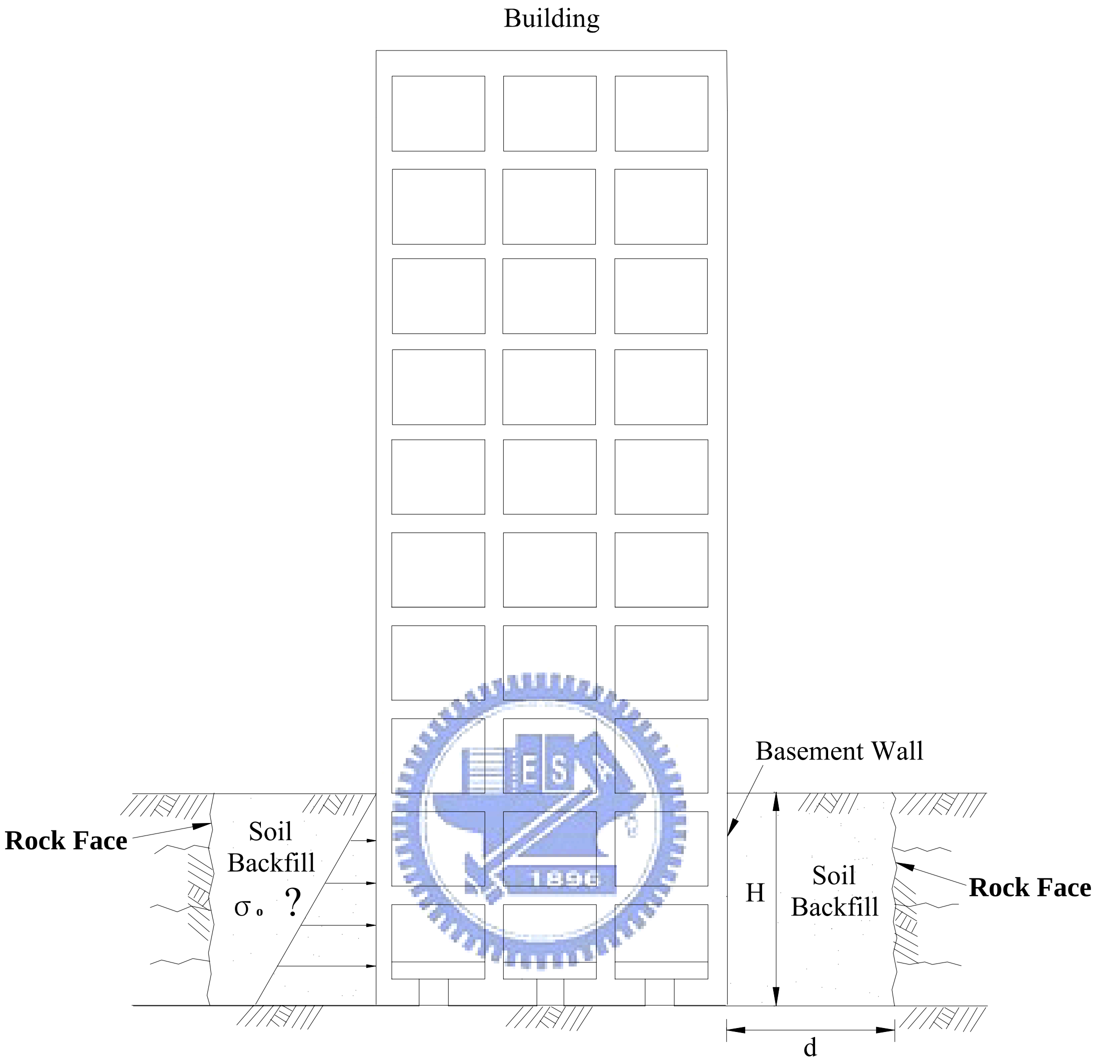

Fig. 1.1. Earth pressure at-rest on the basement wall near vertical rock faces

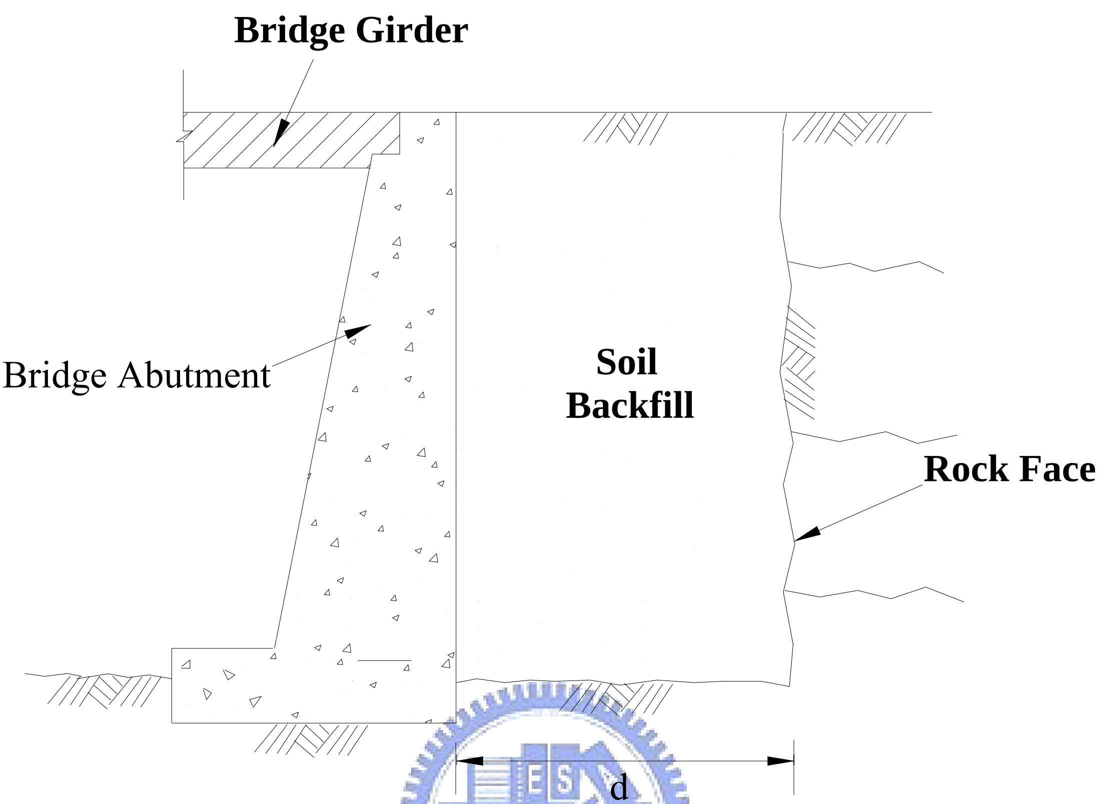

Fig. 1.2. Bridge abutment near a vertical rock face

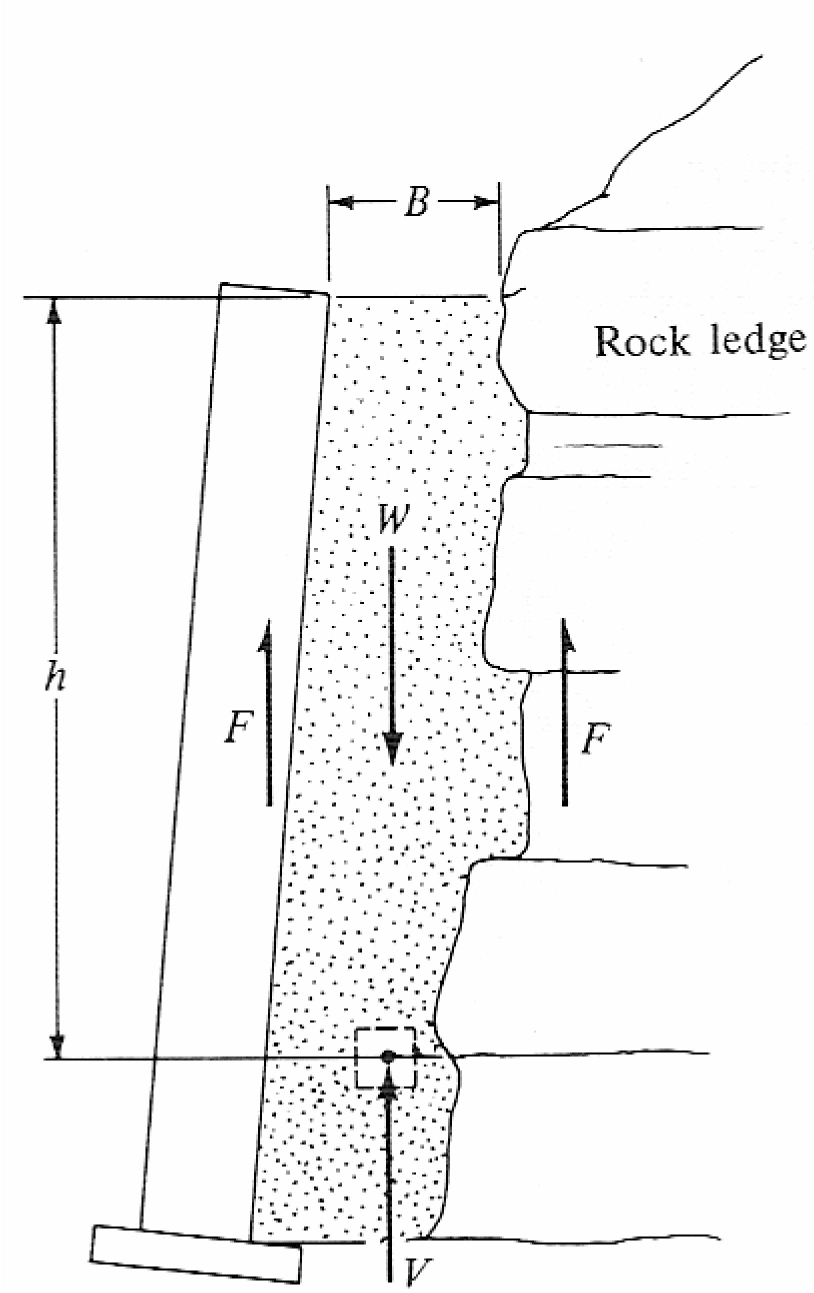

Fig. 1.3. Fascia wall (after Spangler and Handy, 1982)

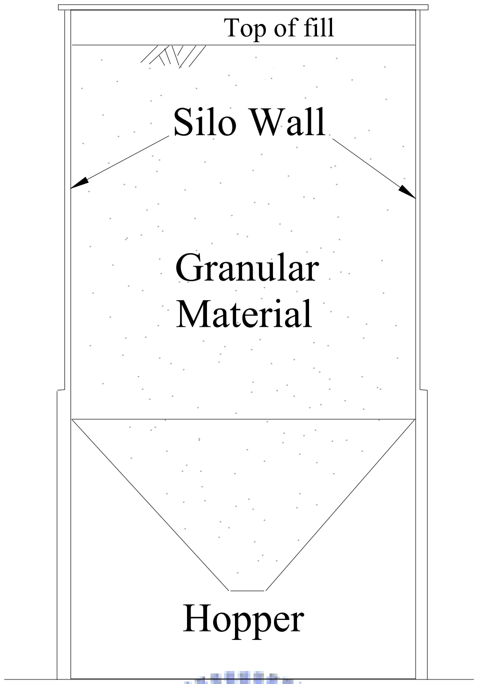

(a)


(b)

Fig. 1.4. Circular silo filled with granular material

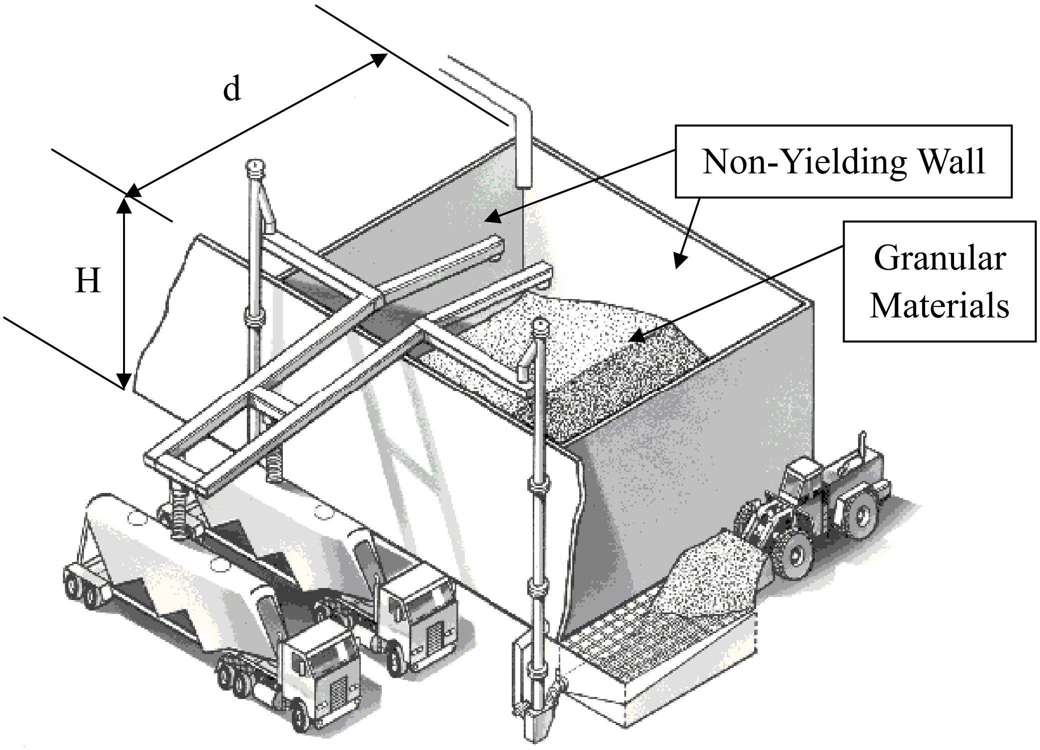

Fig. 1.5. Storage bunker filled with granular material

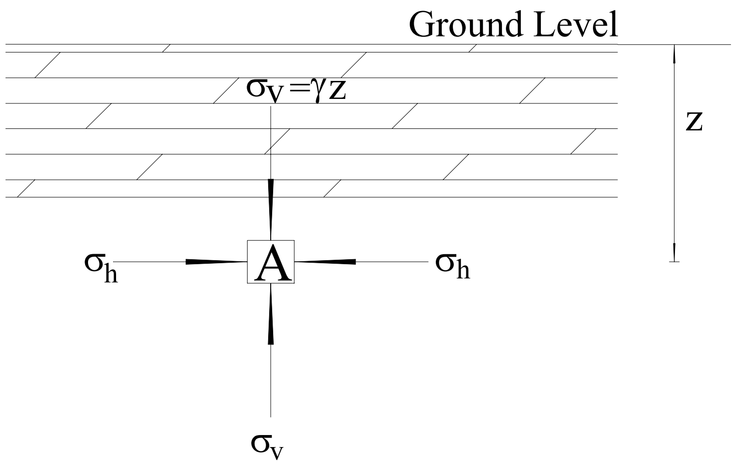

(a)

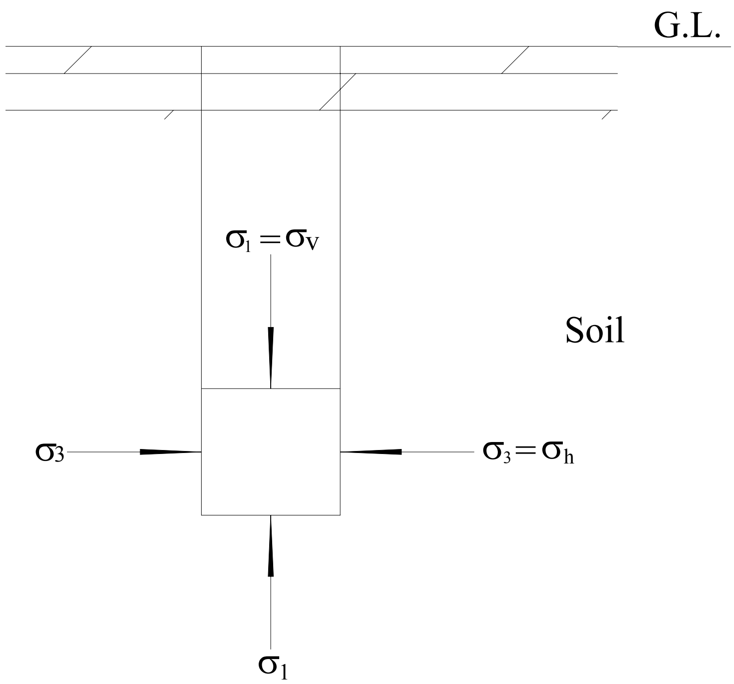

(b)

Fig. 2.1. Development of in-situ stresses

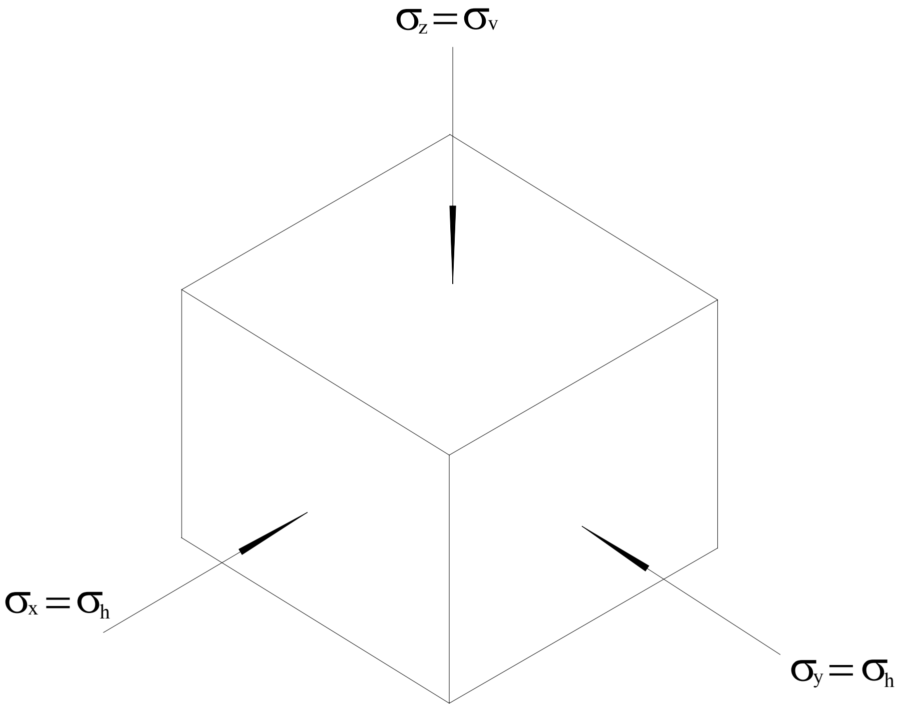

Fig. 2.2. Principal stresses in soil element

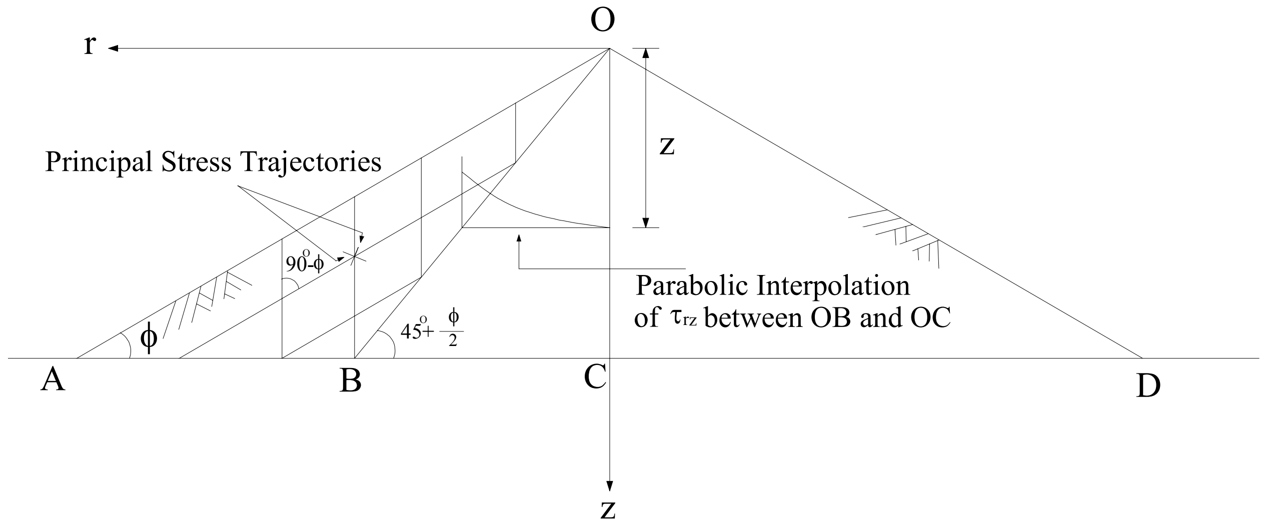

Fig. 2.3. Jaky's formulation of the relationship between K_o on OC and ϕ mobilized in OAB (after Mesri and Hayat, 1993)

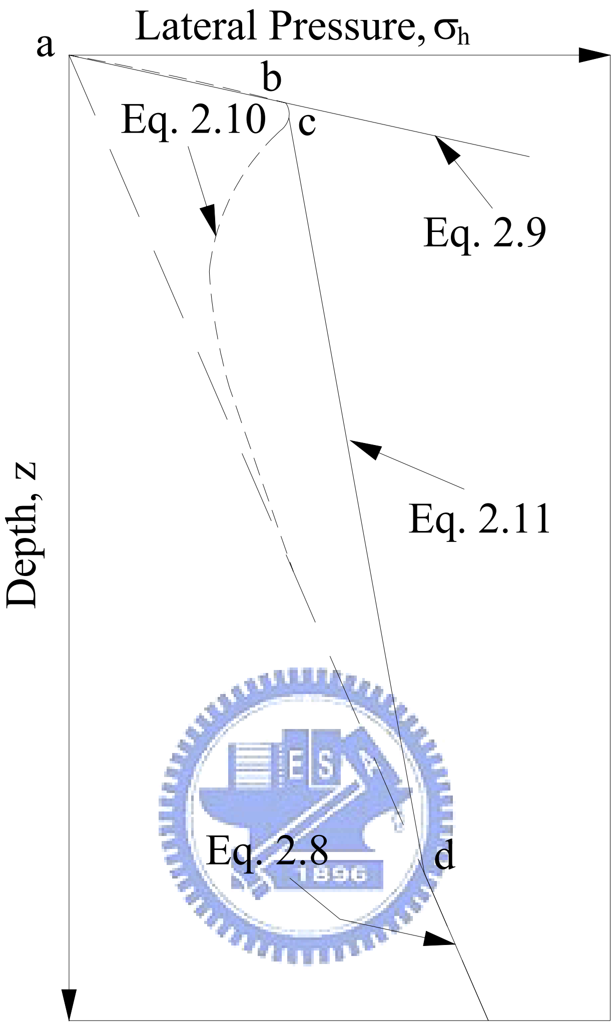

Fig. 2.4. Hand-calculation for estimating σ_h
(after Peck and Mesri, 1987)

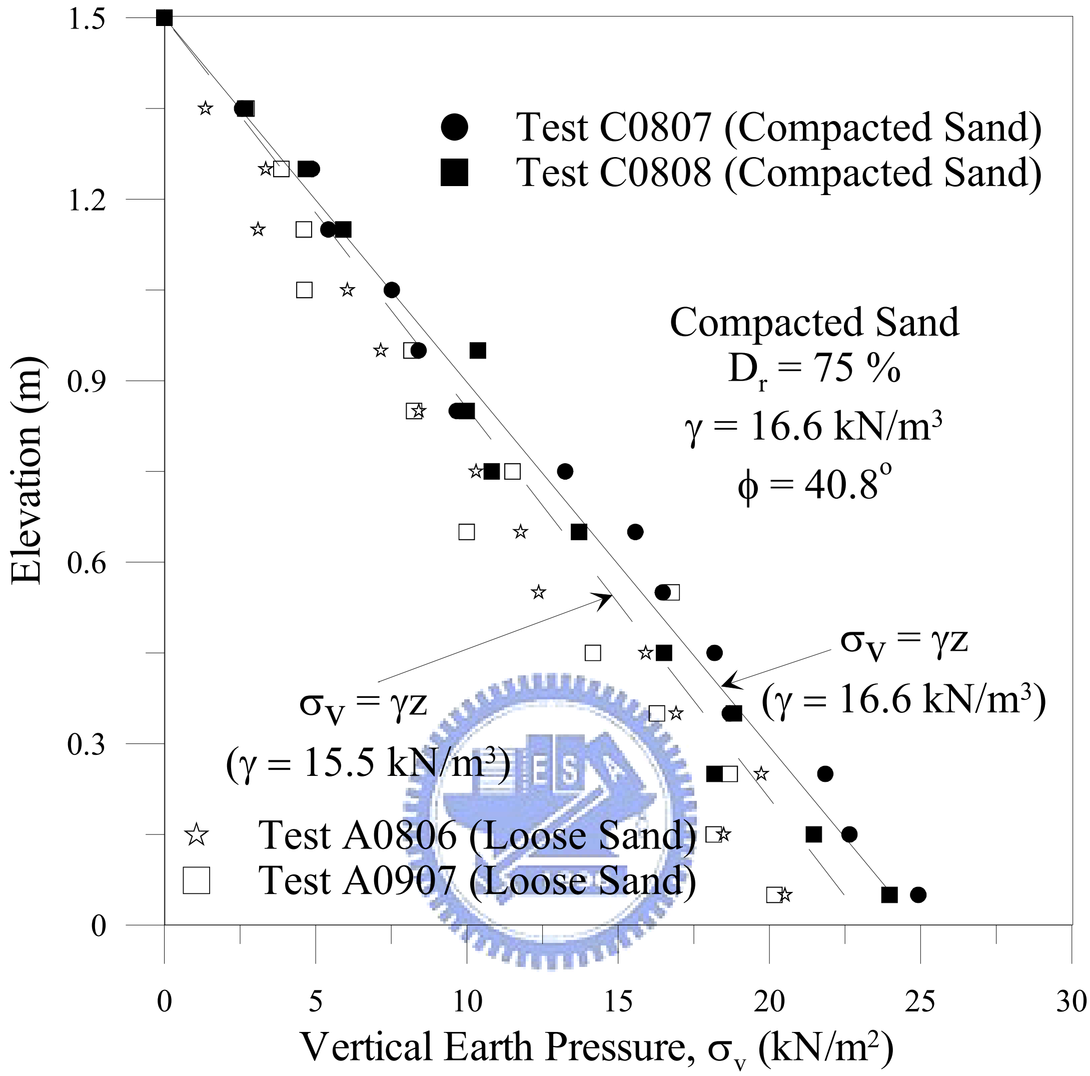

Fig. 2.5. Distribution of vertical earth pressure measured in soil mass (after Chen, 2003)

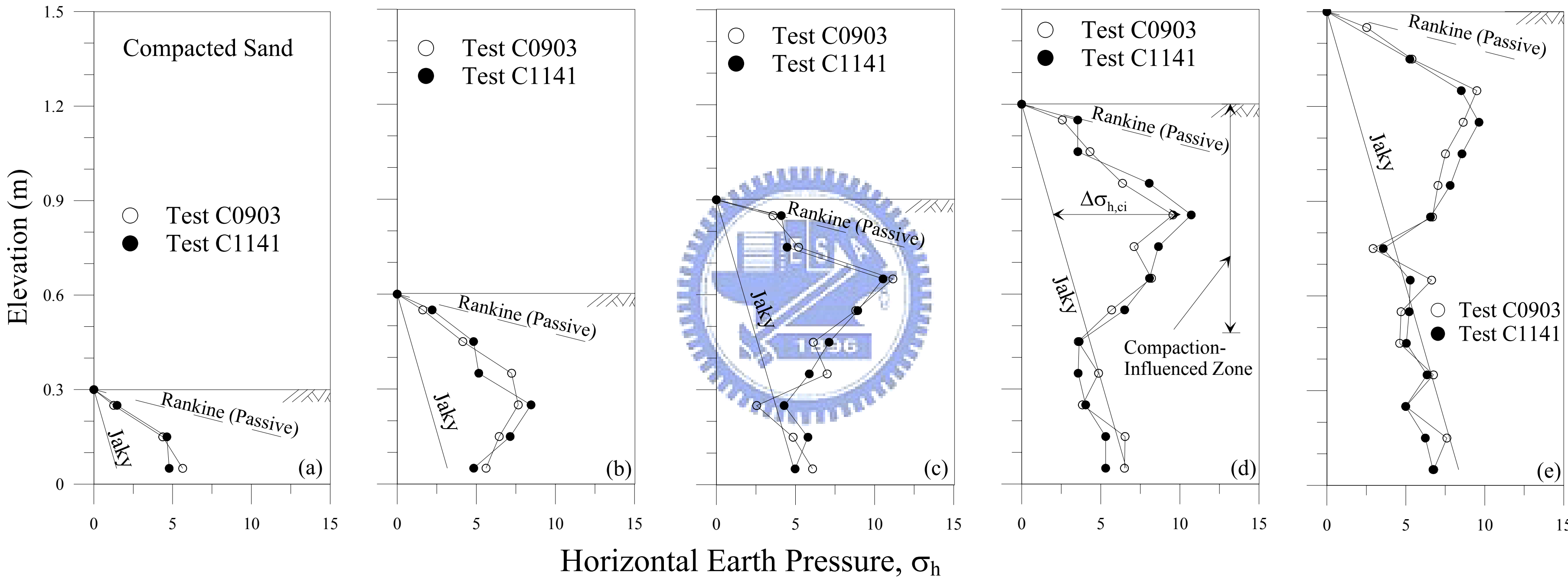

Fig. 2.6. Distribution of horizontal earth pressure after compaction (after Chen, 2003)

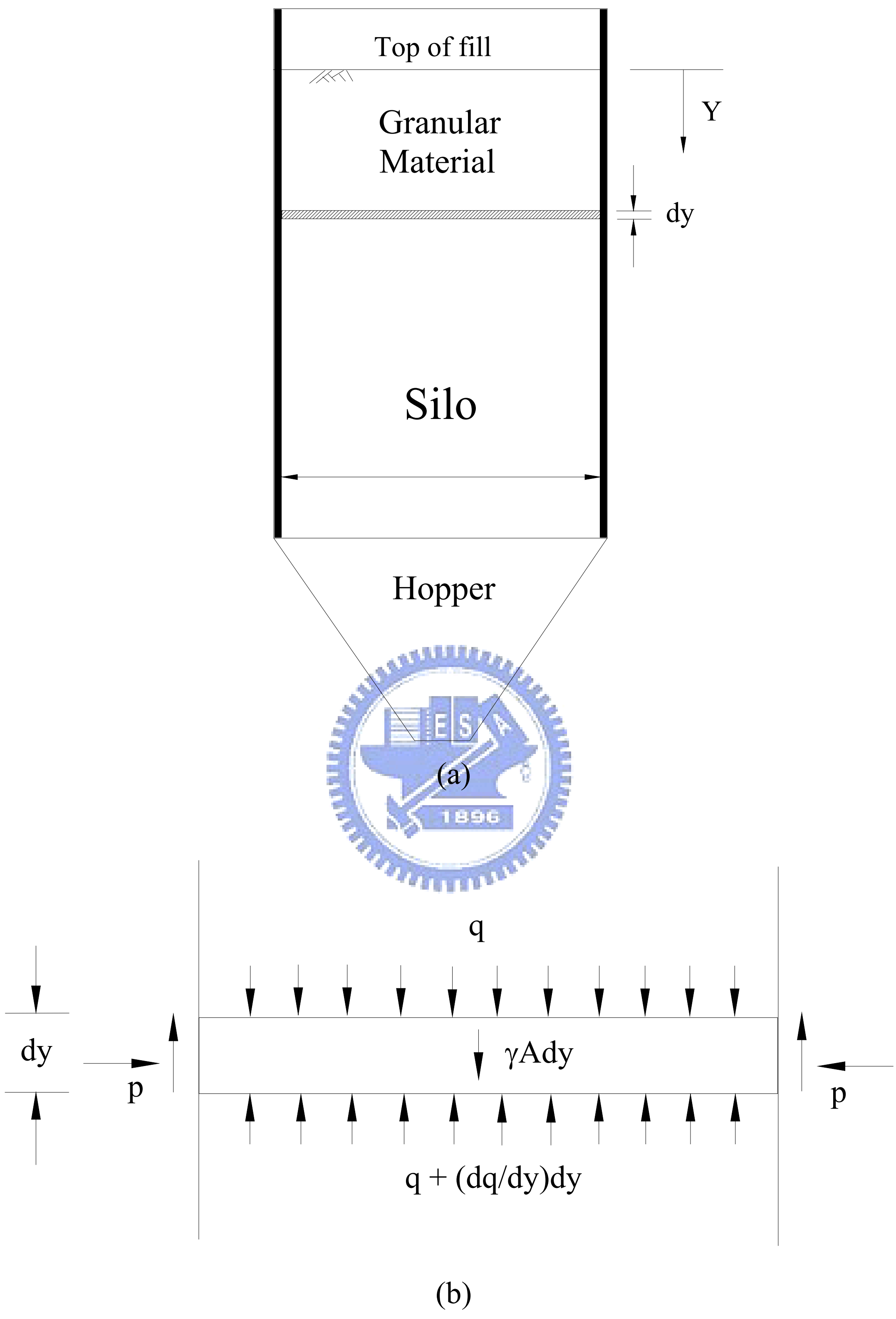

Fig. 2.7. Horizontal lamina for derivation of Janssen's equations (redrawn after Safarian and Harris, 1985)

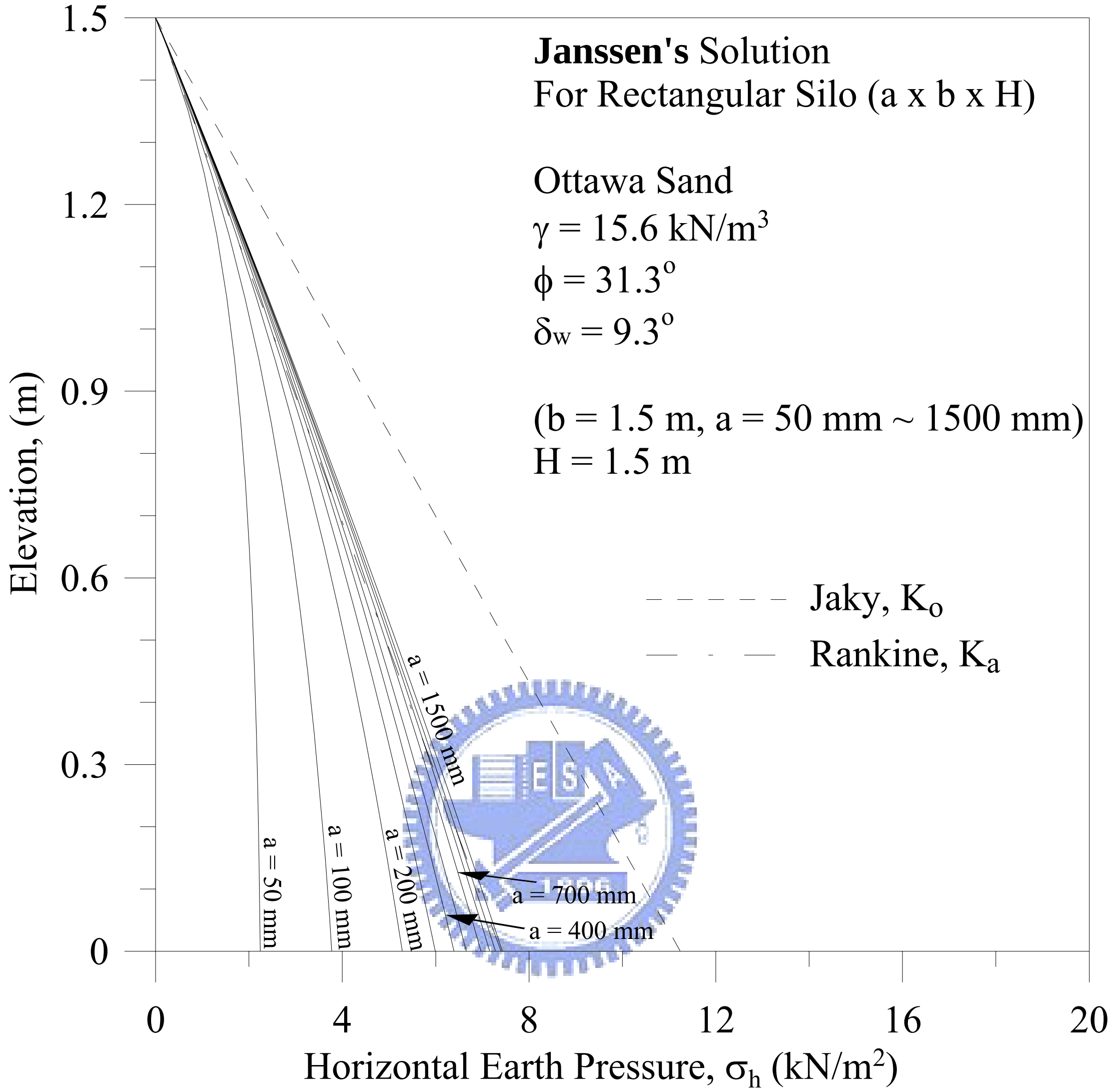

Fig. 2.8. Distribution of earth pressure for Janssen's solution with different hydraulic radius R

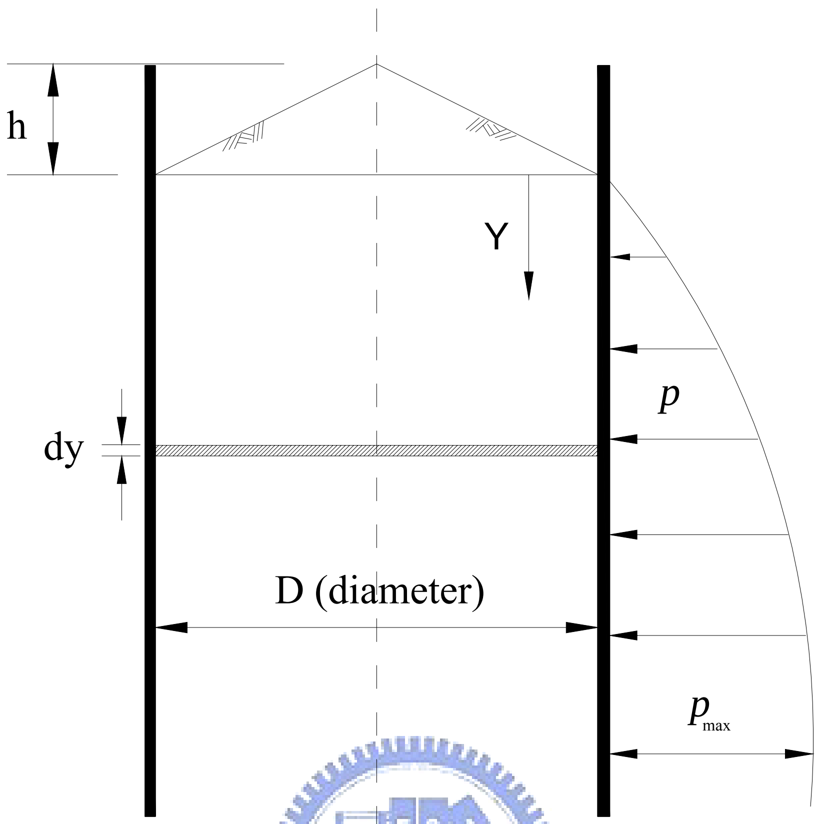

(a)

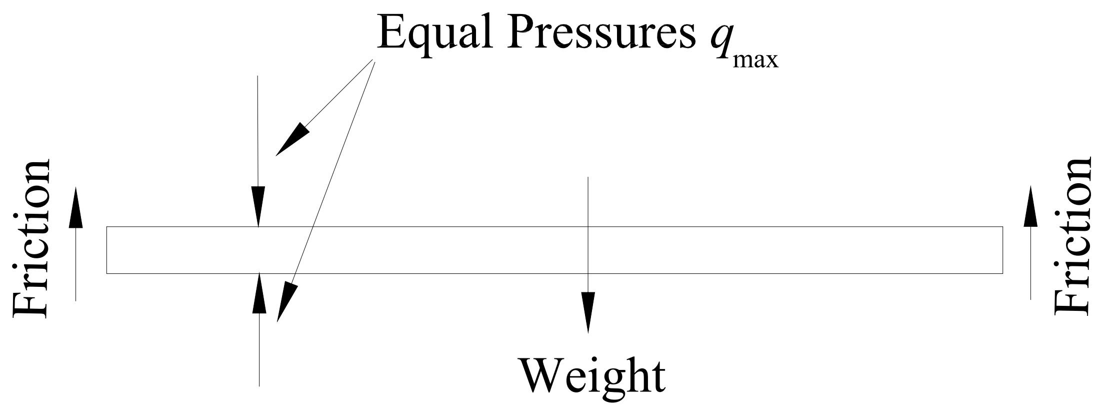

(b)

Fig. 2.9. Lamina of stored material for derivation of the Reimbert's equations (redrawn after Safarian and Harris, 1985)

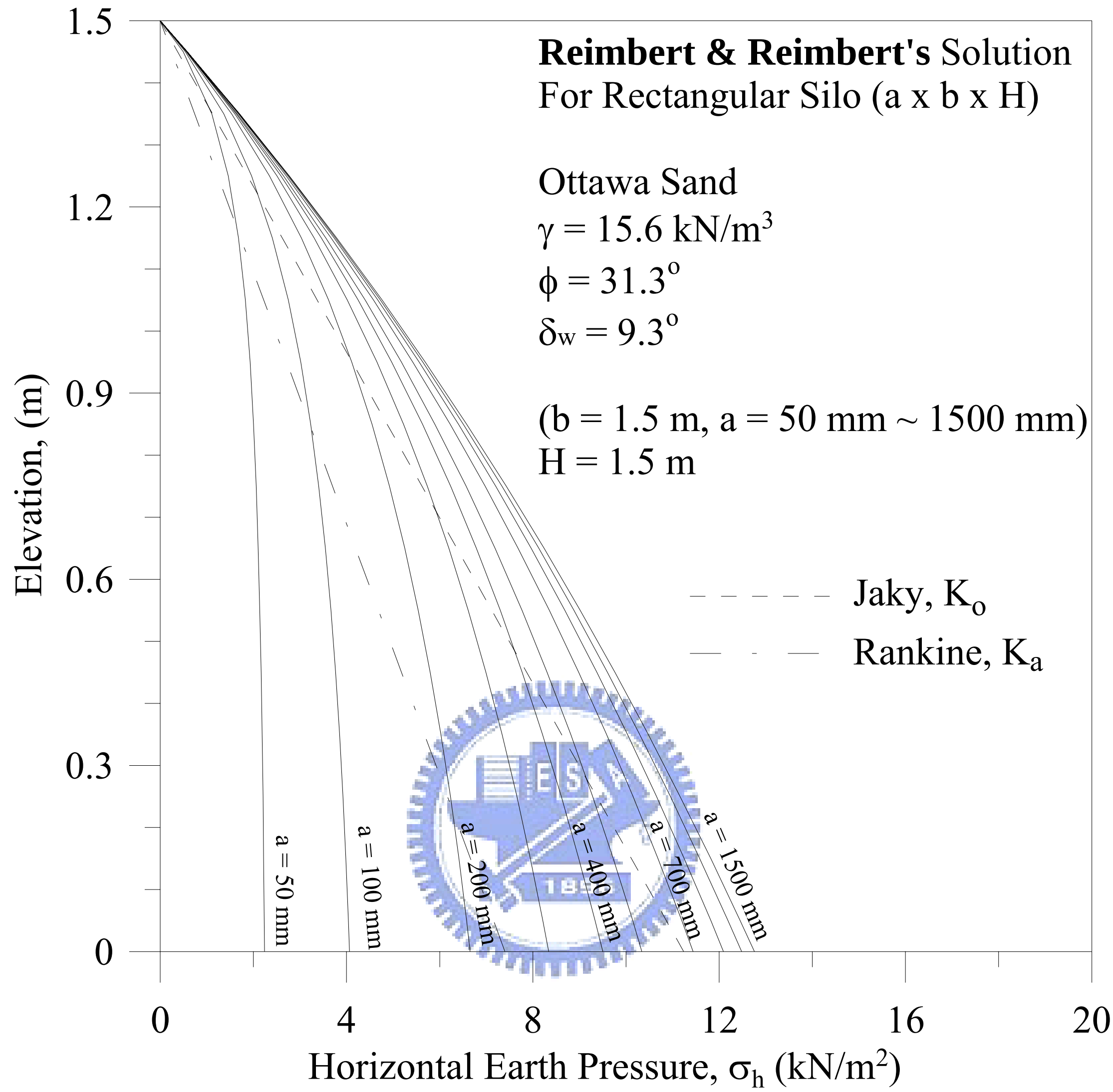

Fig. 2.10. Distribution of earth pressure for Reimbert's solution with different hydraulic radius R

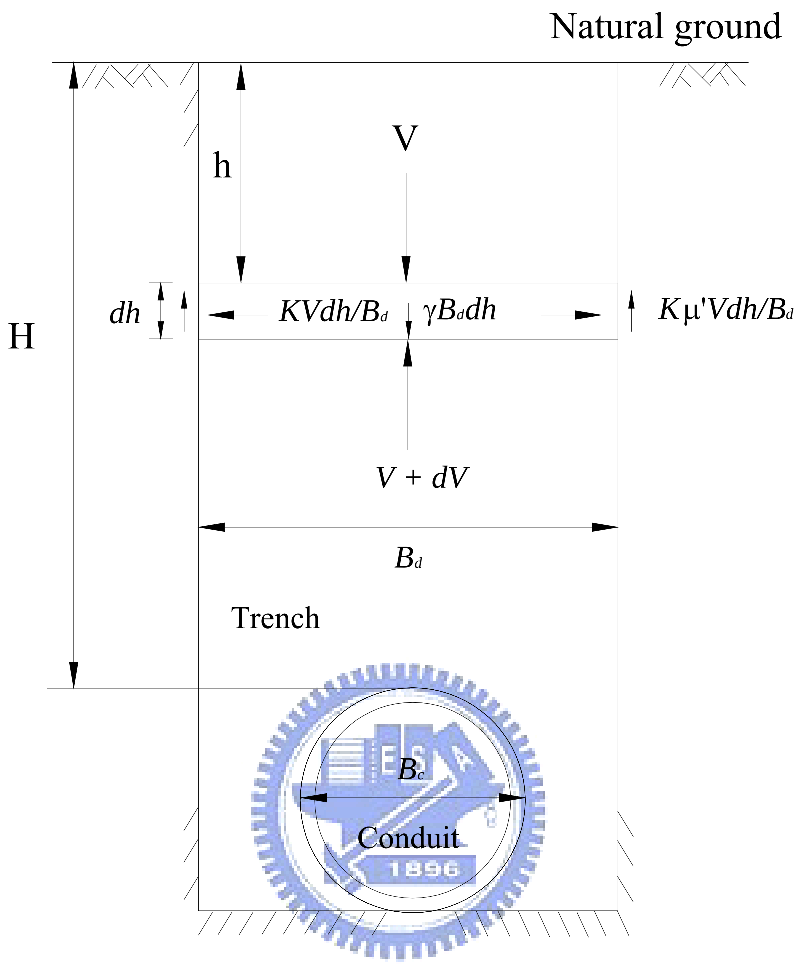

Fig. 2.11. Free-body diagram for a ditch conduit
(after Spangler and Handy, 1982)

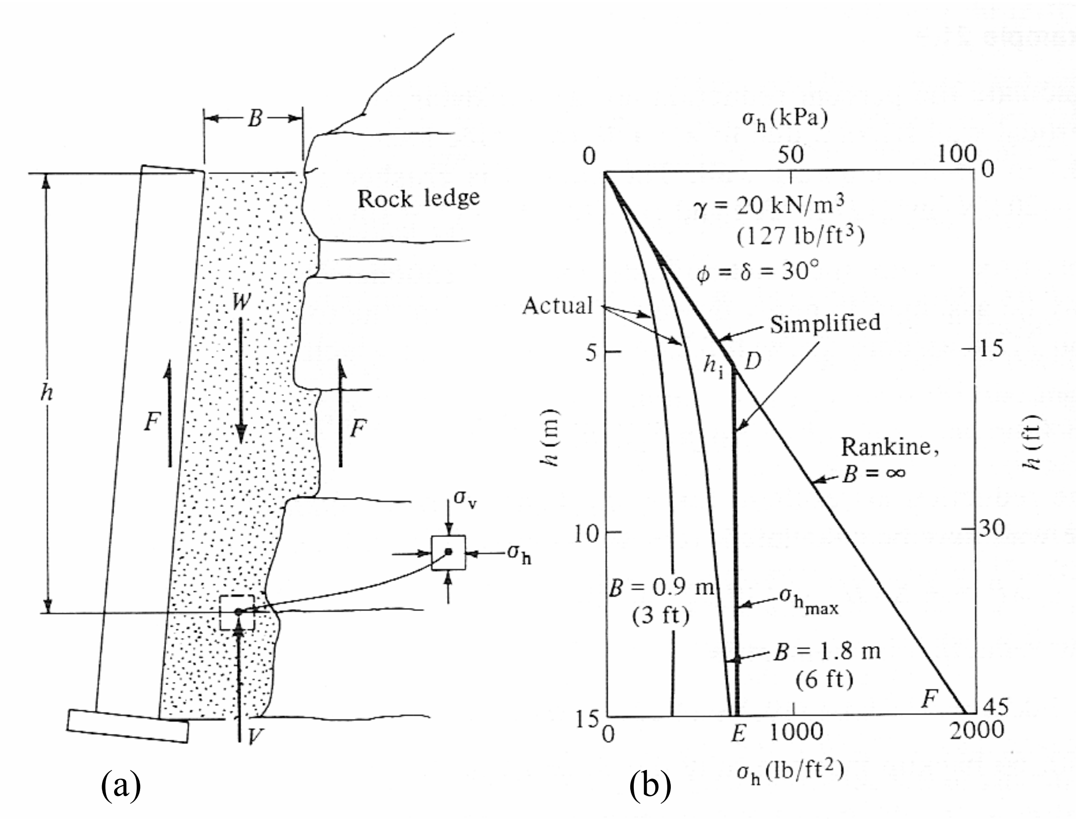

Fig. 2.12. Distribution of soil pressure against fascia walls to partial support from wall friction F
(after Spangler and Handy, 1982)

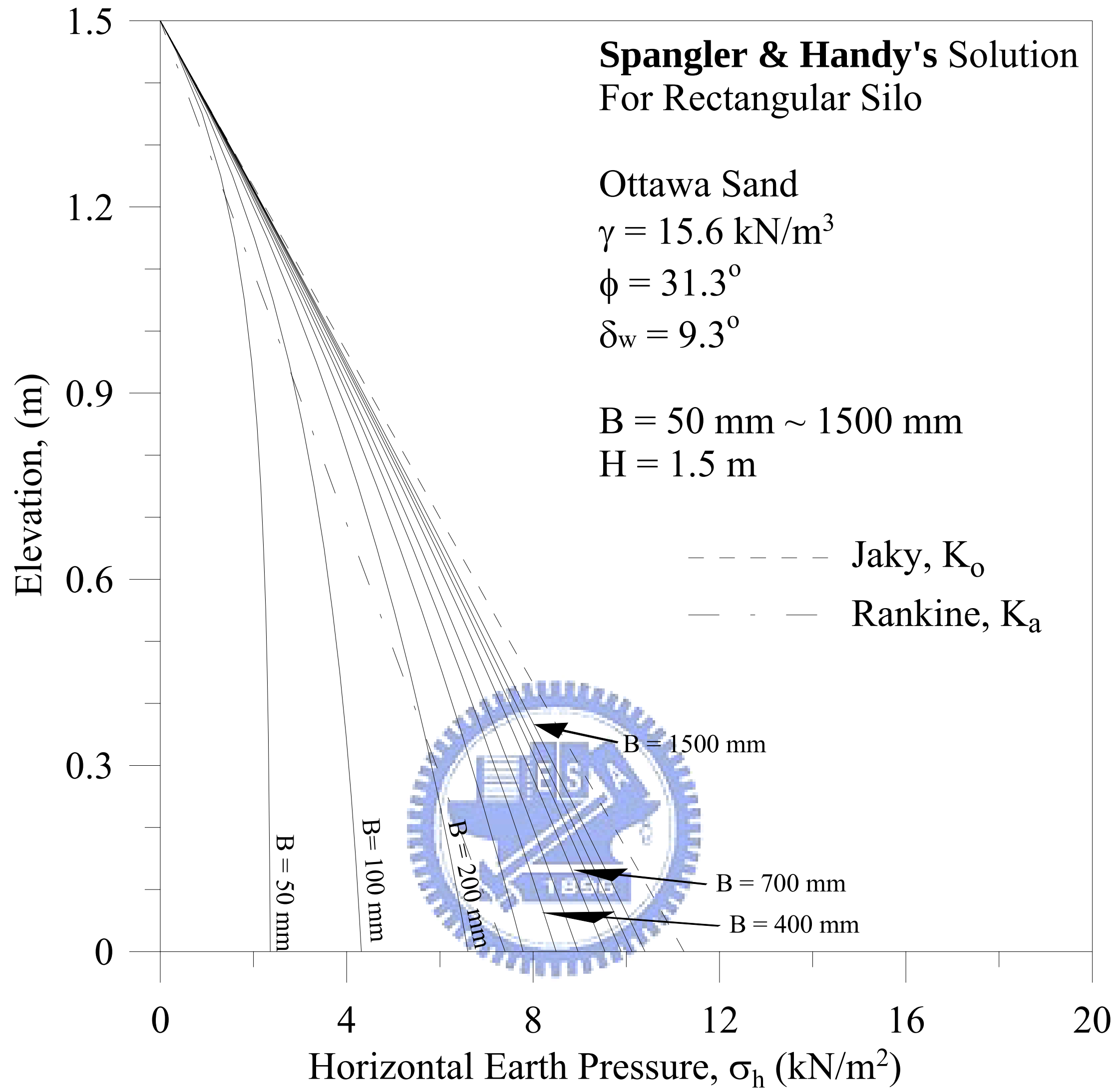

Fig. 2.13. Distribution of earth pressure for Spangler and Handy's solution with different distance B

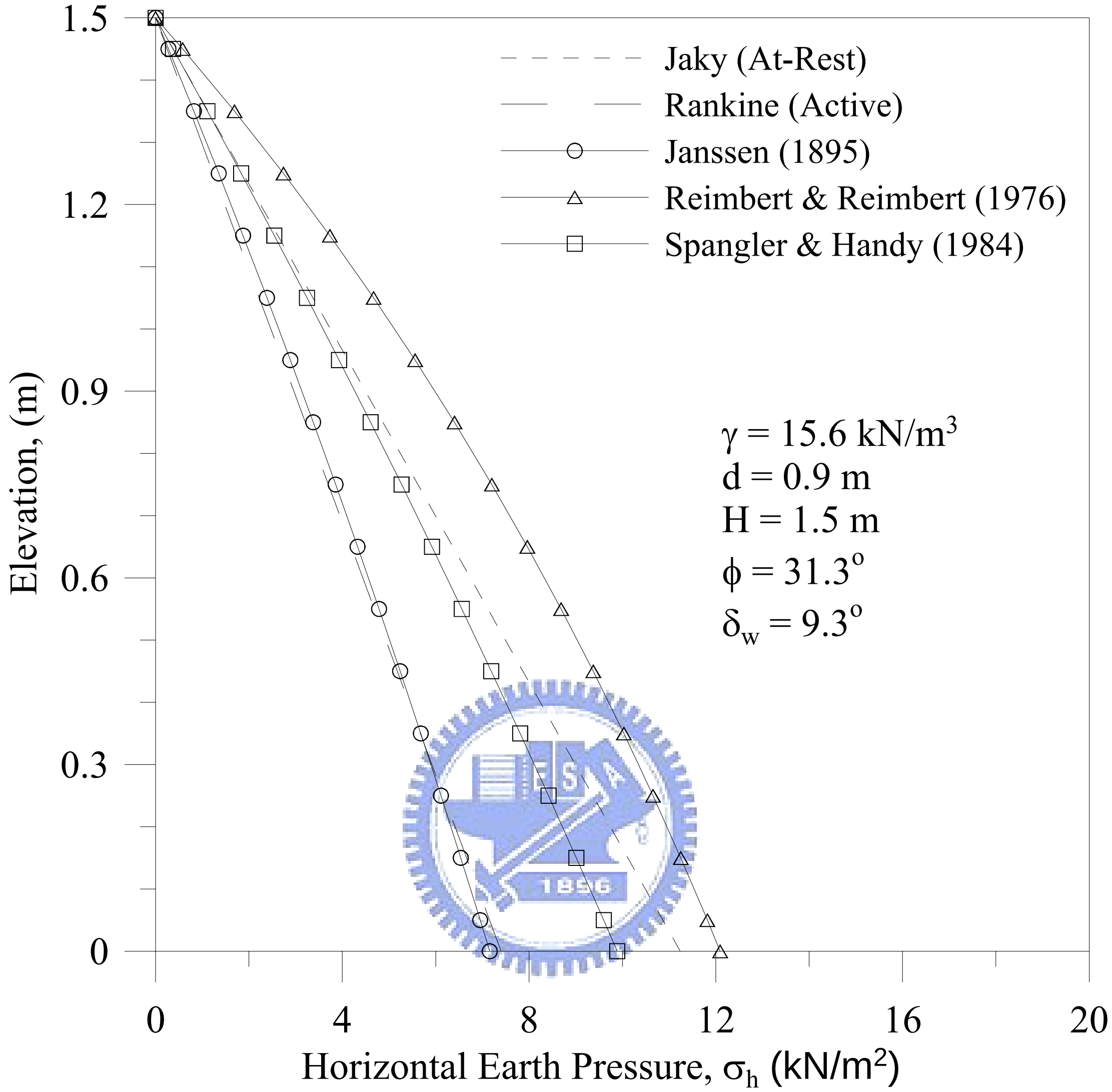

Fig. 2.14. Comparison of earth pressure calculated with different theories for d = 900 mm

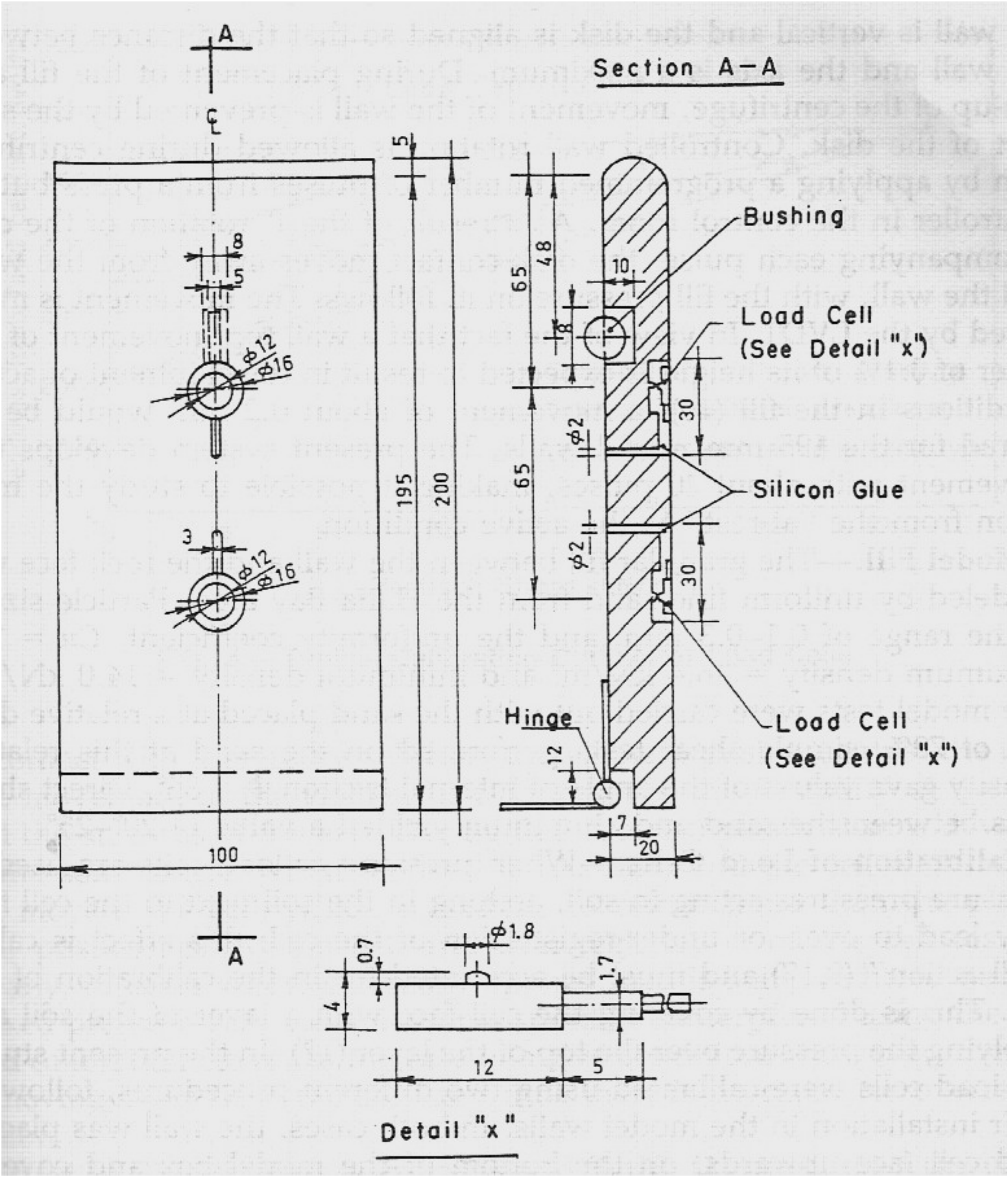

Fig. 2.15. Model retaining wall (after Frydman and Keissar, 1987)

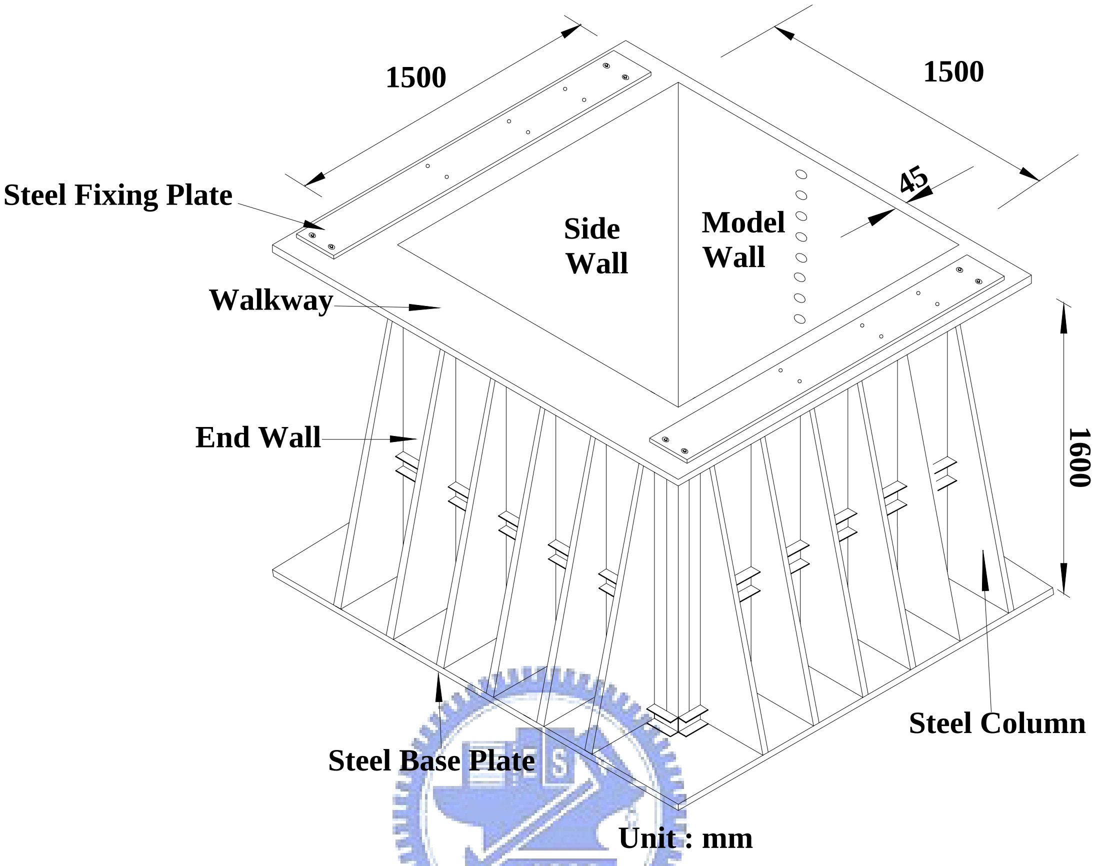

Fig. 3.1. NCTU non-yielding retaining wall

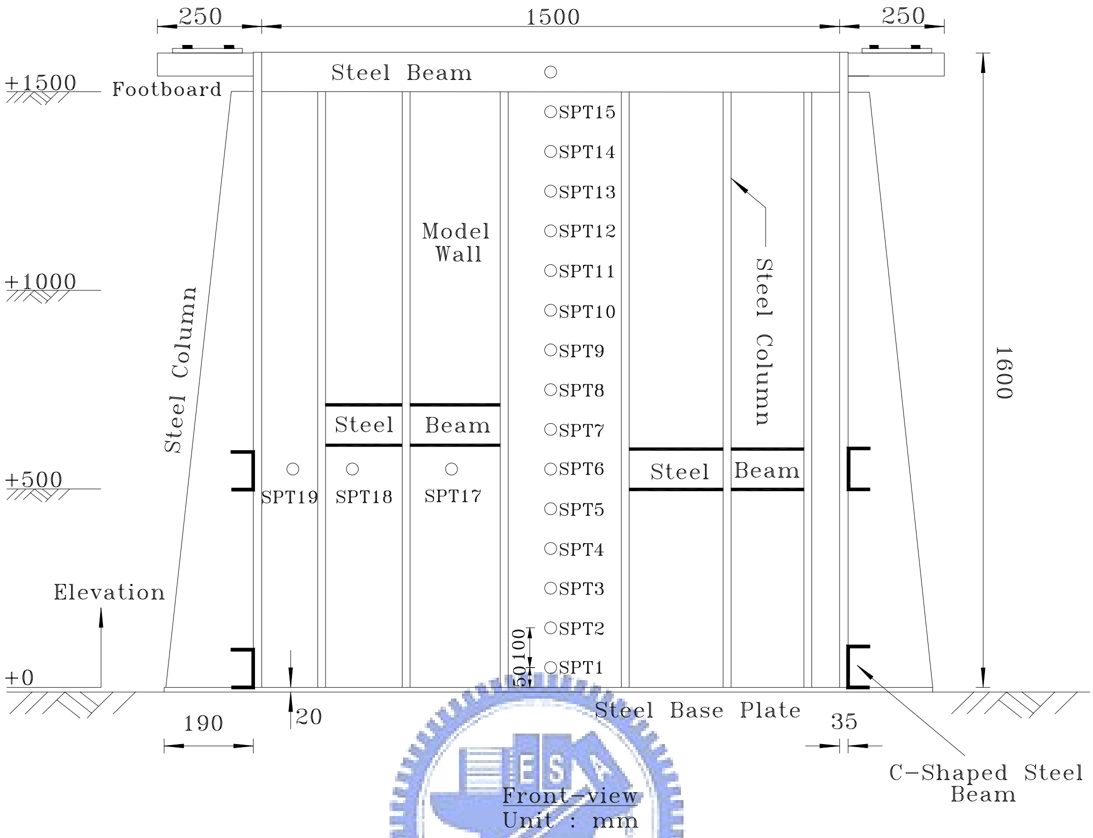

Fig. 3.2. Locations of soil-pressure transducers mounted on the wall (after Chen and Fang, 2002)

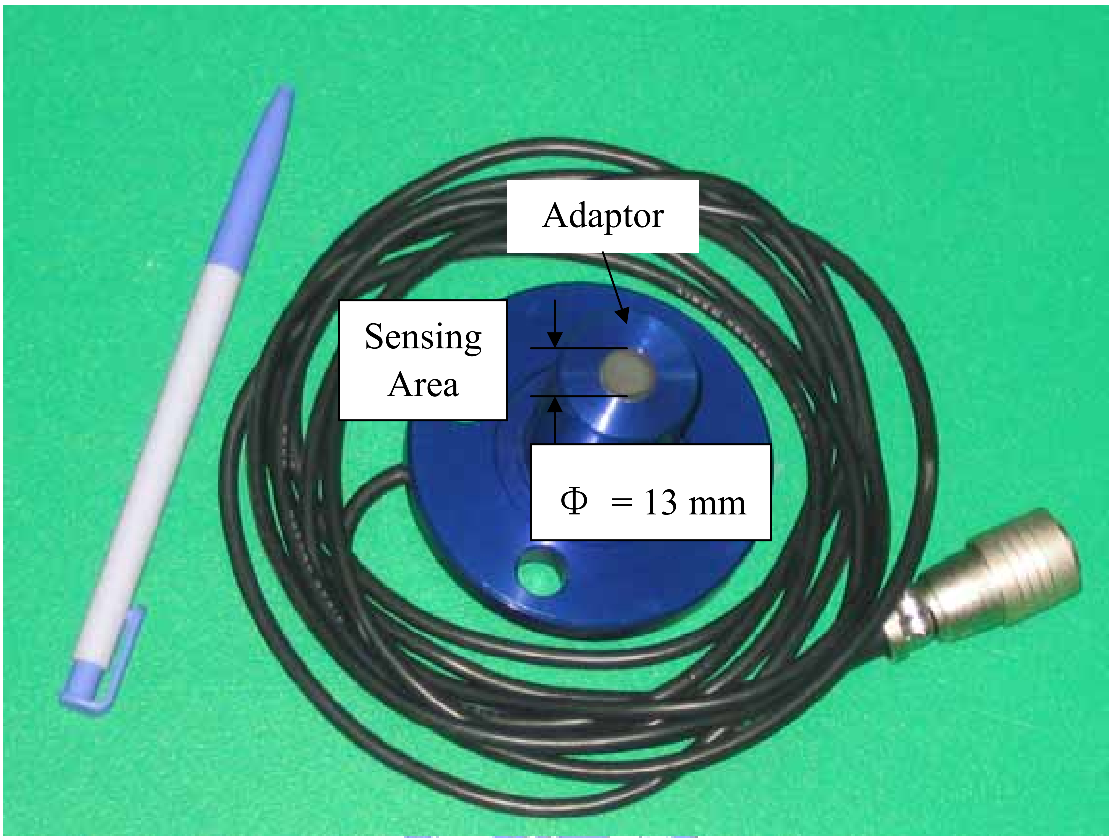

Fig. 3.3. Soil pressure transducer (Kyowa PGM-0.2KG)

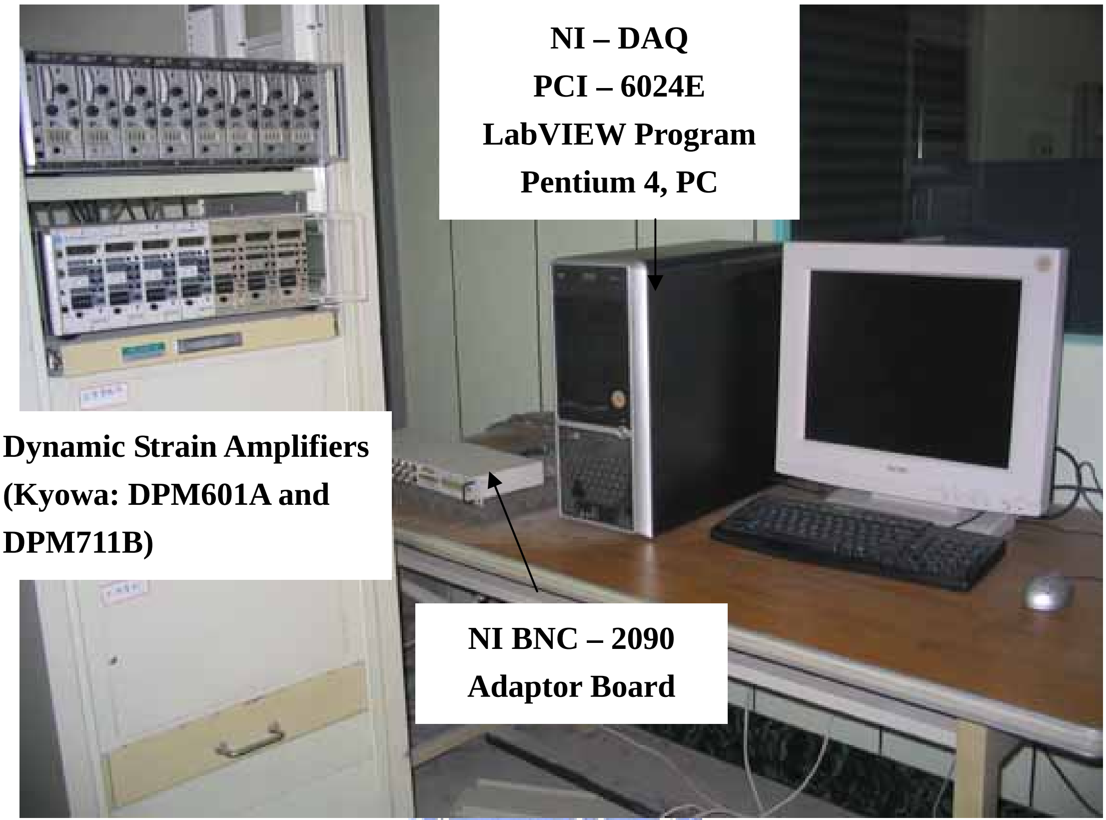

Fig. 3.4. Data acquisition system

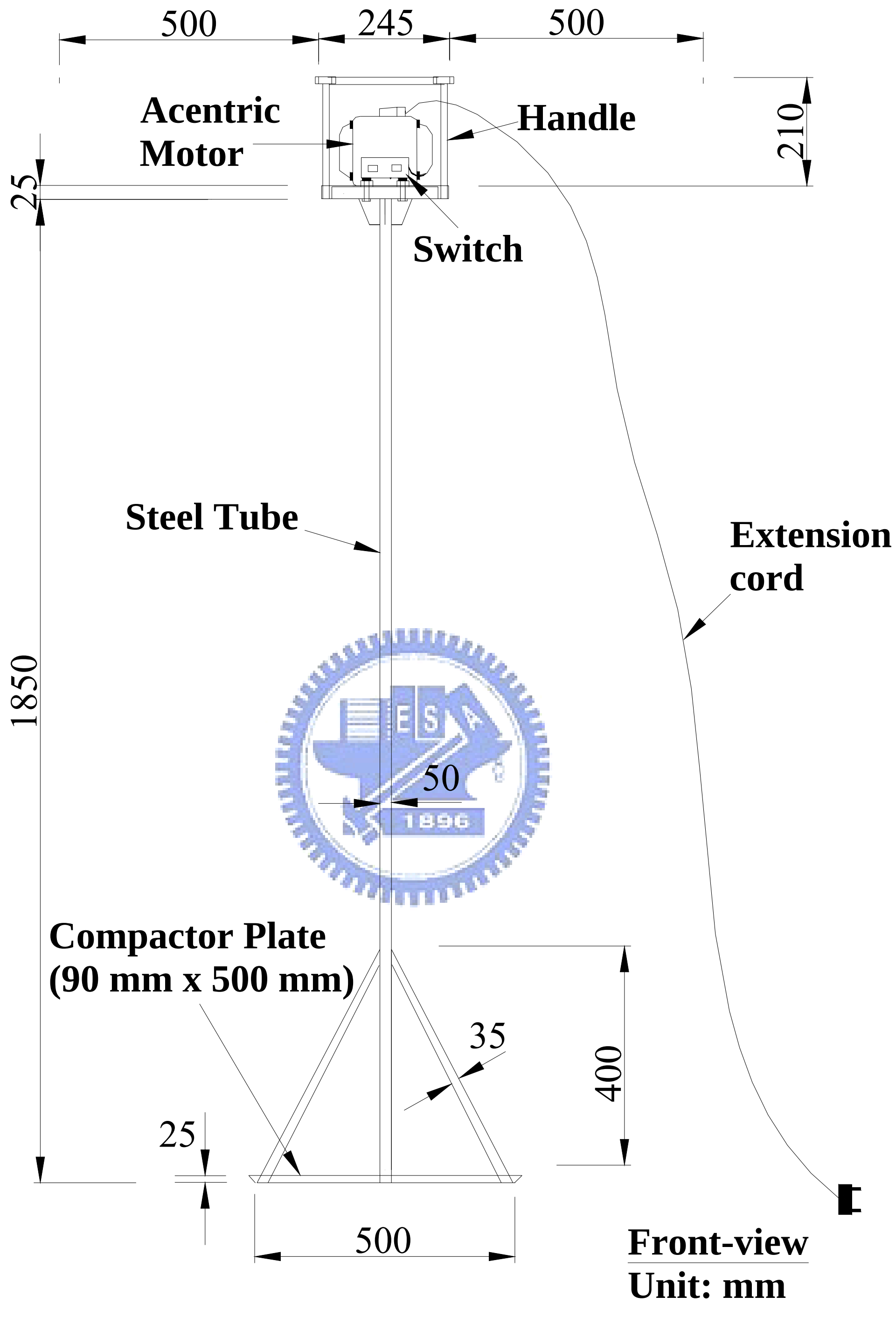

Fig. 3.5. 90 mm Ｘ 500 mm vibratory soil compactor

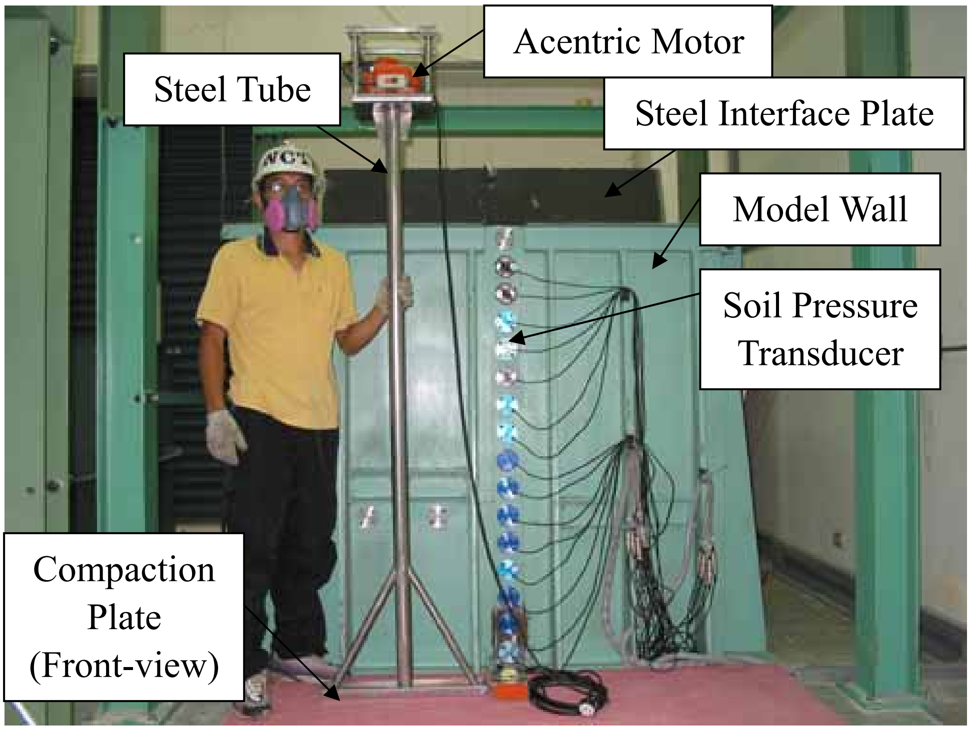

(a) Front view of the strip soil compactor and the model wall

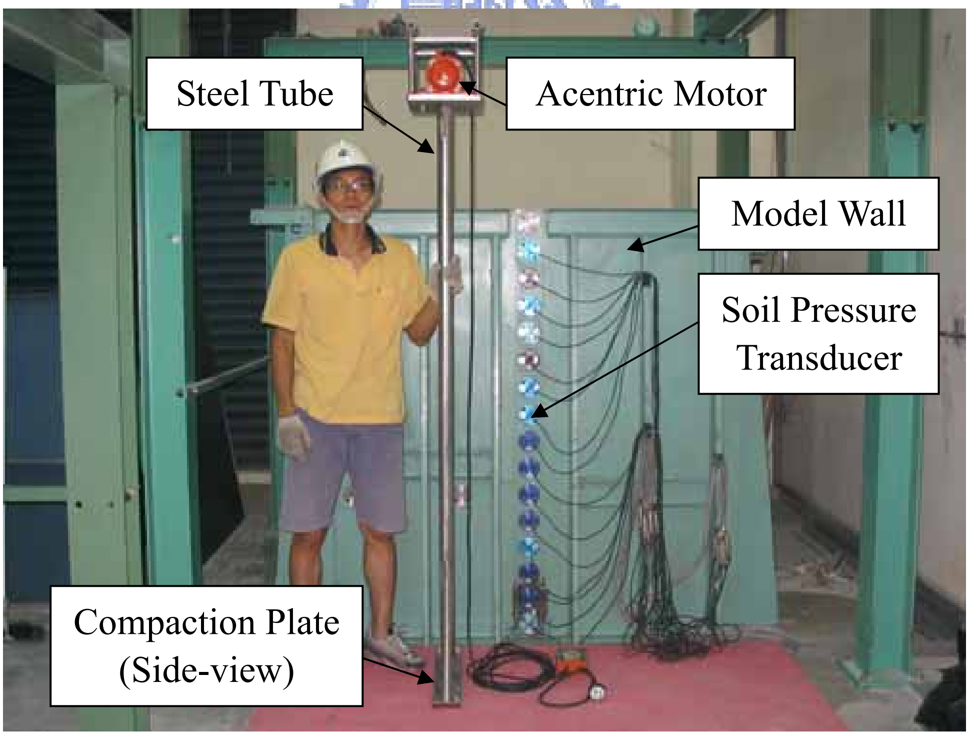

(b) Side view of the strip soil compactor

Fig. 3.6. Strip vibratory soil compactor

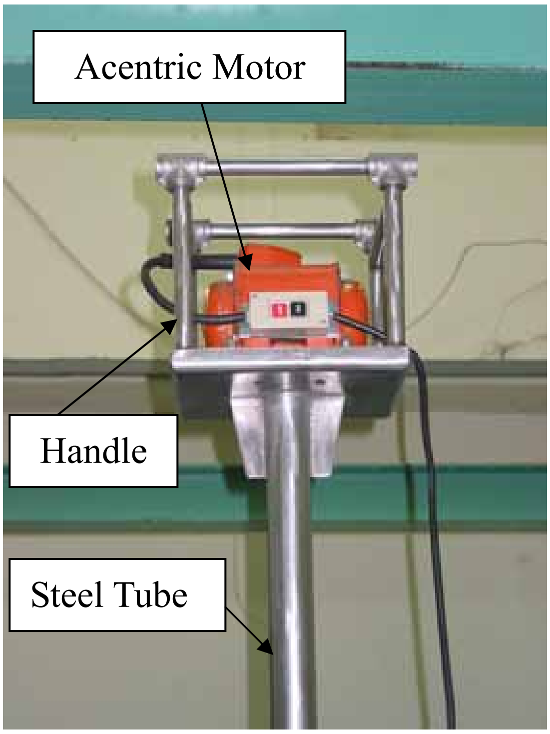

(c) Acentric motor on strip compactor

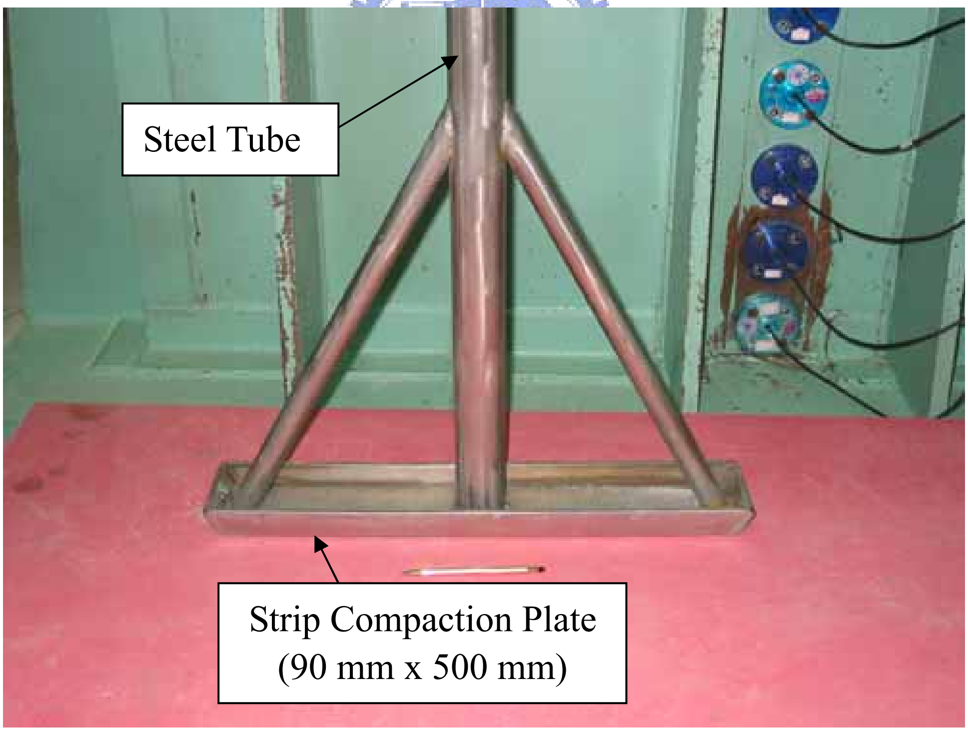

(d) Steel tube and compaction plate

Fig. 3.6. Strip vibratory soil compactor (cont'd)

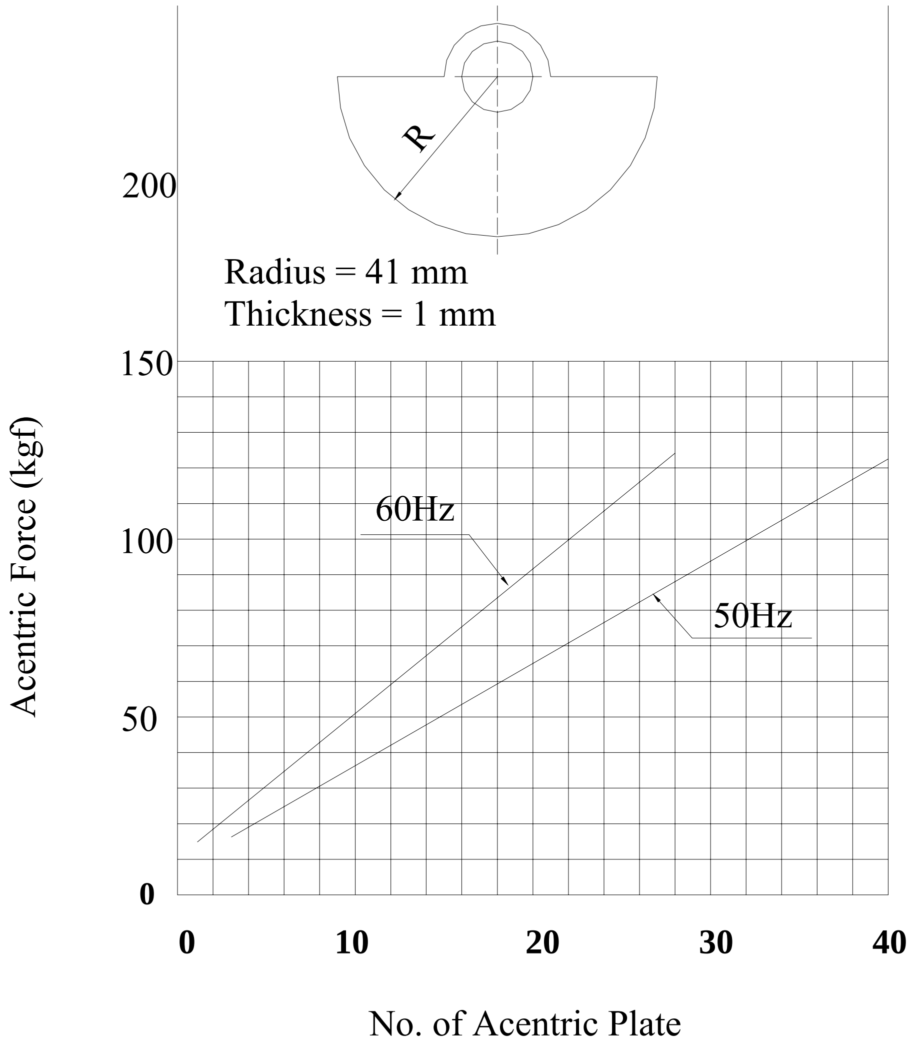

Fig. 3.7. Acentric force as a function of number of acentric plate (Mikasa KJ75)

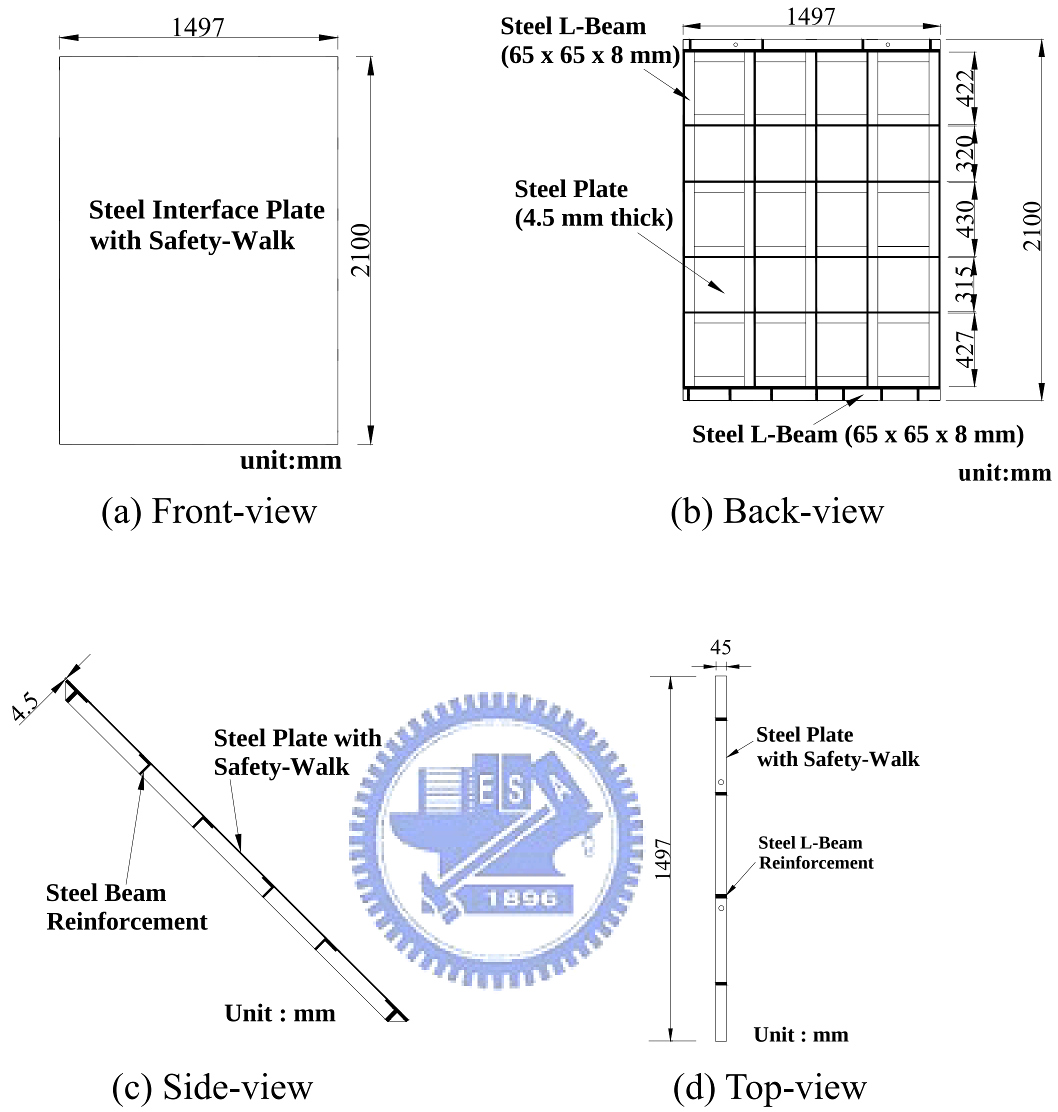

Fig. 4.1. 2100 mm Ｘ 1497 mm steel interface plate

(a) Front-view

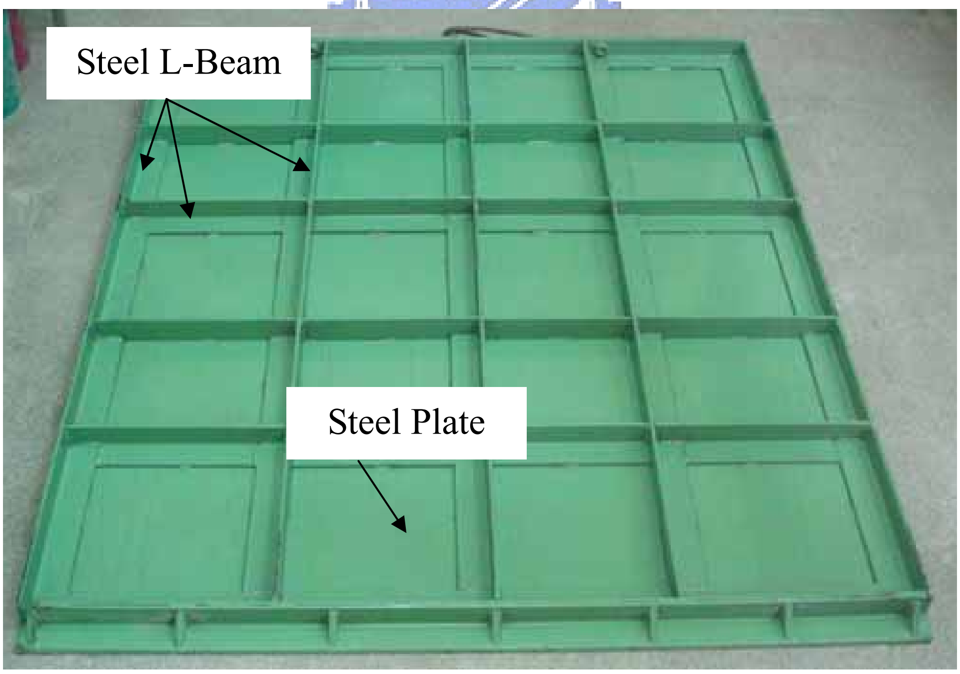

(b) Back-view

Fig. 4.2. Steel interface plate

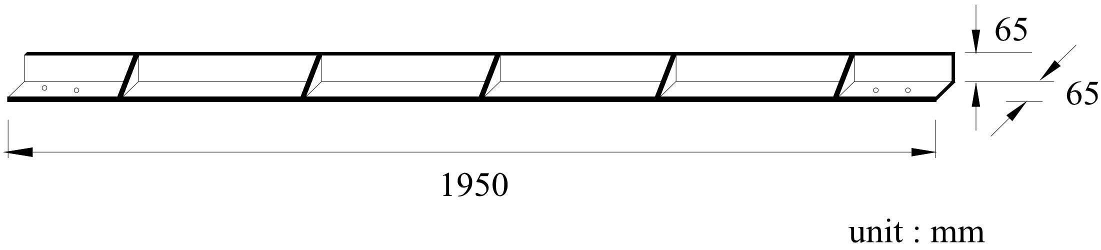

(a)

(b)

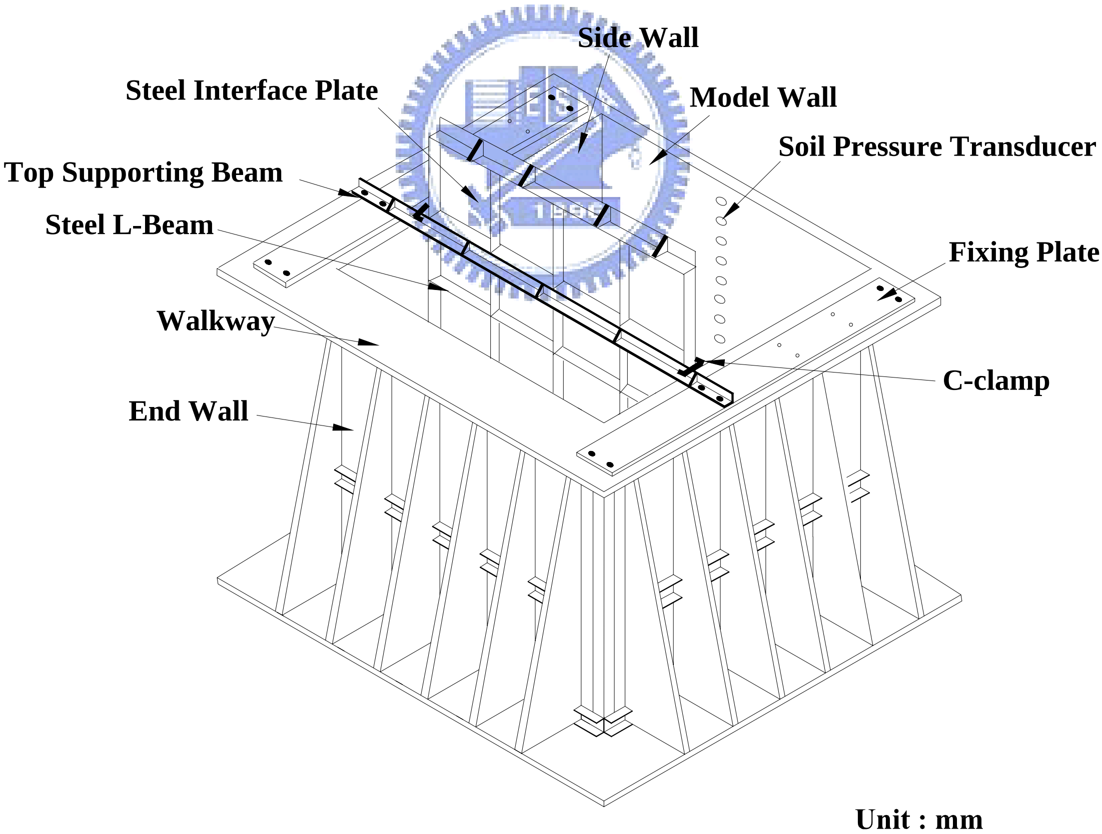

(c) Model retaining wall with top supporting beam

Fig. 4.3. Top supporting beam

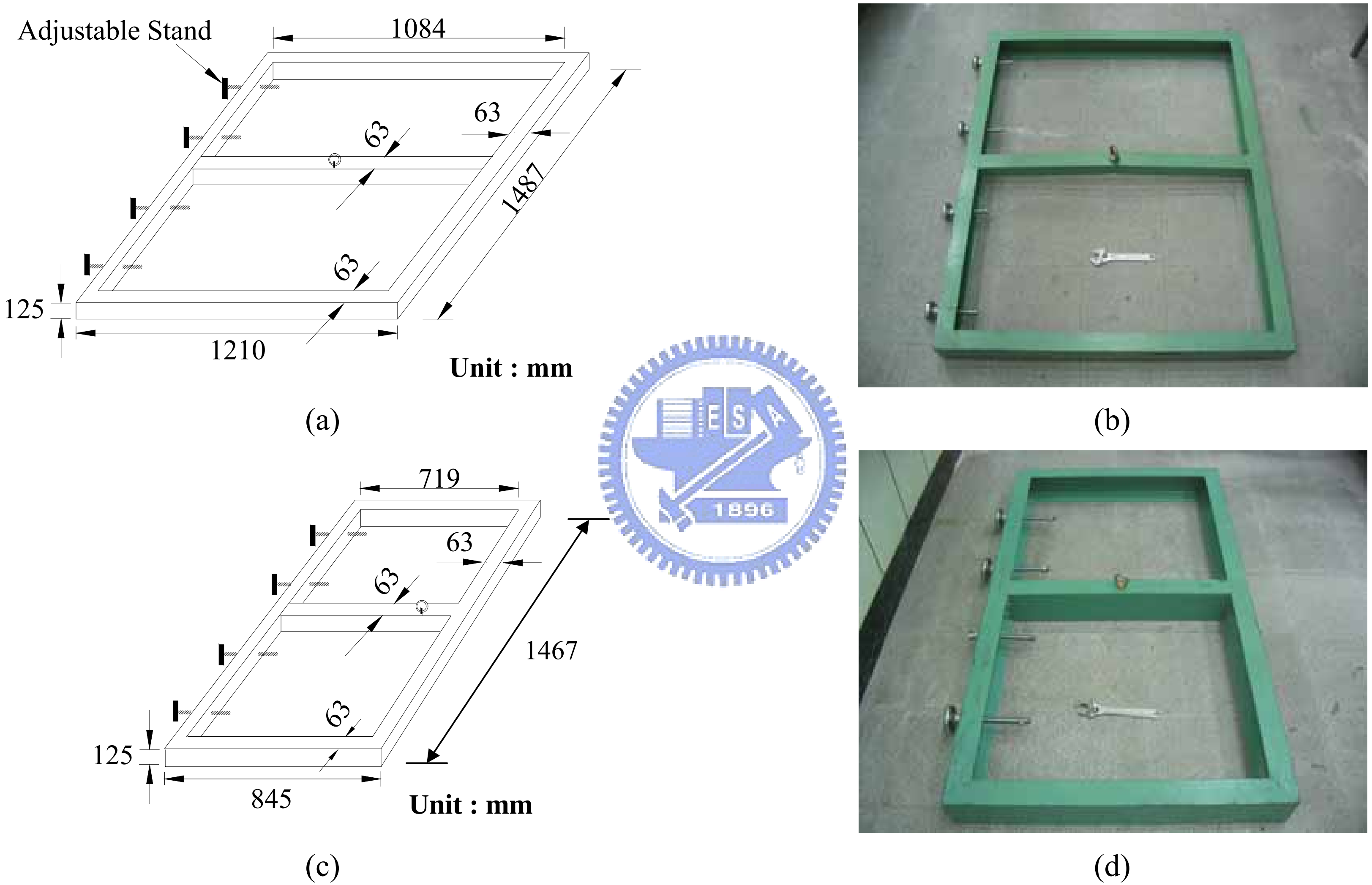

Fig. 4.4. Base supporting frame

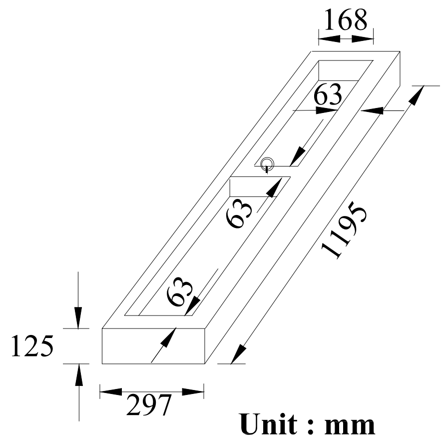

(e)

(f)

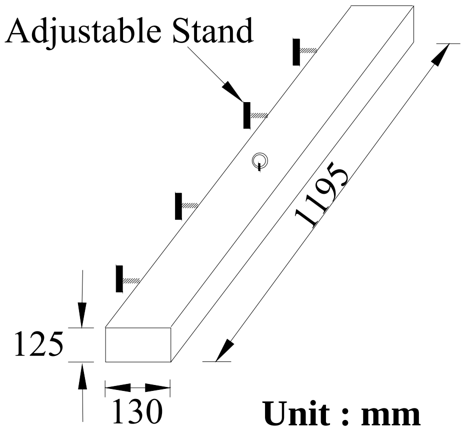

(g)

(h)

Fig. 4.4. Base supporting frame (cont'd)

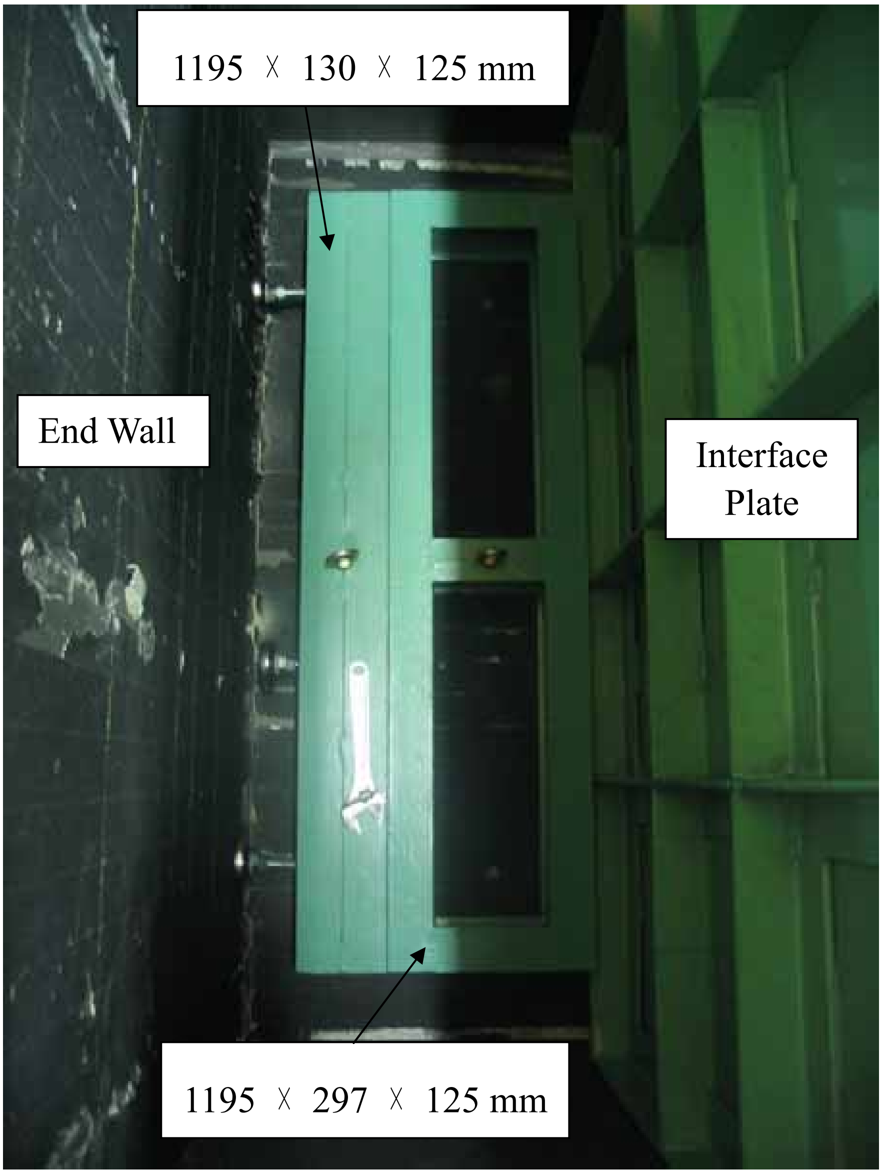

Fig. 4.5. Combination of base supporting frames d = 900 mm

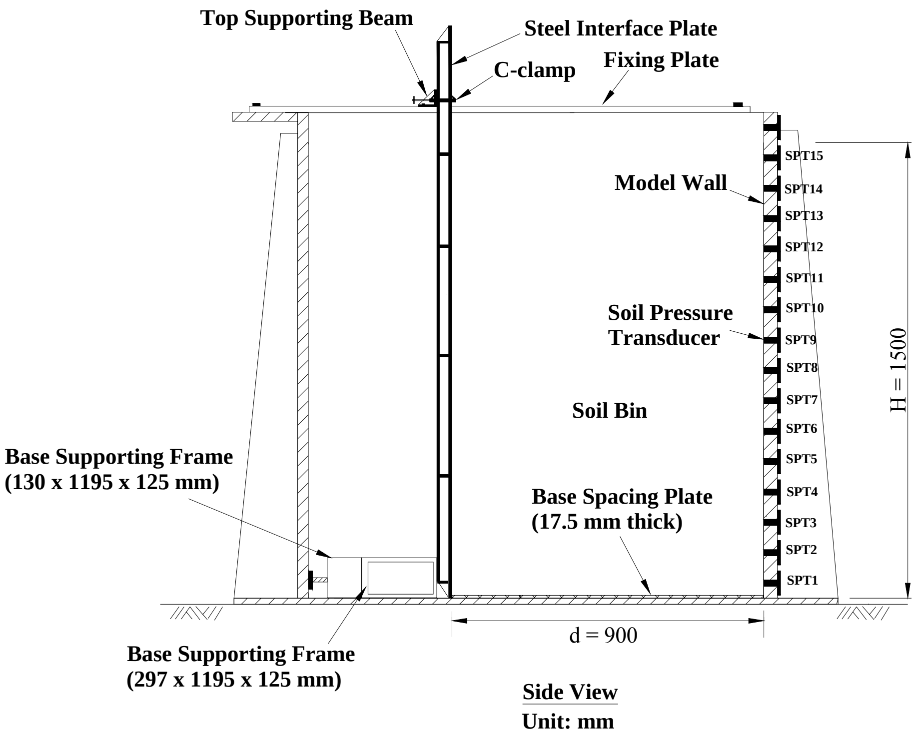

(a) Side-view

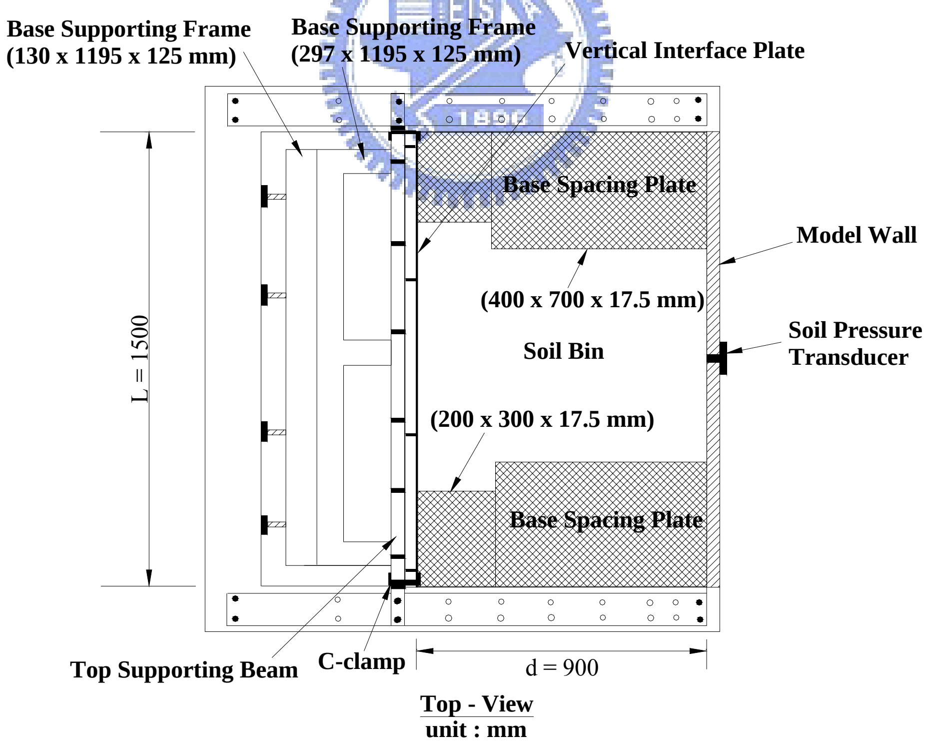

(b) Top-view

Fig. 4.6. Model retaining wall near a vertical interface plate with d = 900 mm

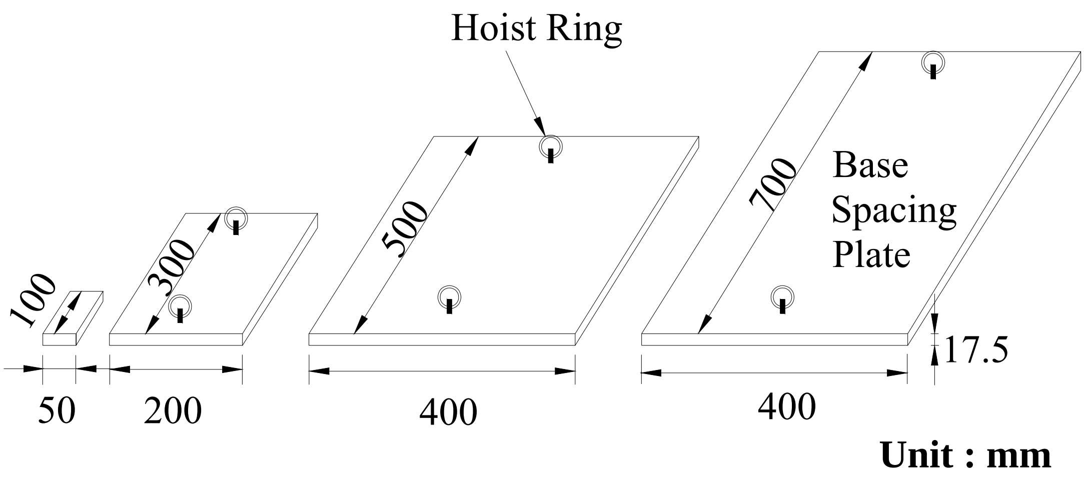

(a)

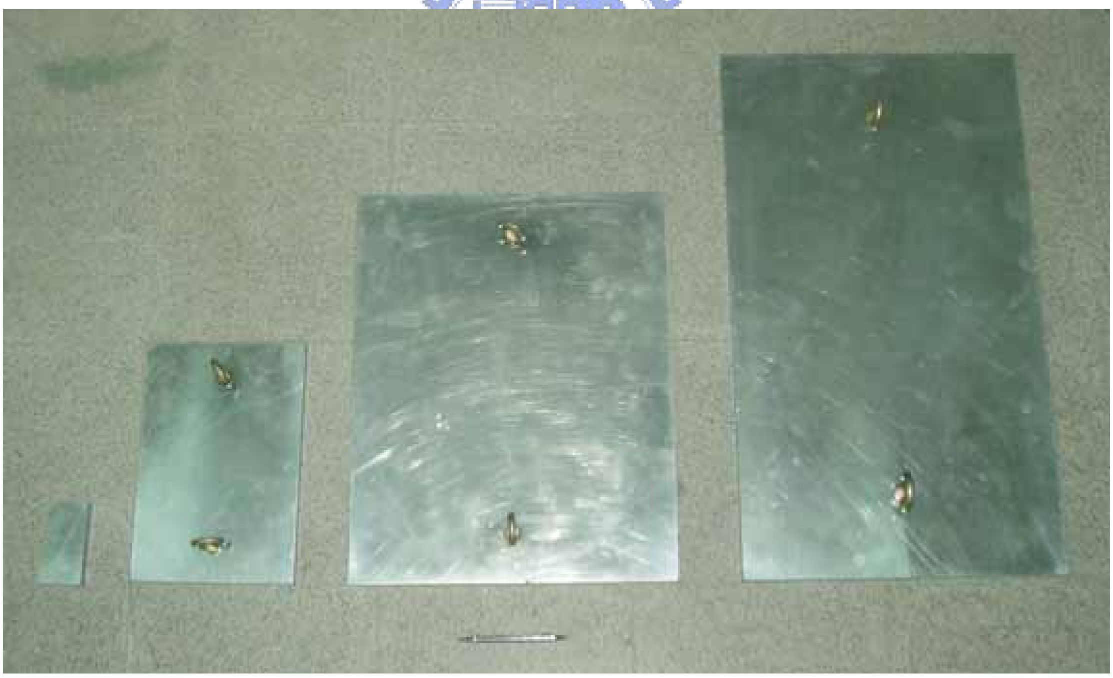

(b)

Fig. 4.7. Base spacing plates

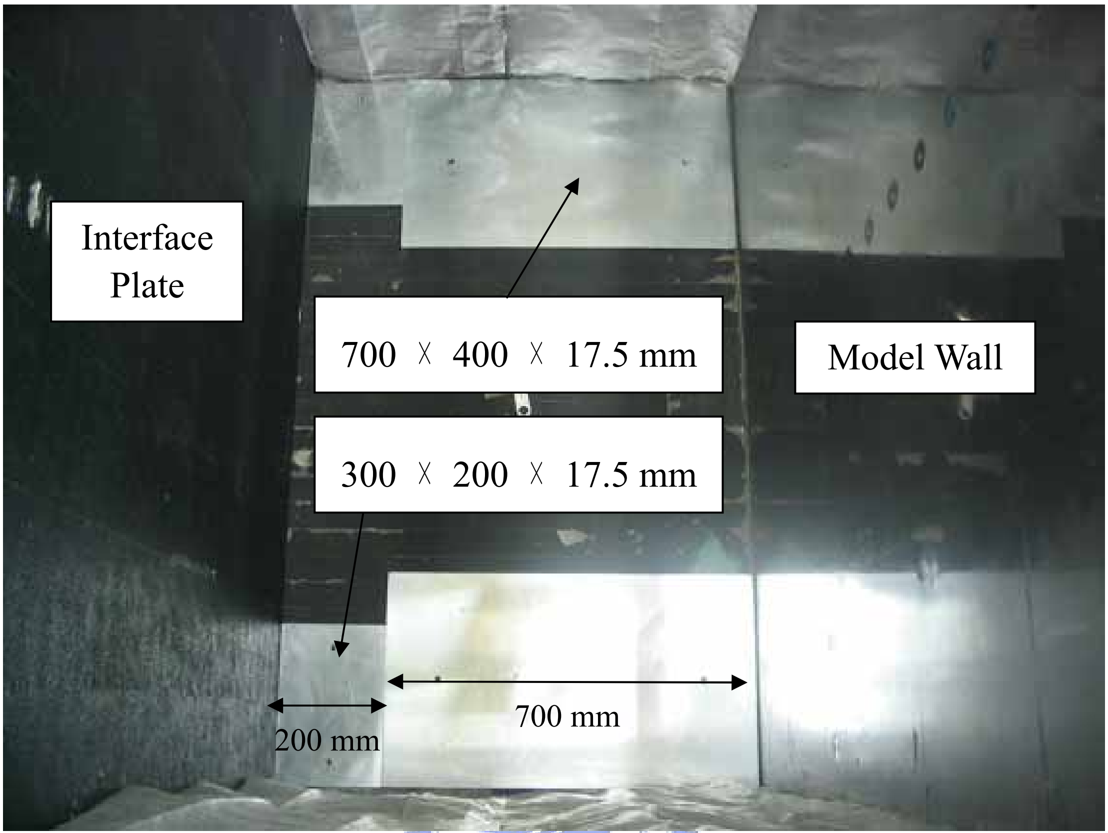

Fig. 4.8. Combination of base spacing plates for d = 900 mm

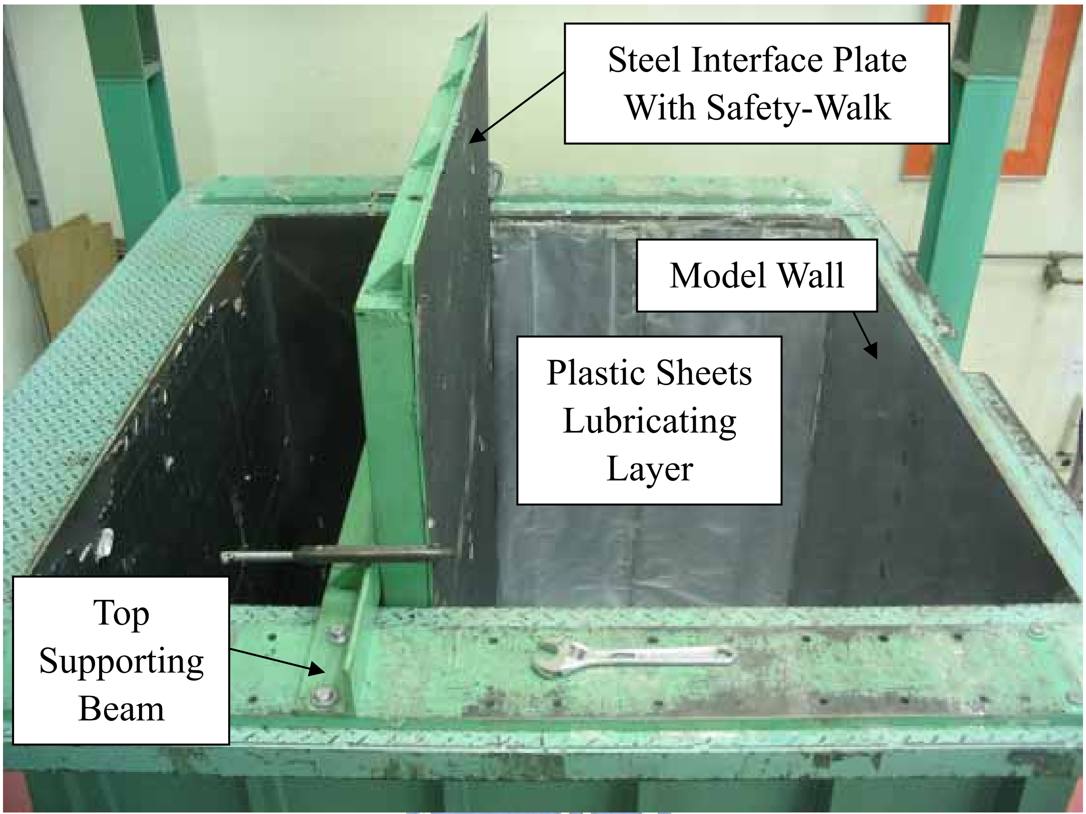

Fig. 4.9. For d = 900 mm between interface plate and model wall

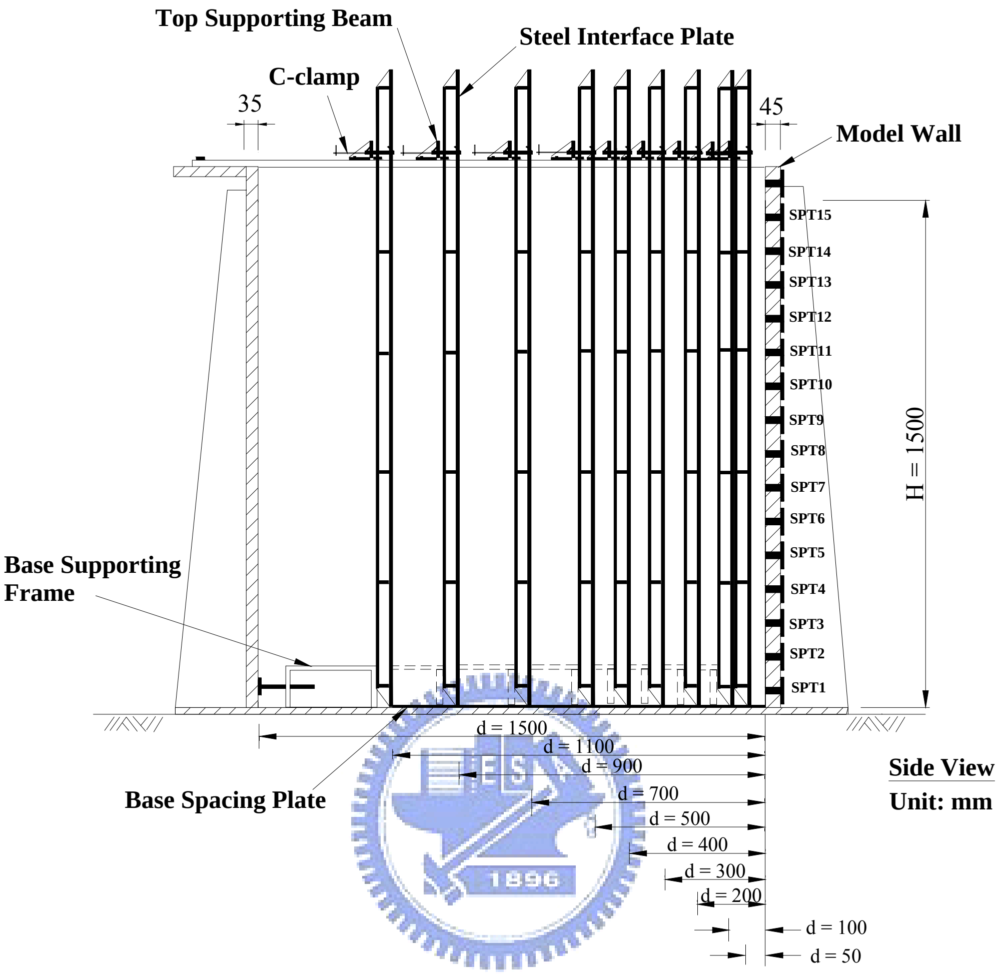

Fig. 4.10. Different spacing d between interface plate and model wall

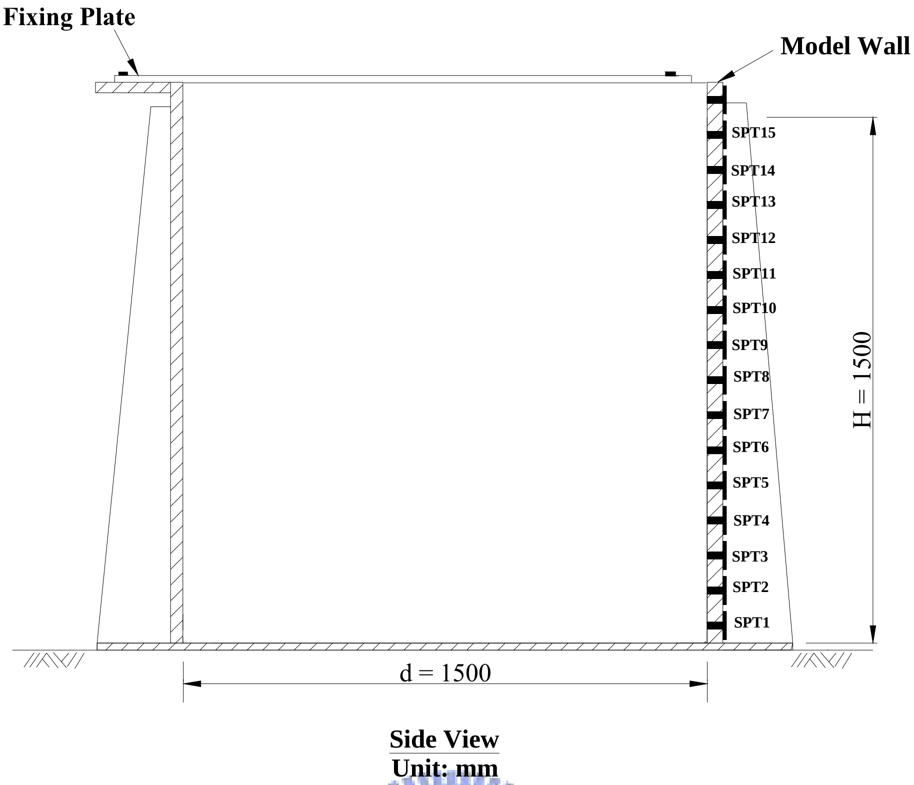

(a)

(b)

Fig. 4.11. For d = 1500 mm between interface plate and model wall

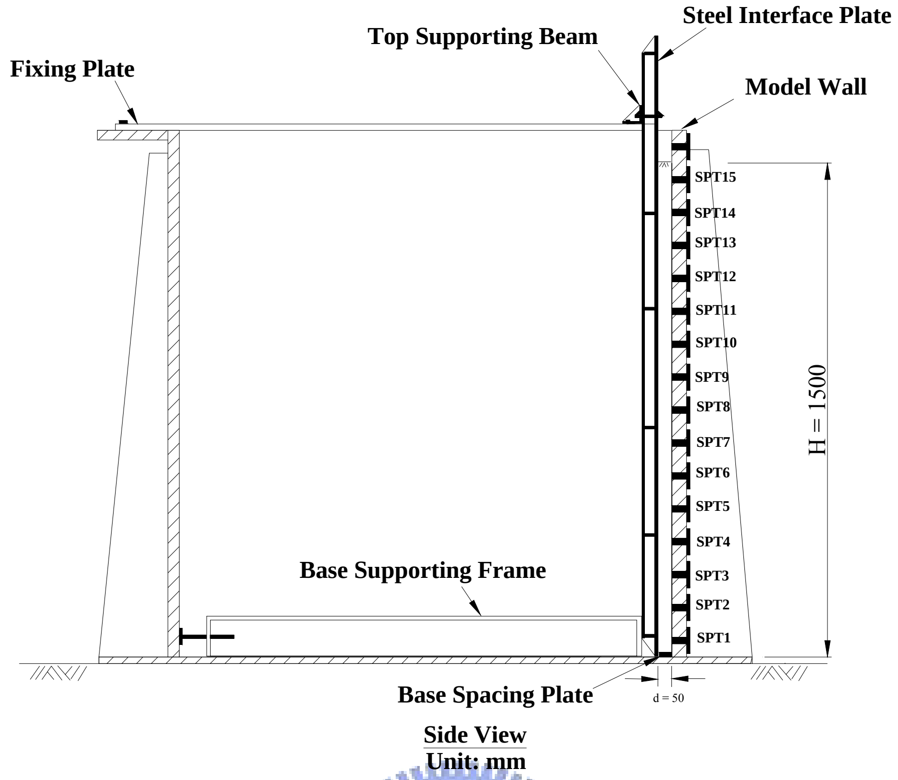

(a)

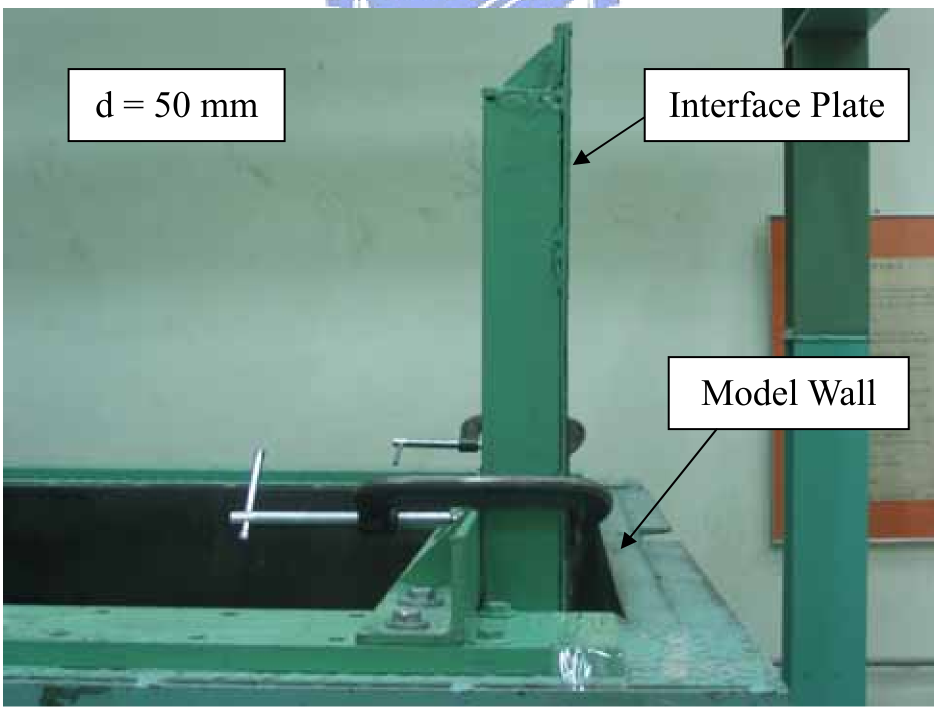

(b)

Fig. 4.12. For d = 50 mm between interface plate and model wall

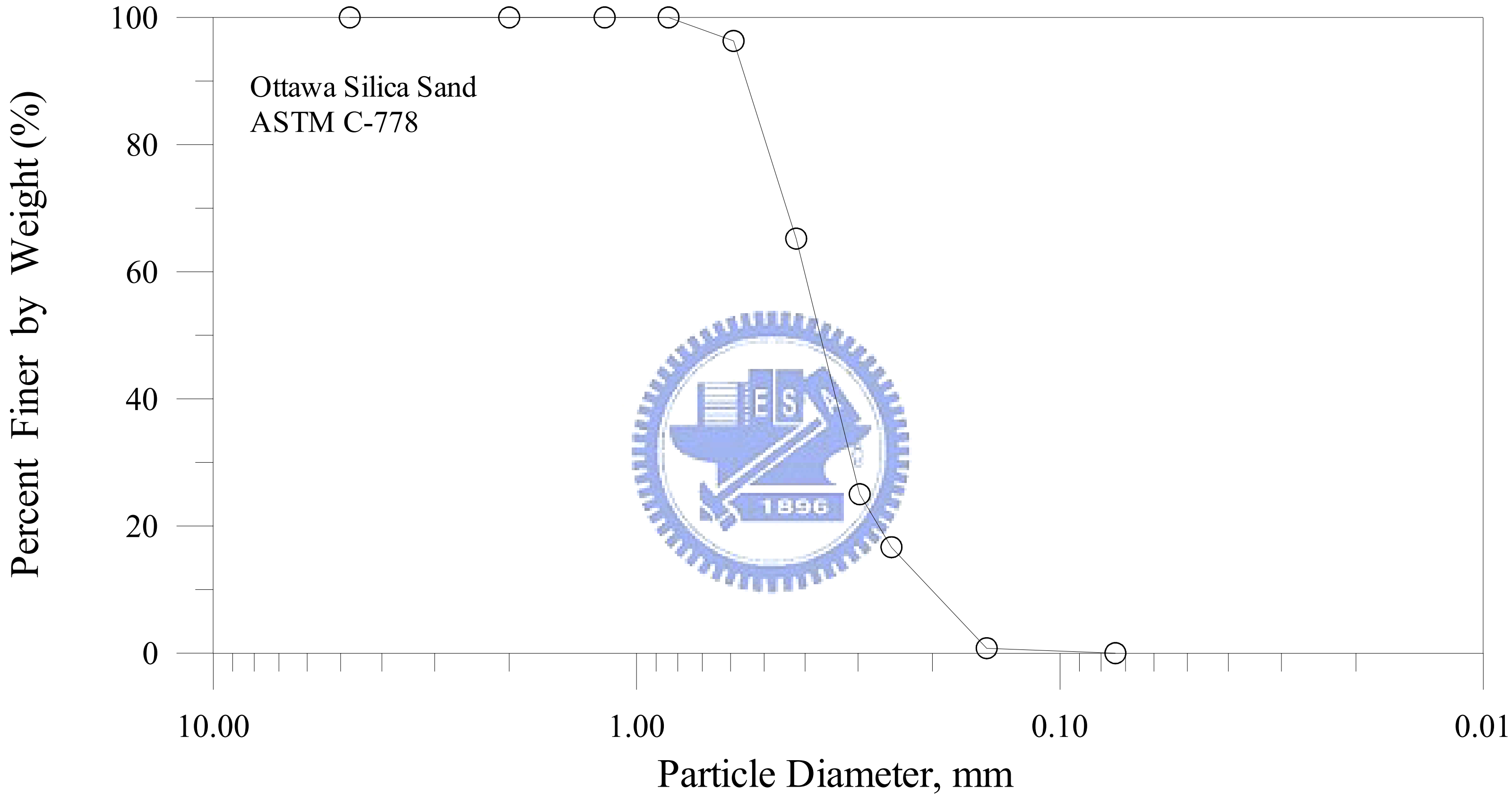

Fig. 5.1. Grain size distribution of Ottawa sand
(after Chen, 2001)

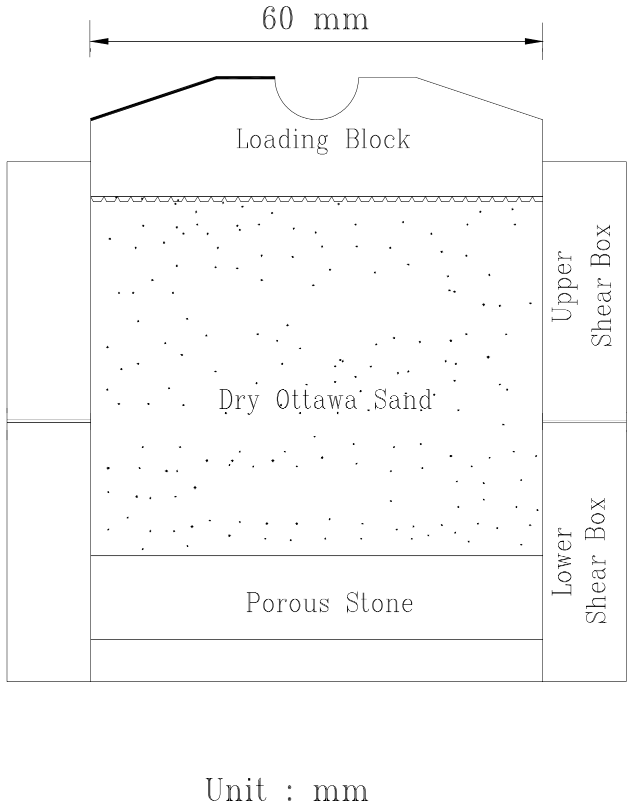

Fig. 5.2. Shear box of direct shear test device
(after Wu, 1992)

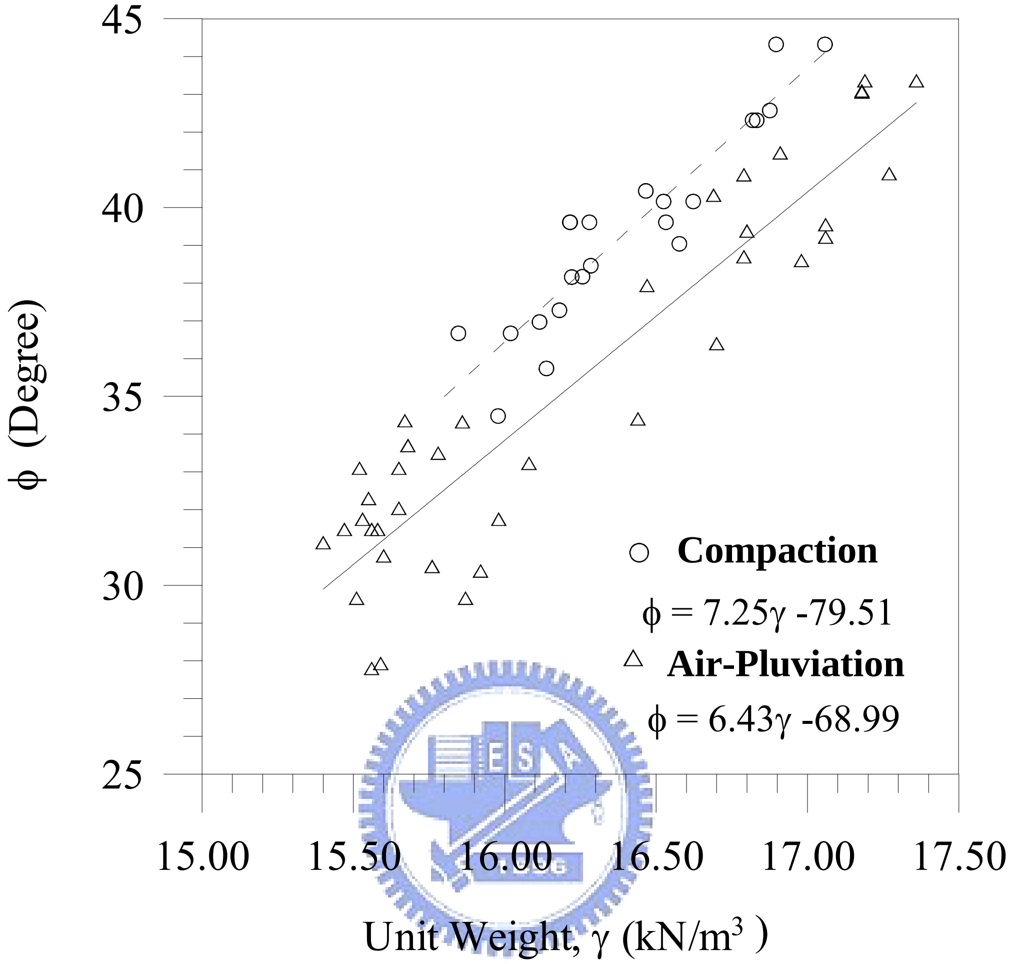

Fig. 5.3. Relationship between unit weight γ and internal friction angle φ (after Chang, 2000)

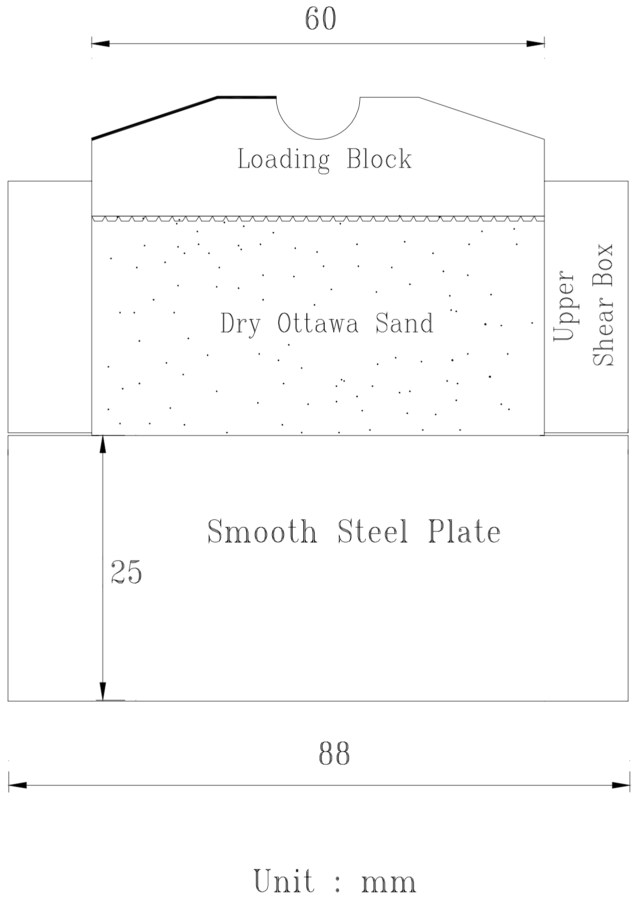

Fig. 5.4. Direct shear test arrangement to determinate wall friction angle δ_w (after Ho, 1999)

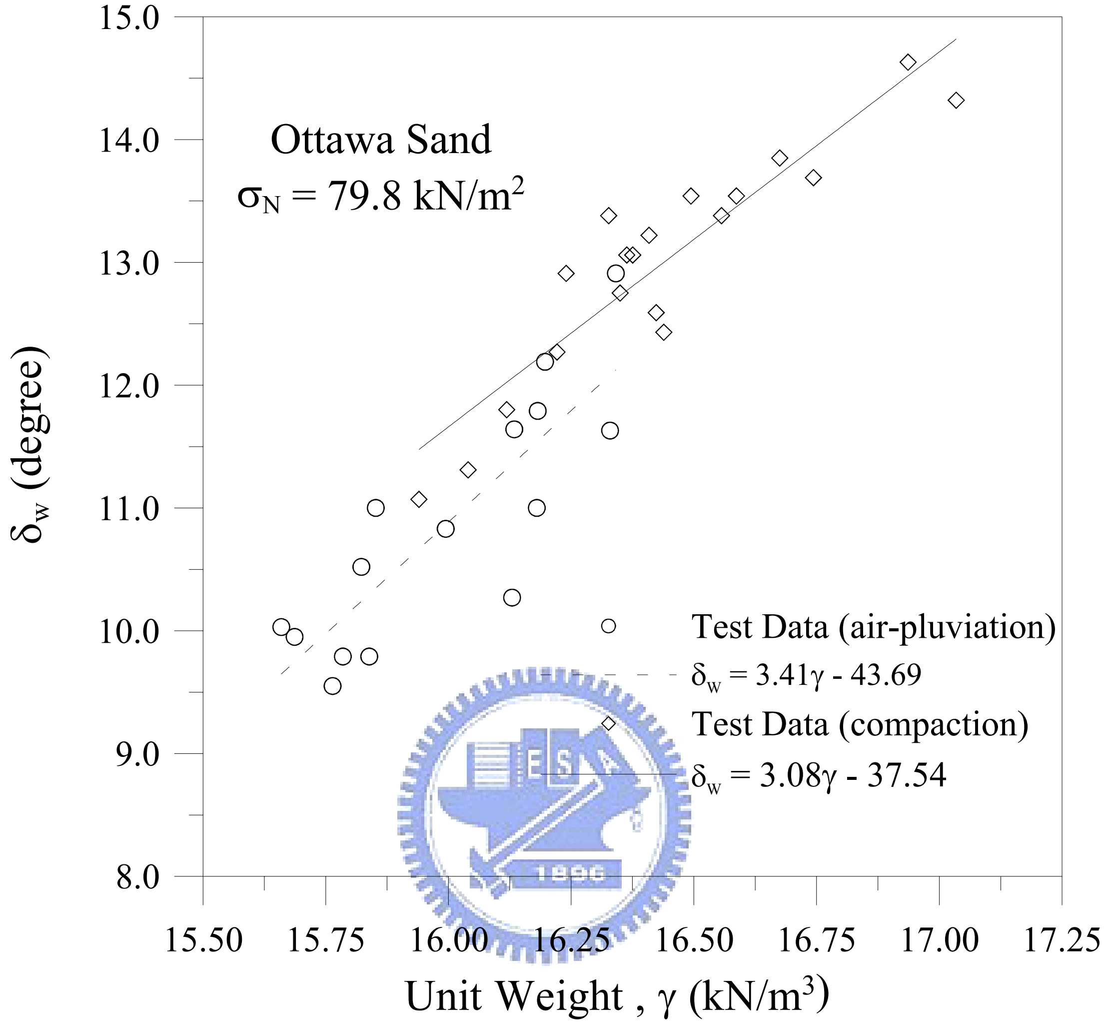

Fig. 5.5. Relationship between unit weight γ and wall friction angle δ_w (after Ho, 1999)

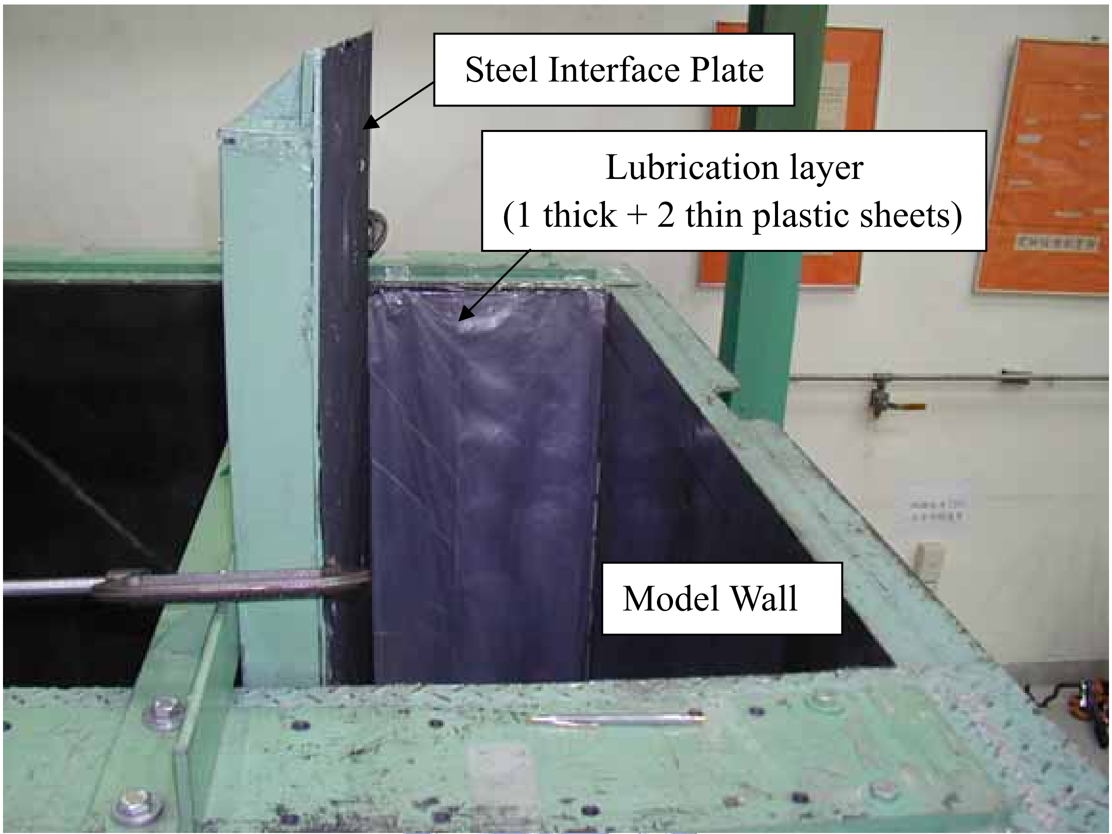

Fig. 5.6. Plastic sheets lubrication layer hung on the side wall

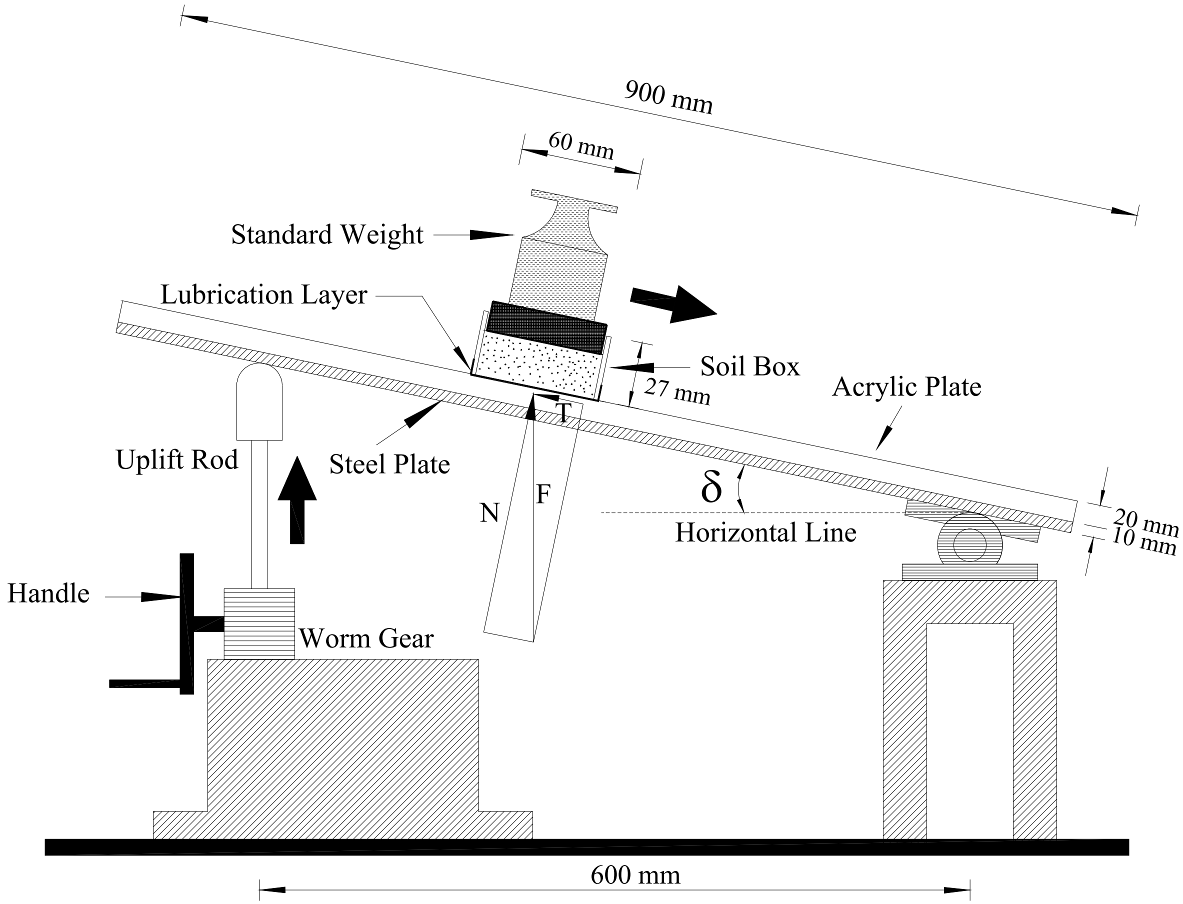

Fig. 5.7. Schematic diagram of sliding block test.
(after Fang et al., 2004)

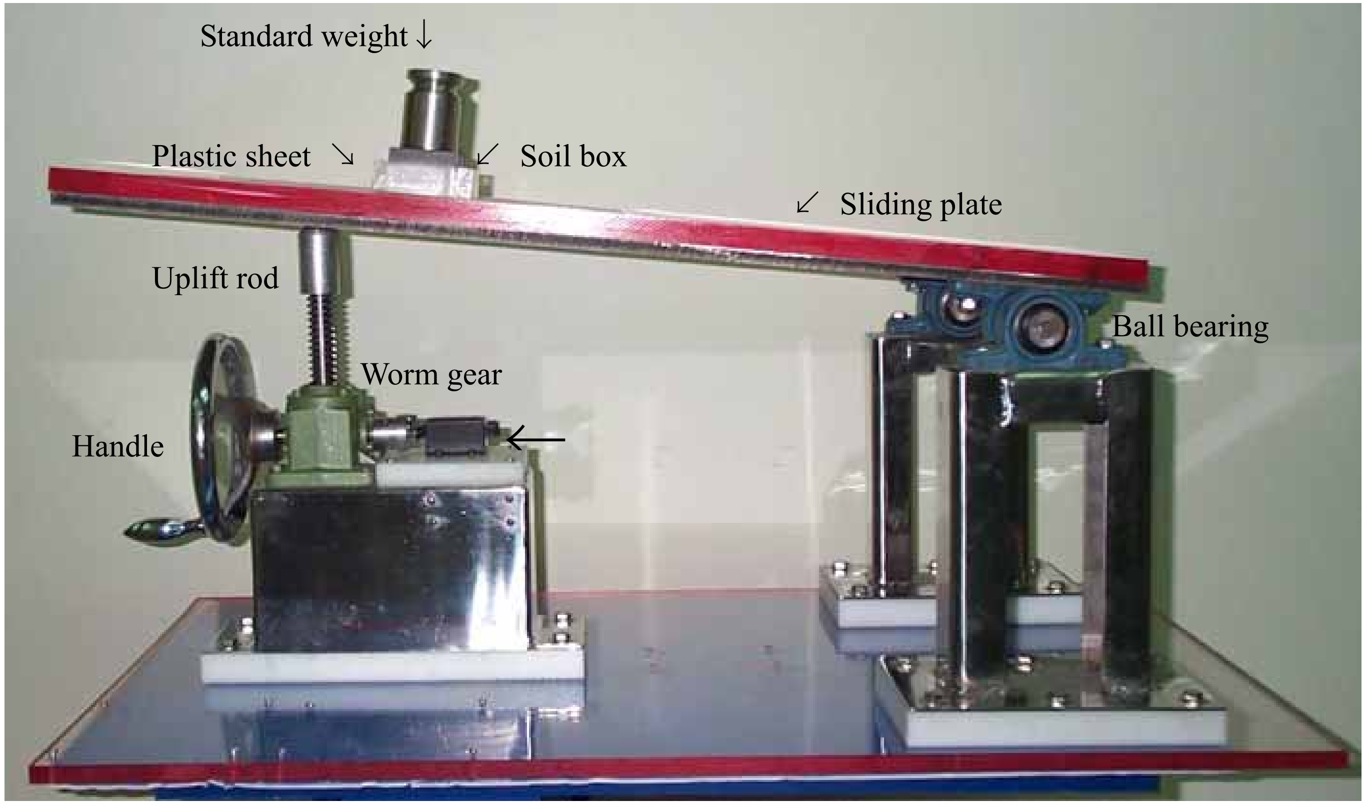

Fig. 5.8. Sliding block test apparatus

(after Fang et al., 2004)

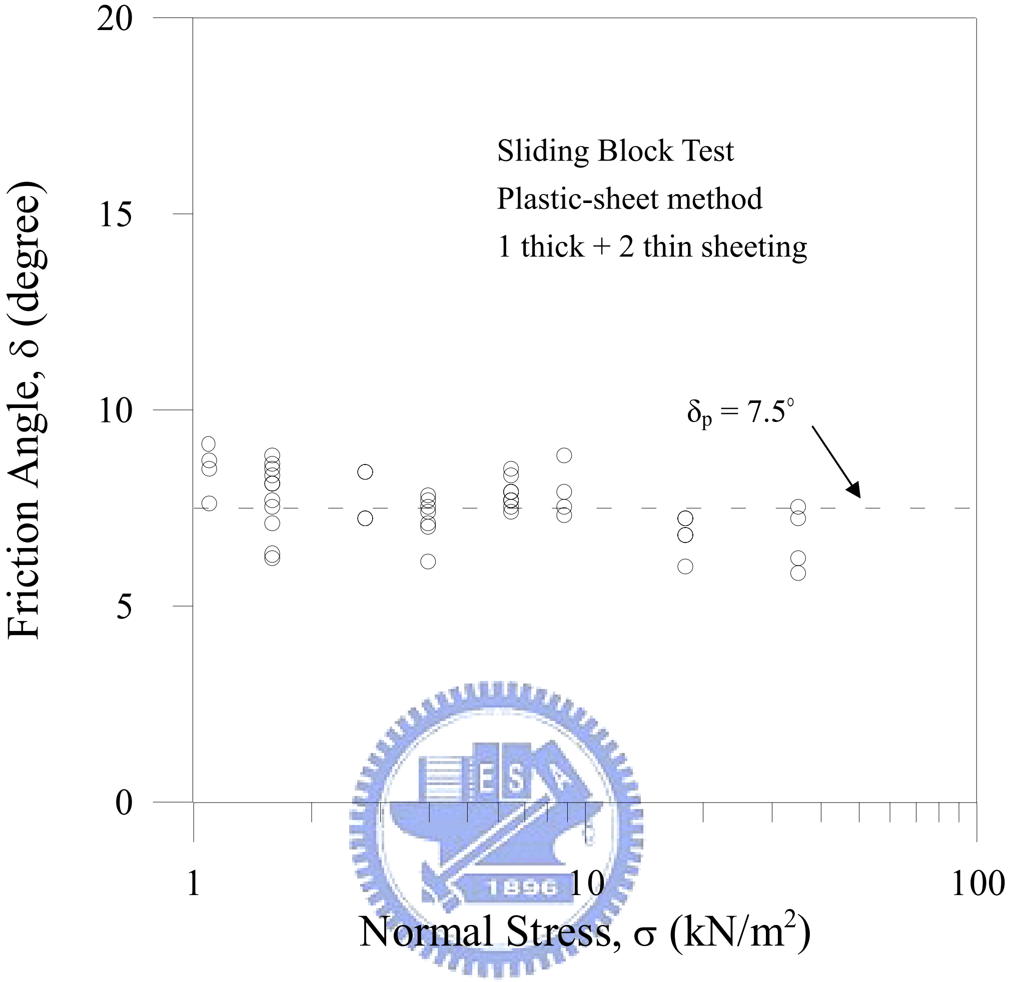

Fig. 5.9. Variation of interface friction angle δ_p with normal stress (after Fang et al., 2004)

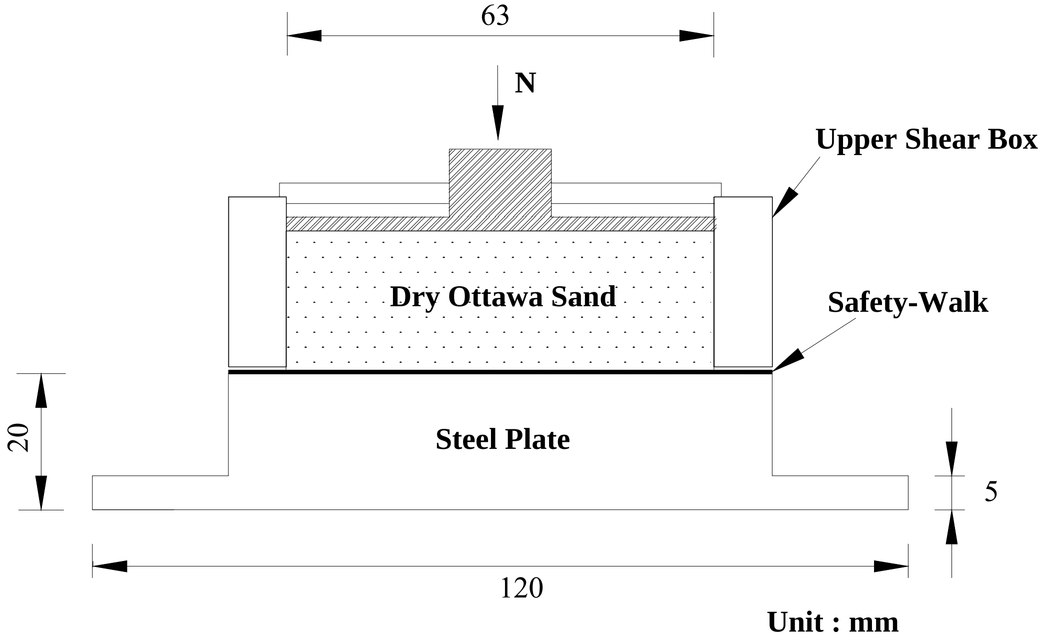

(a) Arrangement of direct shear test

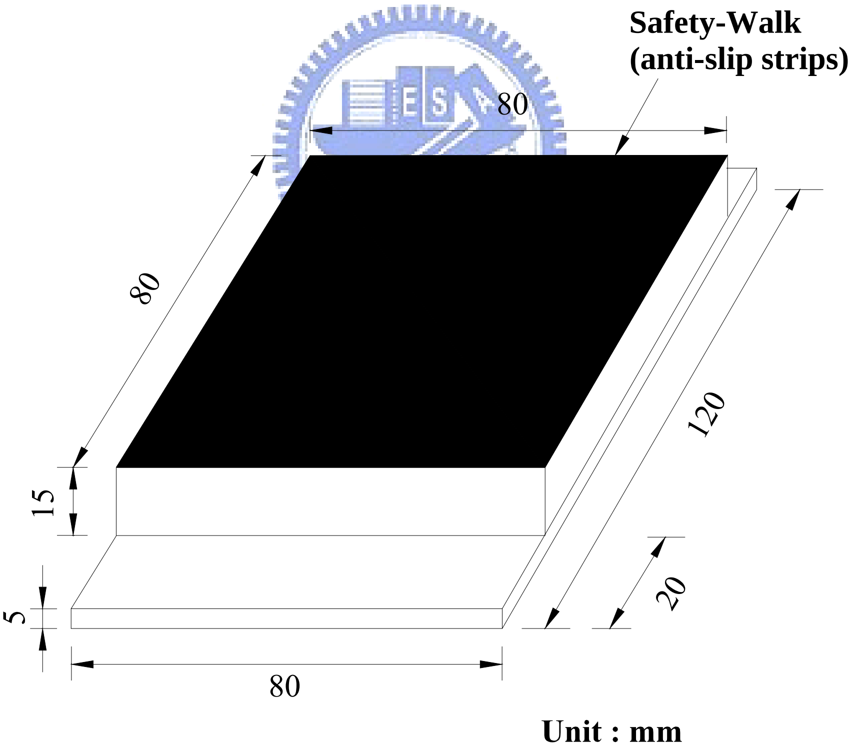

(b) Steel plate with Safety-Walk

Fig. 5.10. Direct shear test to determinate friction angle δ_i of the interface plate with Safety-Walk

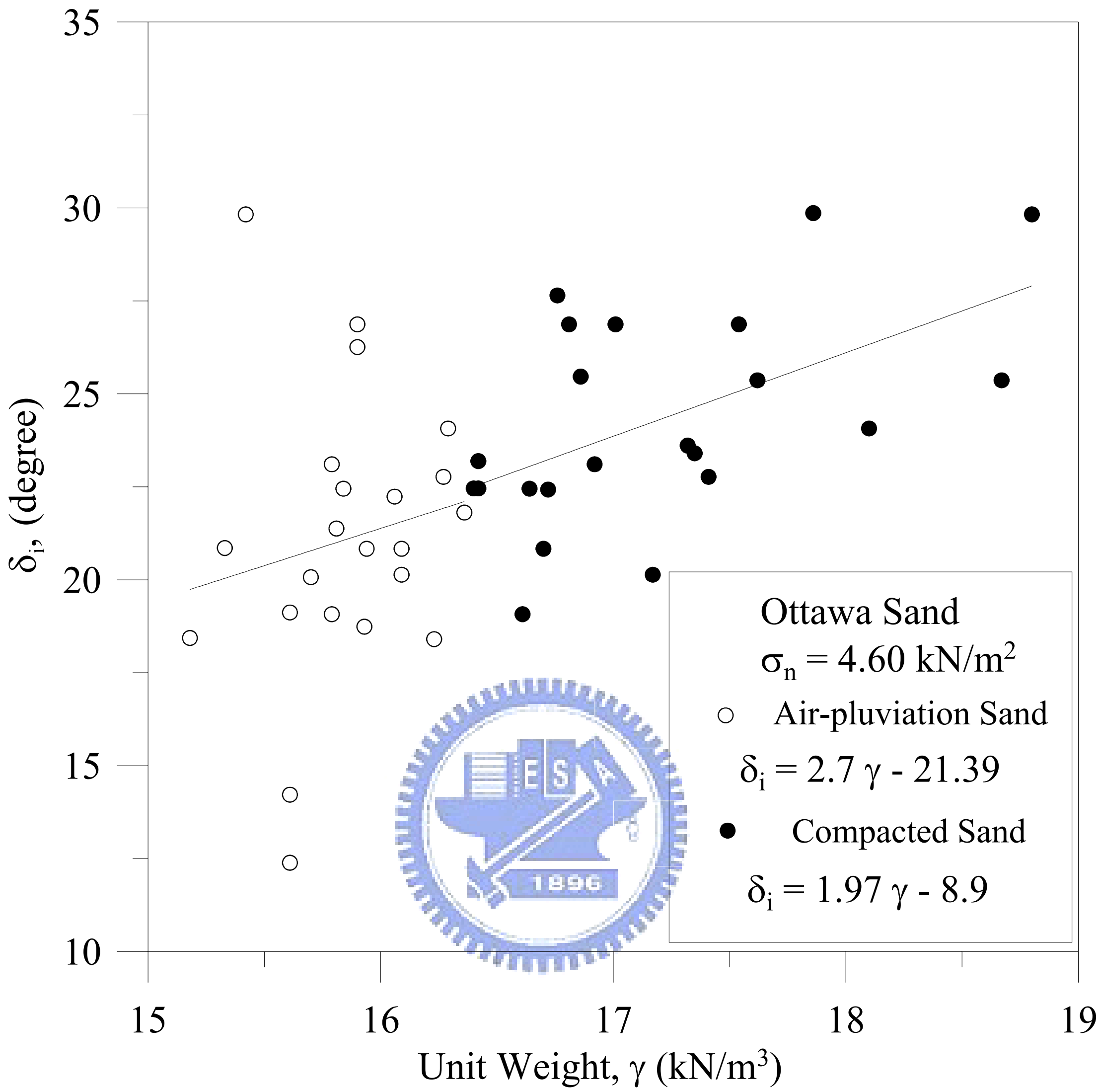

Fig. 5.11. Relationship between unit weight γ and interface plate friction angle δ_i

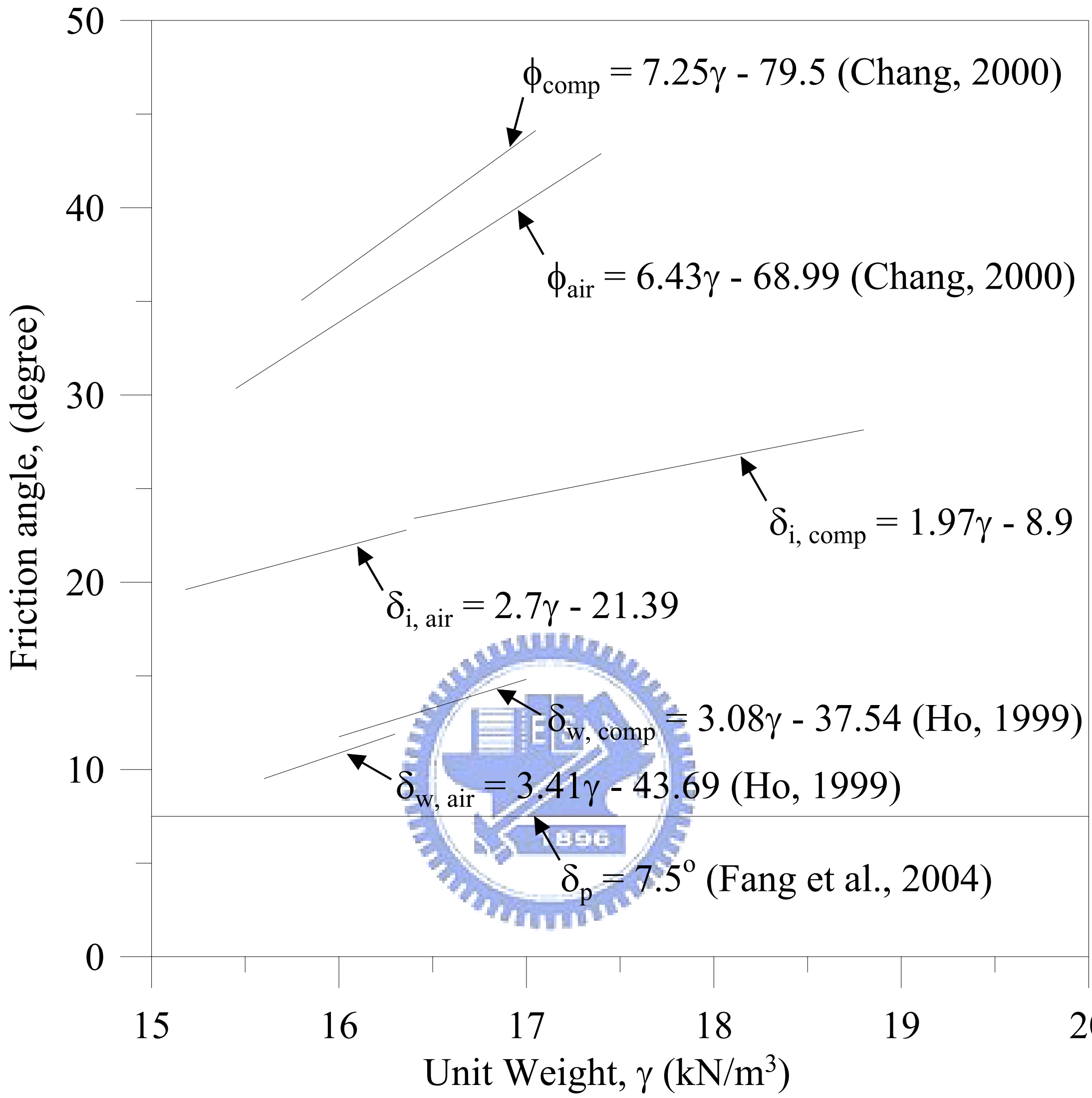

Fig. 5.12. Relationship between unit weight γ and friction angle for different types of interfaces

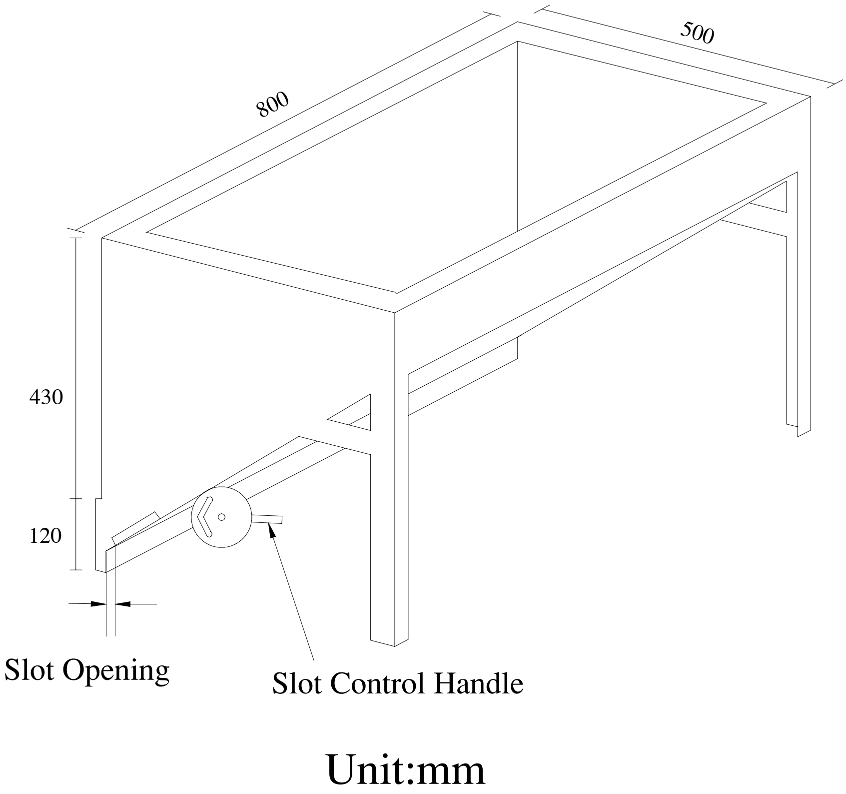

(a)

(b)

Fig. 5.13. Soil hopper

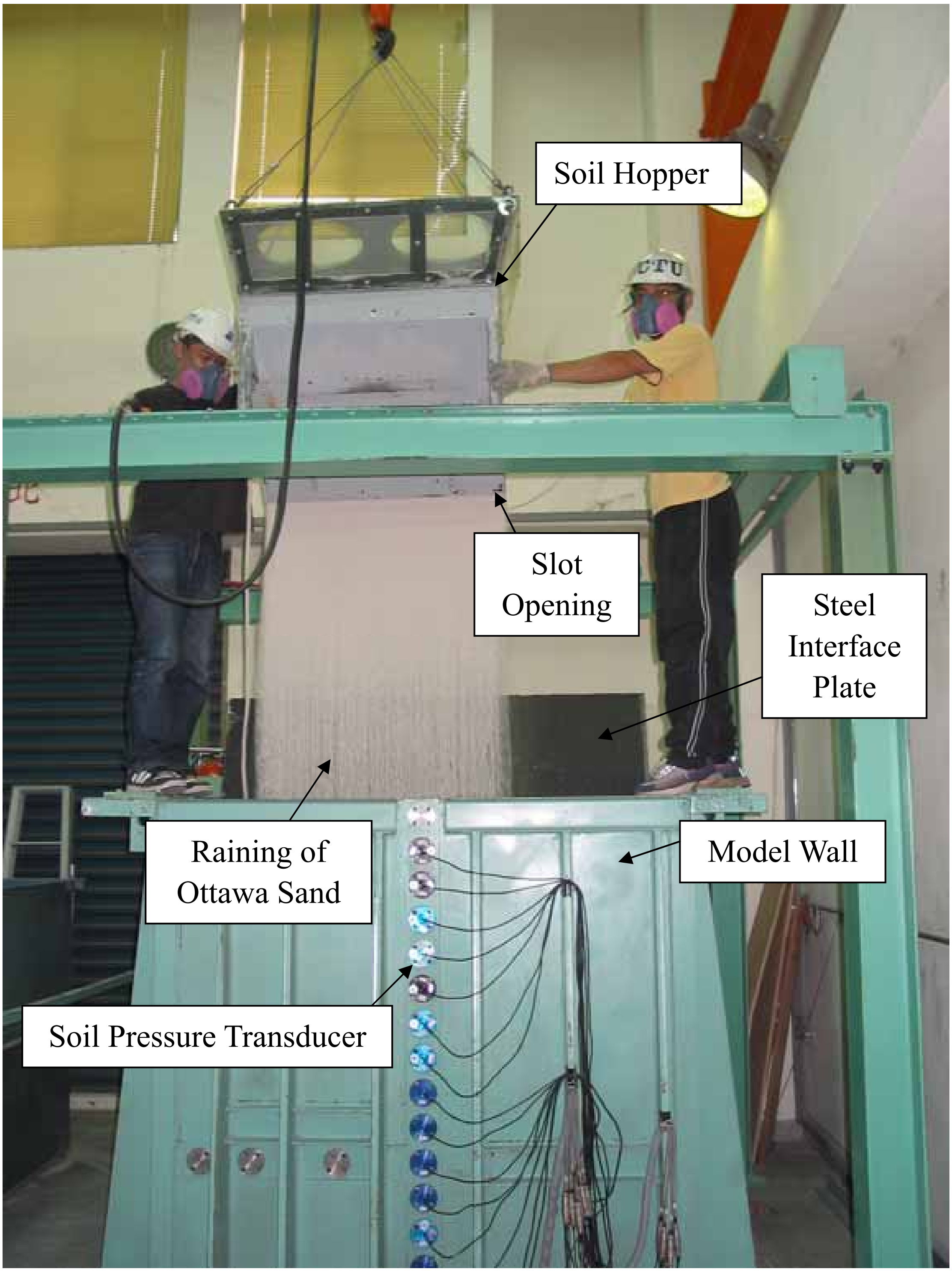

Fig. 5.14. Air-pluviation of the Ottawa sand into soil bin

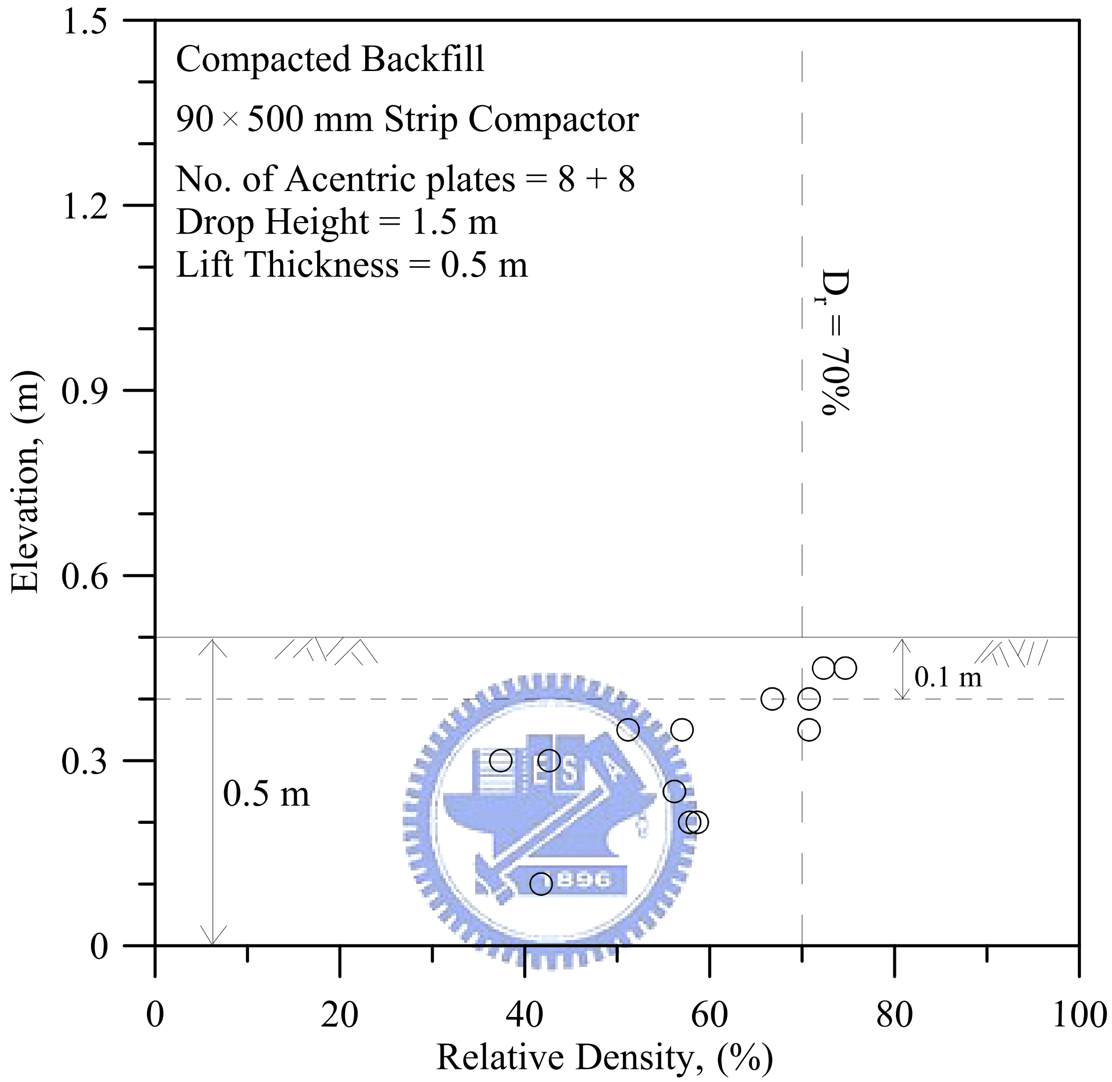

Fig. 5.15. Distribution of soil density with depth for sand compacted with the 90 mm ╳ 500 mm strip compactor

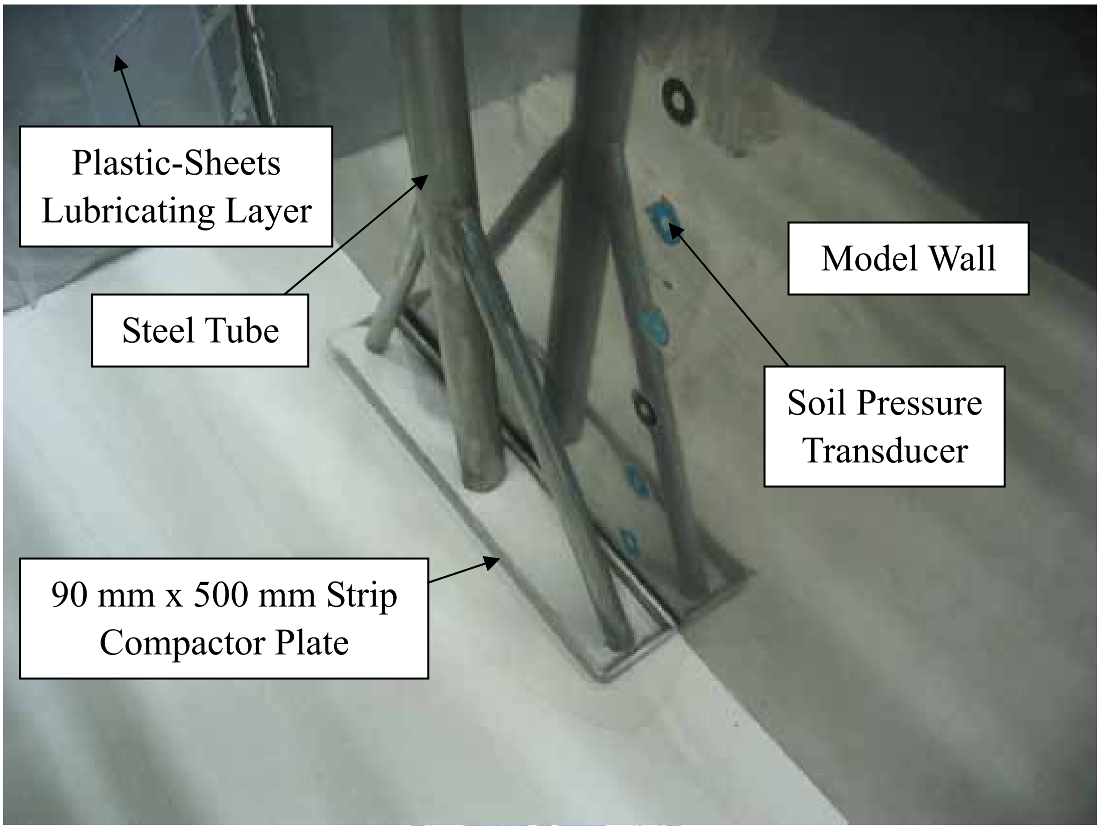

Fig. 5.16. Backfill compacted with 90 mm × 500 mm strip compactor

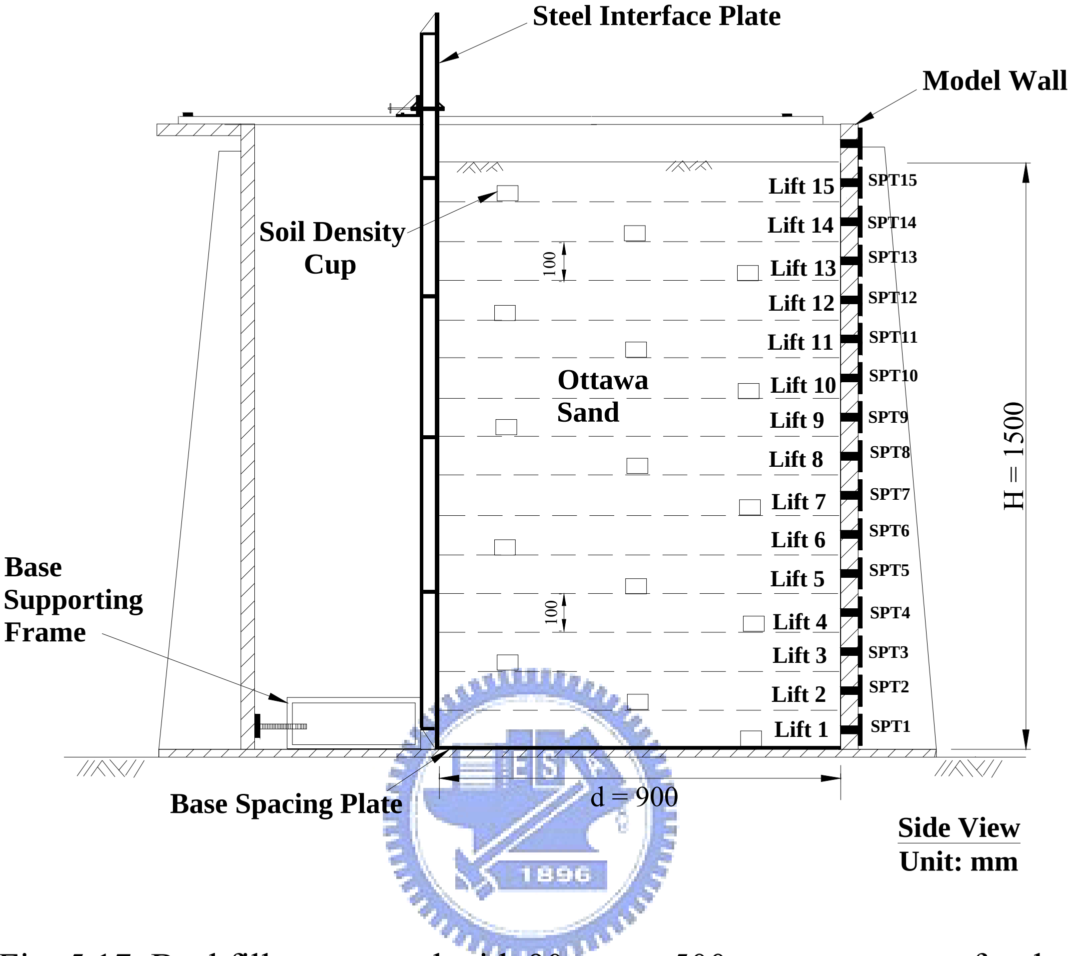

Fig. 5.17. Backfill compacted with 90 mm × 500 mm compactor for d = 900 mm

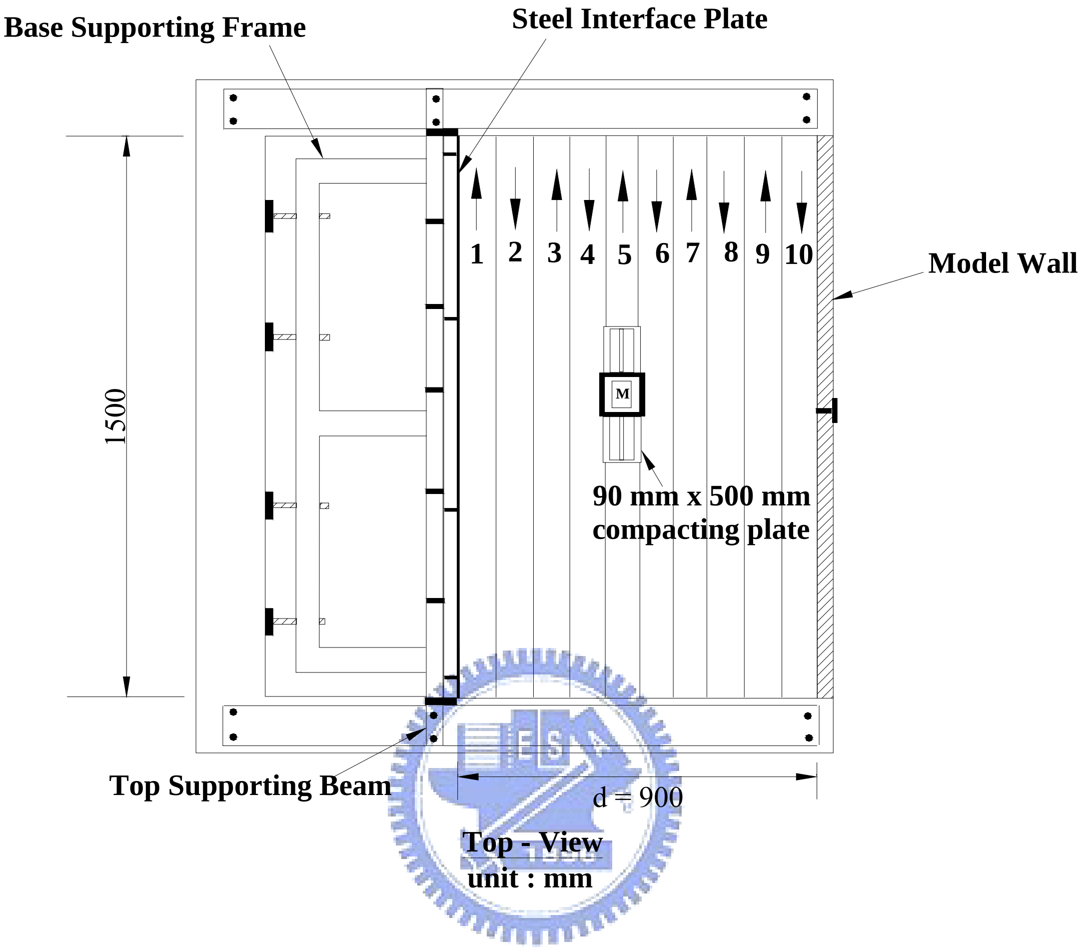

Fig. 5.18. Backfill compacted with 90 mm × 500 mm compactor in 10 lanes

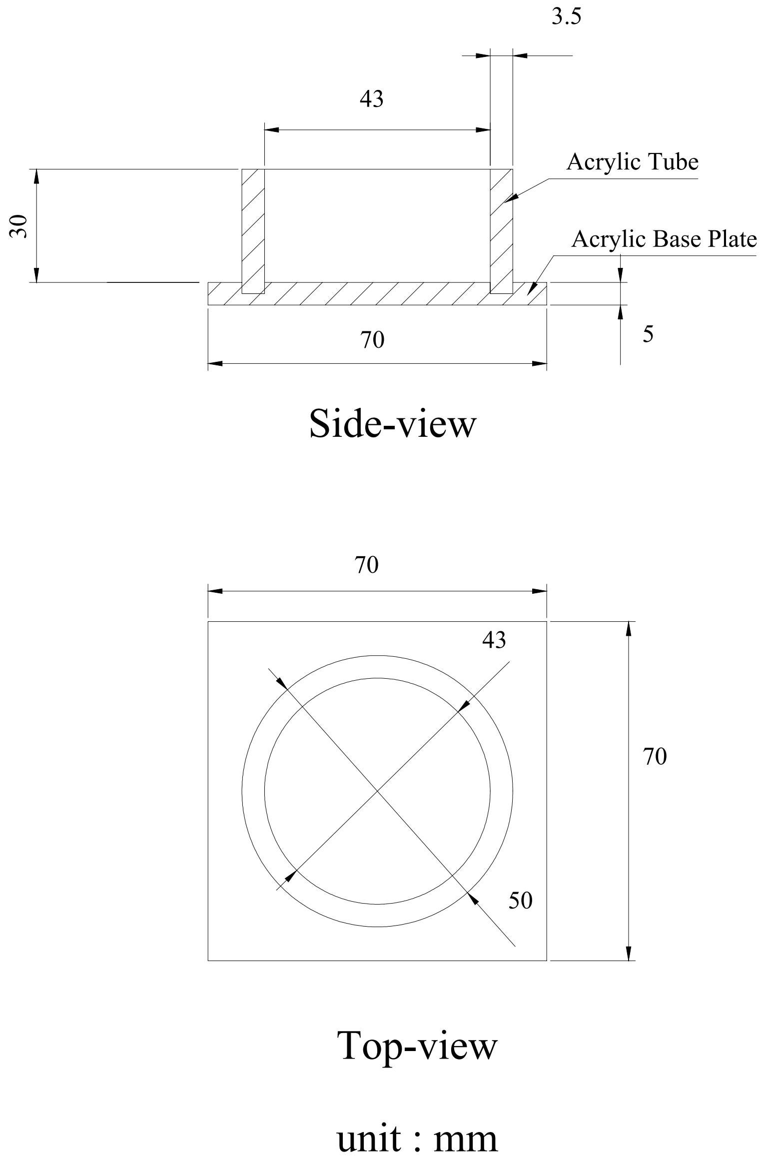

Fig. 5.19. Dimensions of soil density cup

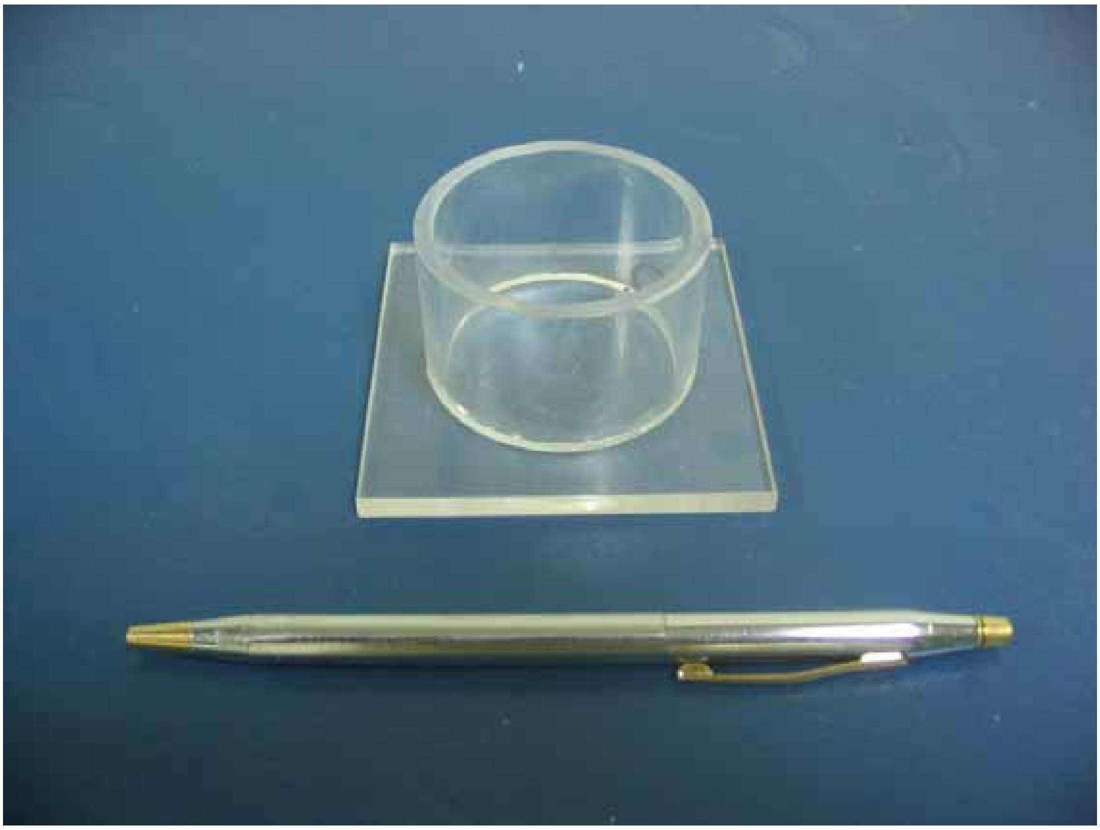

Fig. 5.20. Soil density cup

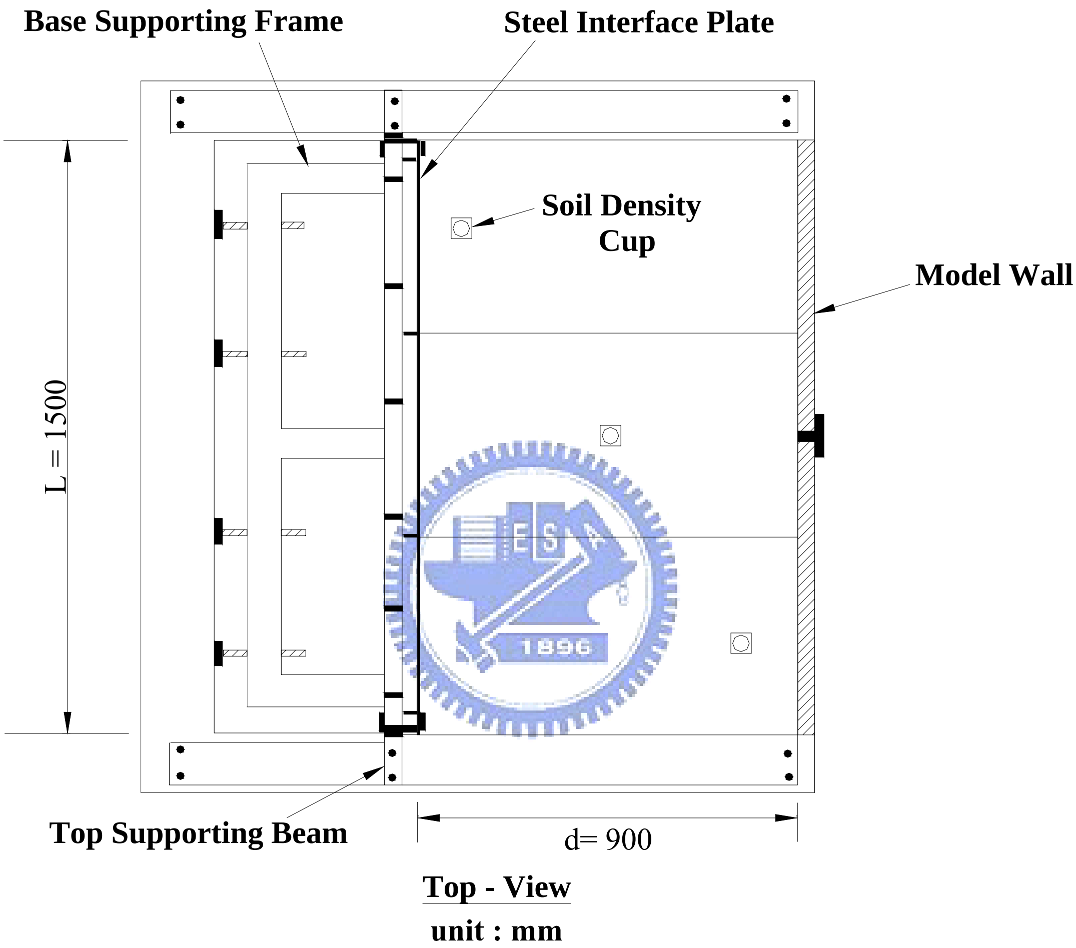

Fig. 5.21. Locations of soil density control cups at the same elevation

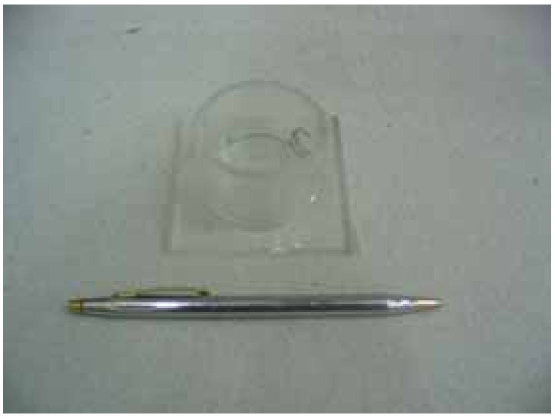

(a) Placement of soil density cup

(b) Cup filled and Buried in Backfill

(c) Compaction of soil

(d) Soil density dug out

(e) Soil mass in cup weighted

$$\gamma_d = \frac{W_s}{V}$$

(f) Calculation of dry density

Fig. 5.22. Procedure of density control test

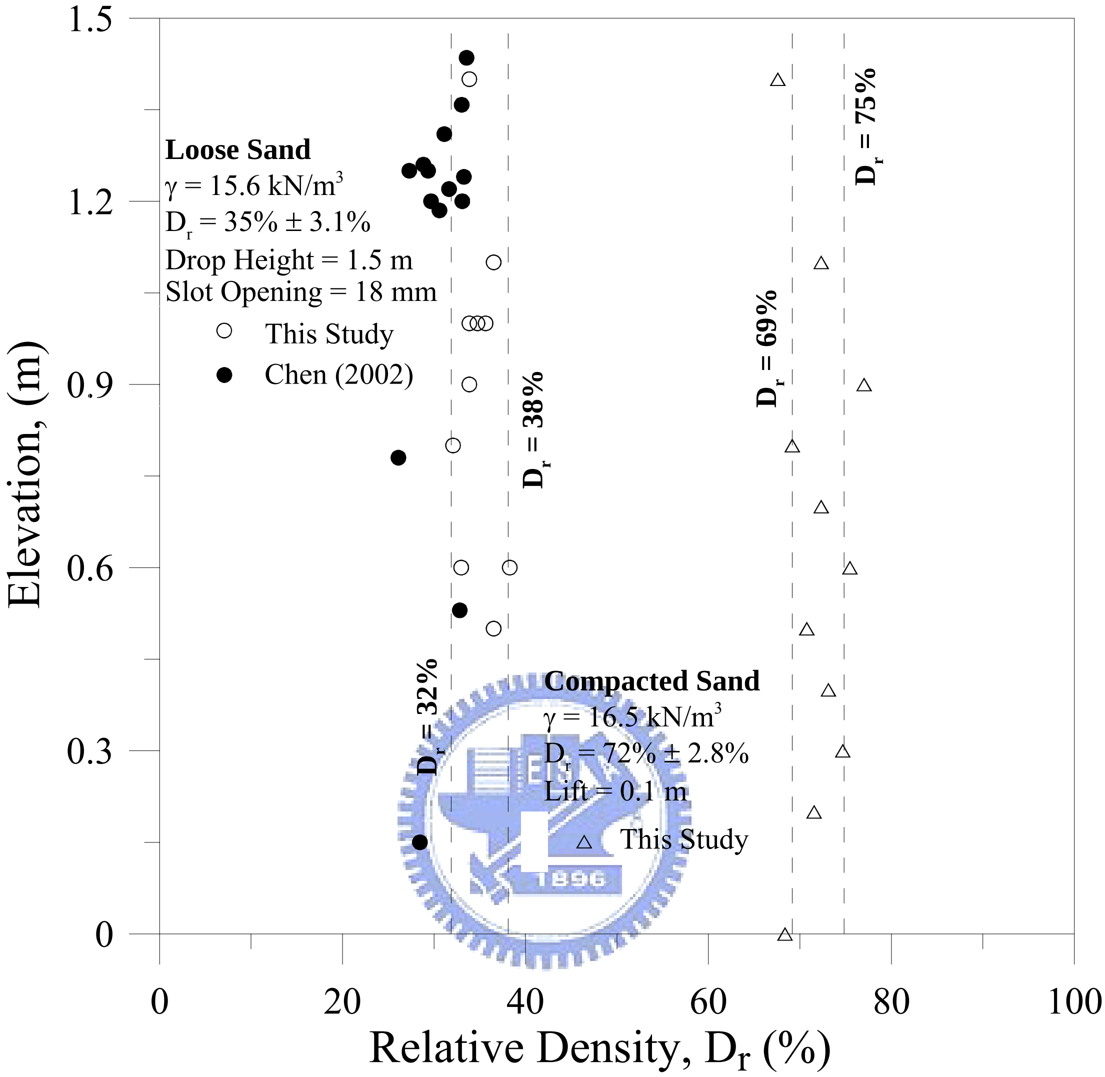

Fig. 5.23. Distribution of soil density for loose and compacted sand

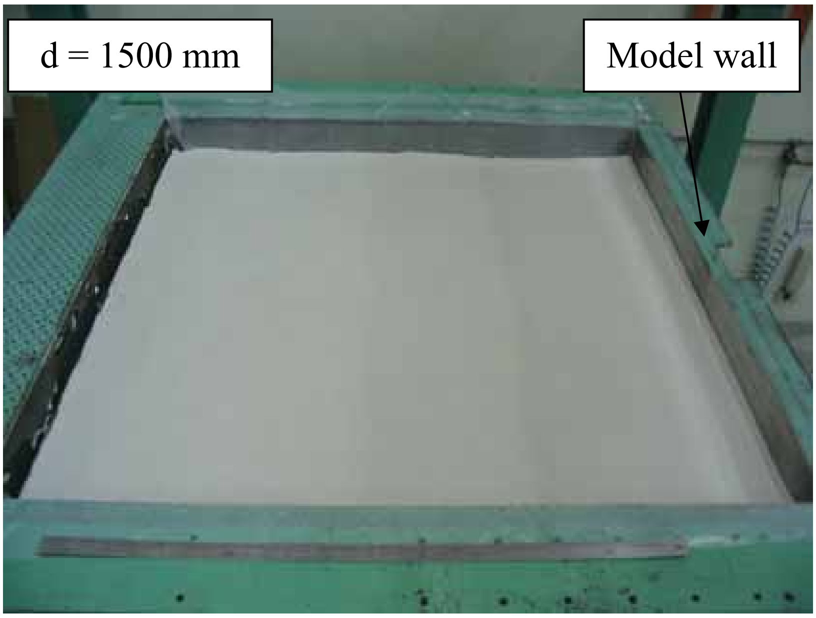

(a)

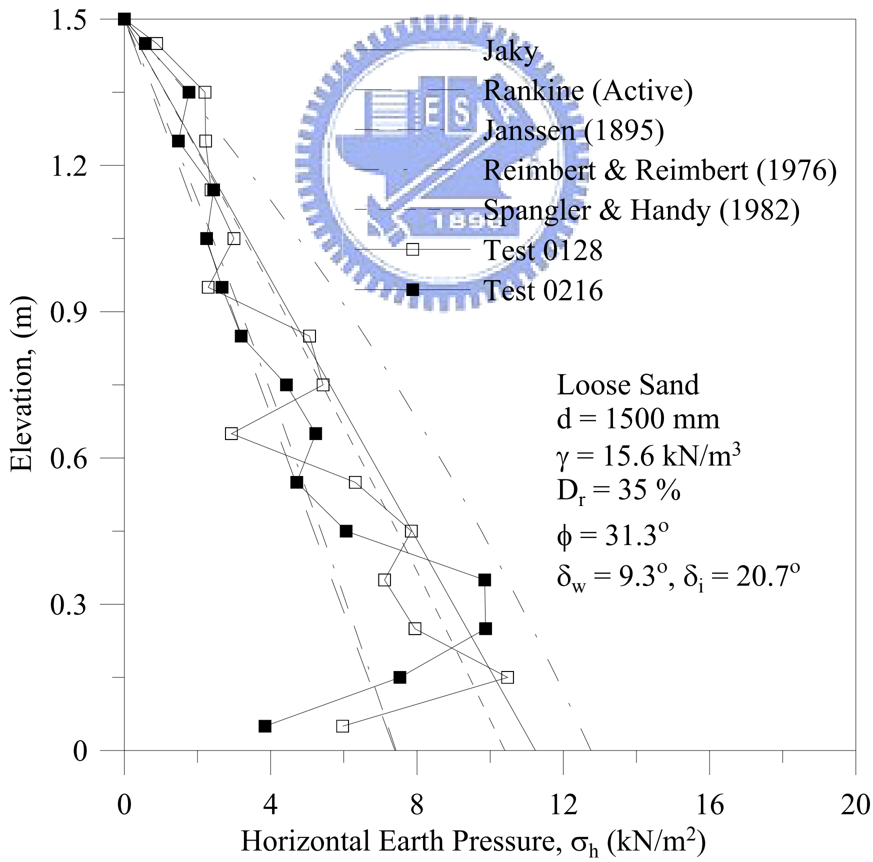

(b)

Fig. 6.1. Distribution of horizontal earth pressure for loose sand with d = 1500 mm

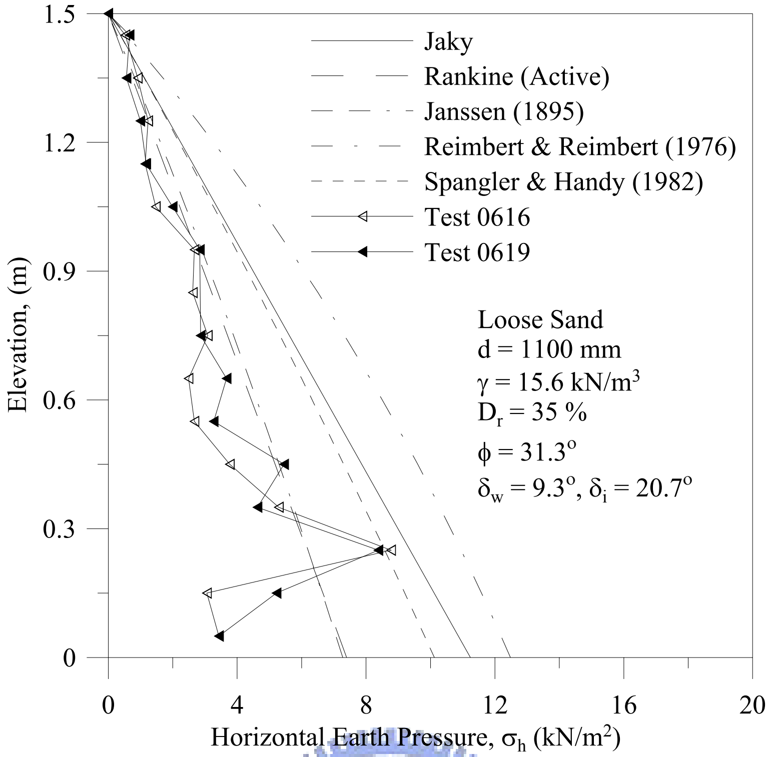

Fig. 6.2. Distribution of horizontal earth pressure for loose sand with d = 1100 mm

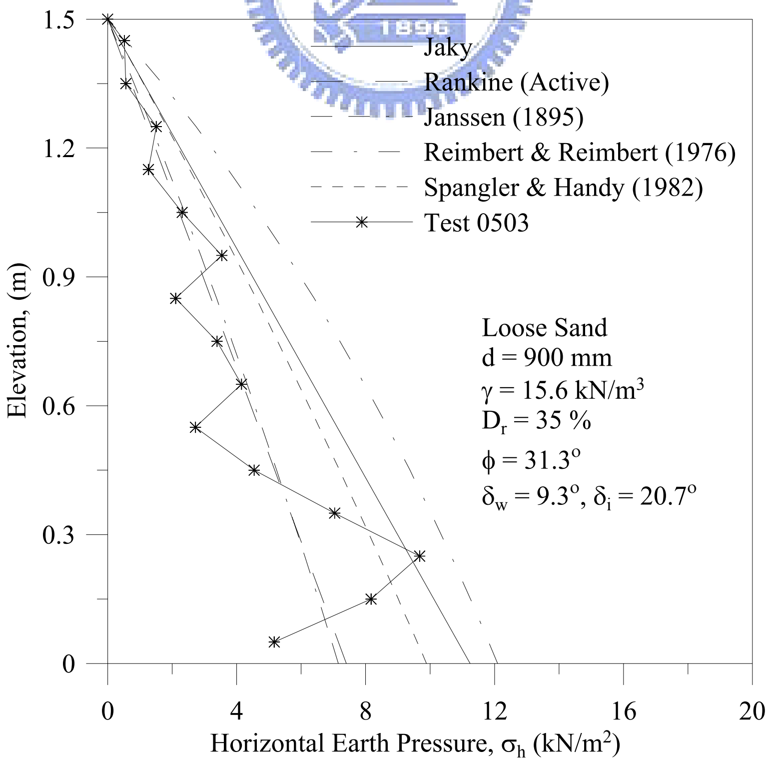

Fig. 6.3. Distribution of horizontal earth pressure for loose sand with d = 900 mm

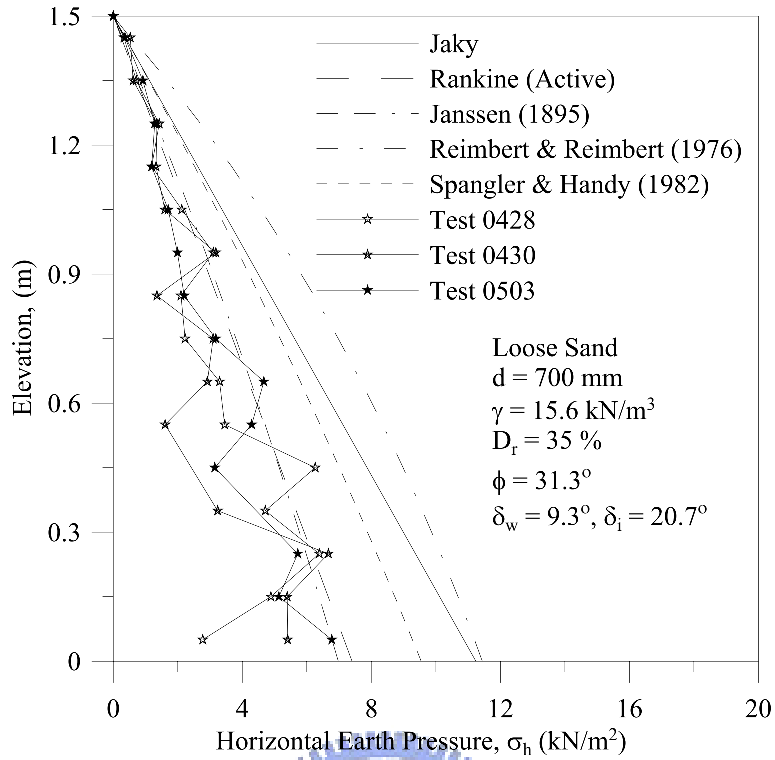

Fig. 6.4. Distribution of horizontal earth pressure for loose sand with d = 700 mm

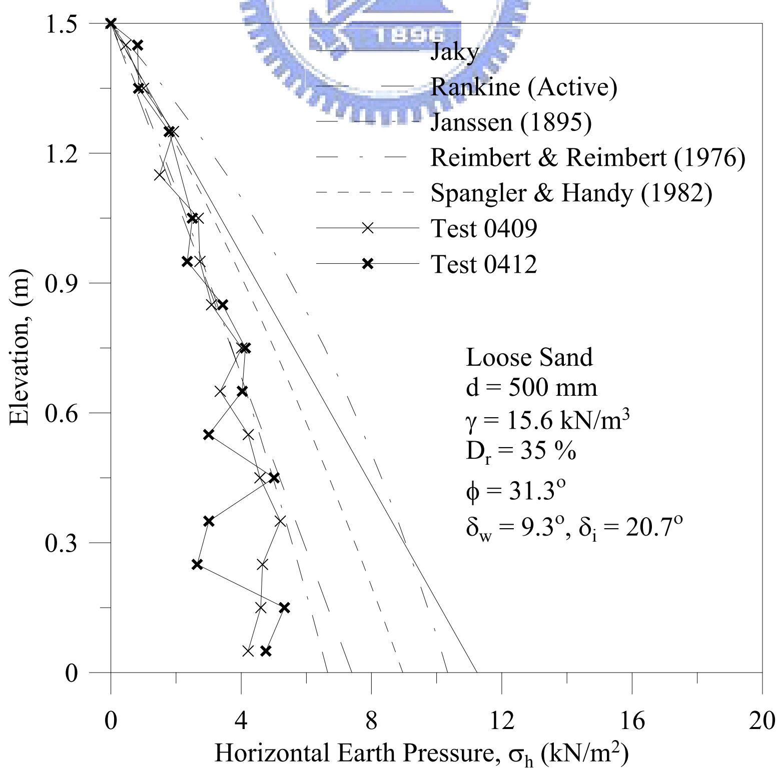

Fig. 6.5. Distribution of horizontal earth pressure for loose sand with d = 500 mm

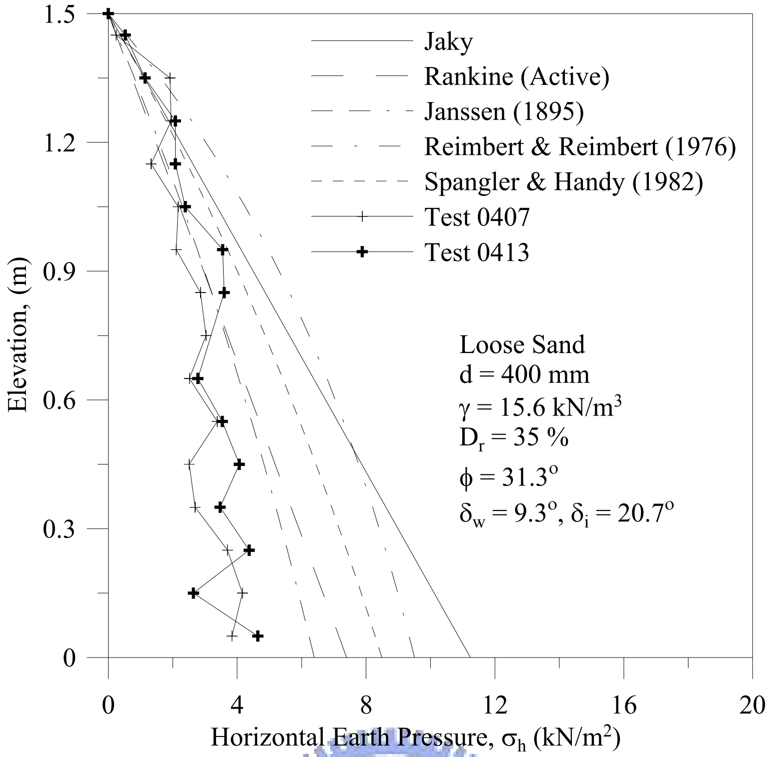

Fig. 6.6. Distribution of horizontal earth pressure for loose sand with d = 400 mm

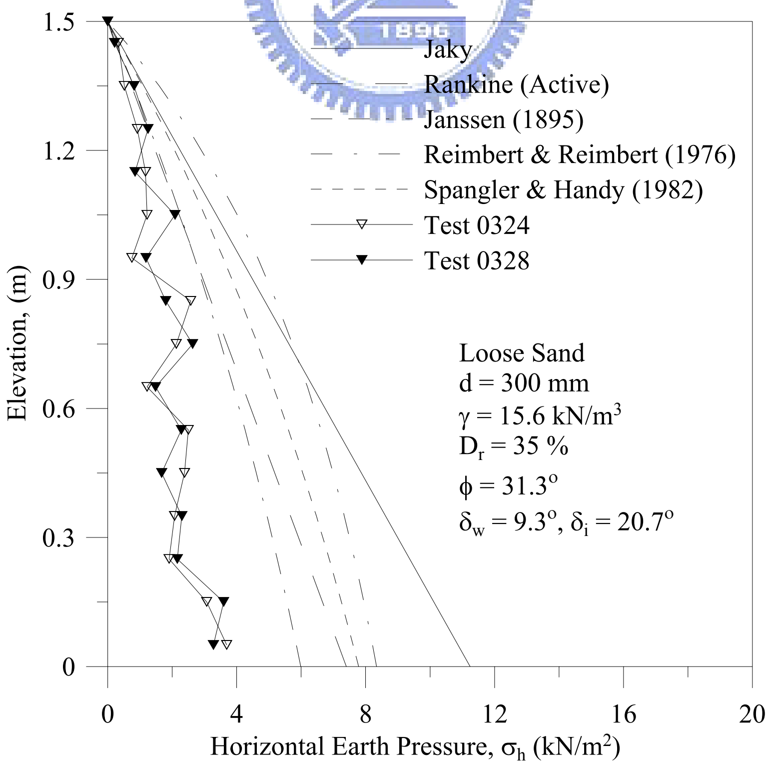

Fig. 6.7. Distribution of horizontal earth pressure for loose sand with d = 300 mm

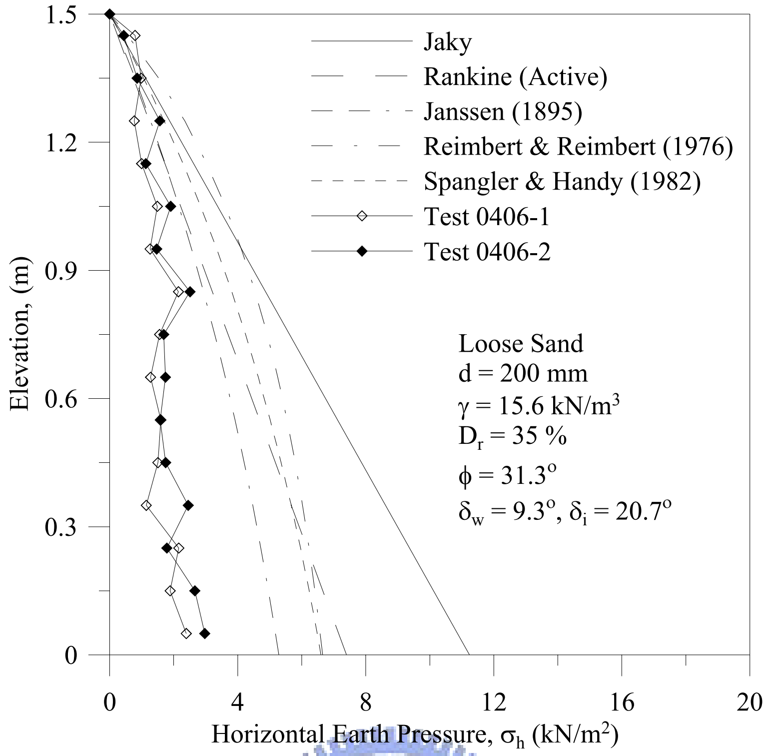

Fig. 6.8. Distribution of horizontal earth pressure for loose sand with d = 200 mm

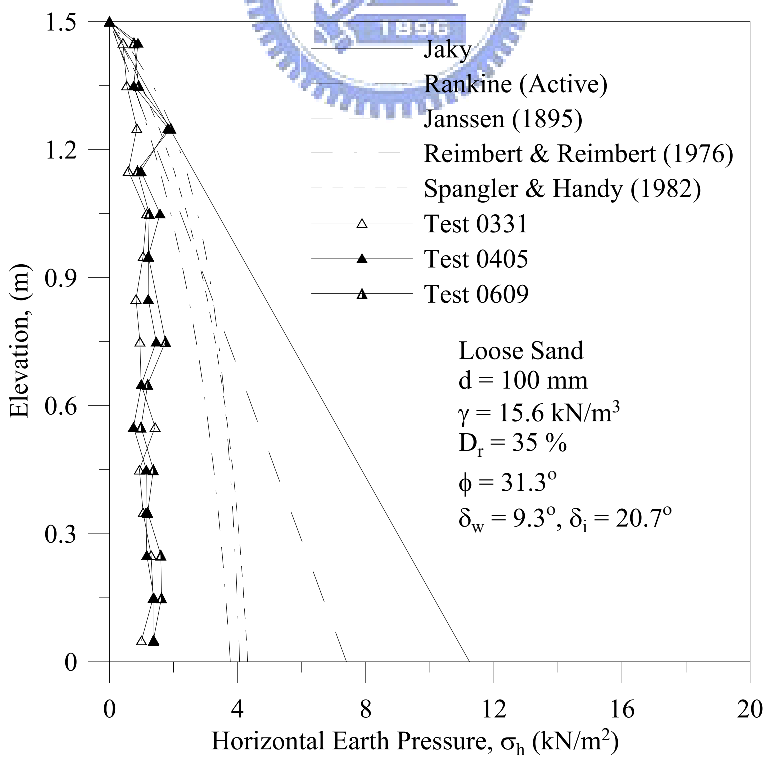

Fig. 6.9. Distribution of horizontal earth pressure for loose sand with d = 100 mm

(a)

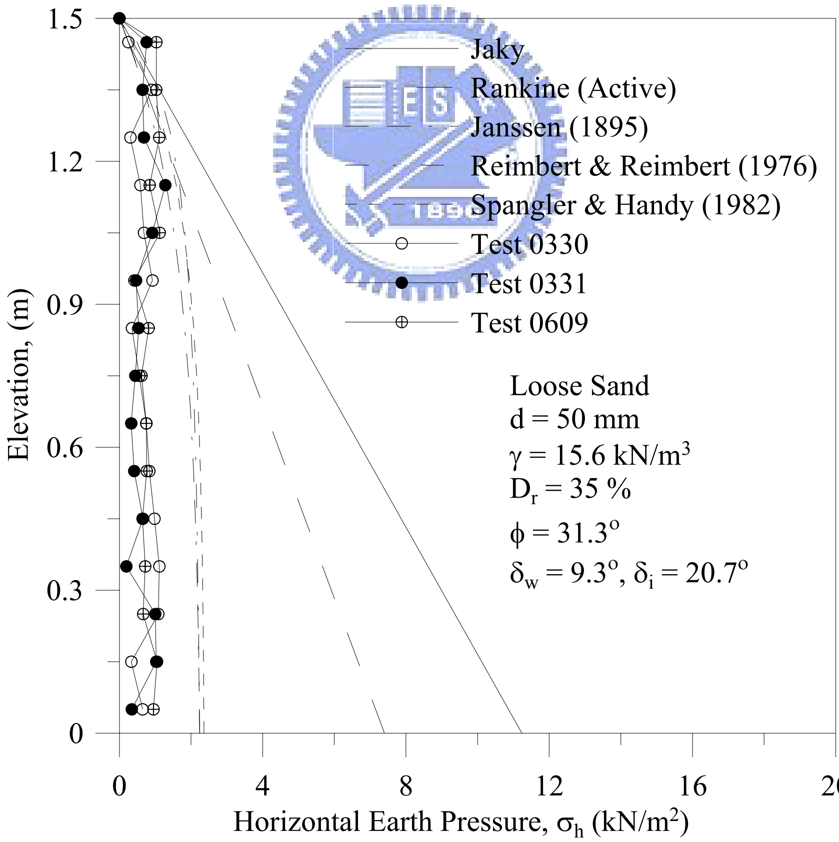

(b)

Fig. 6.10. Distribution of horizontal earth pressure for loose sand with d = 50 mm

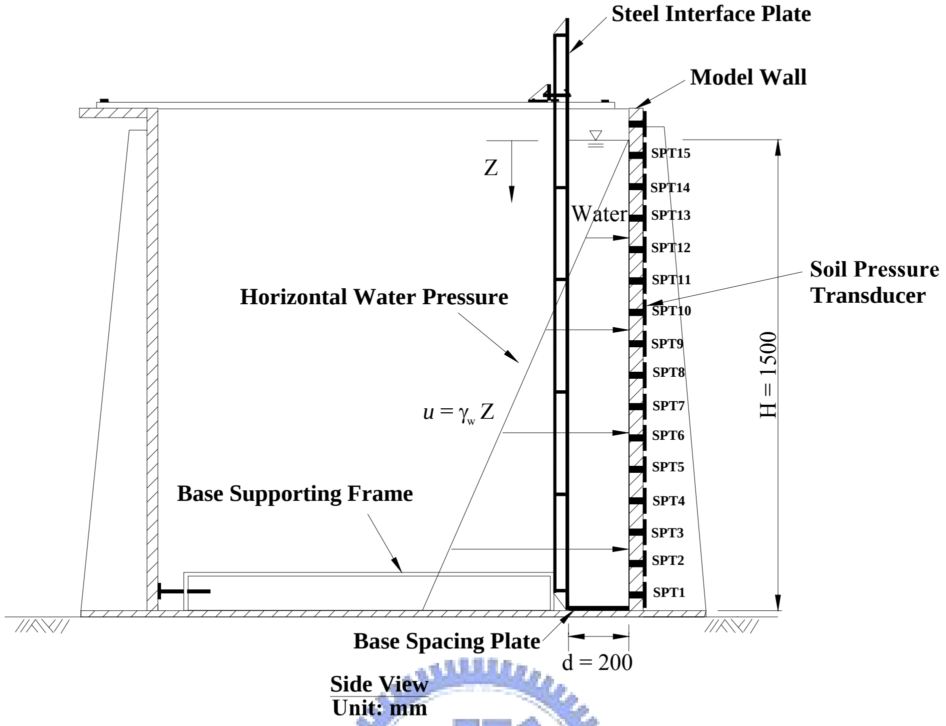

(a) Filled with water

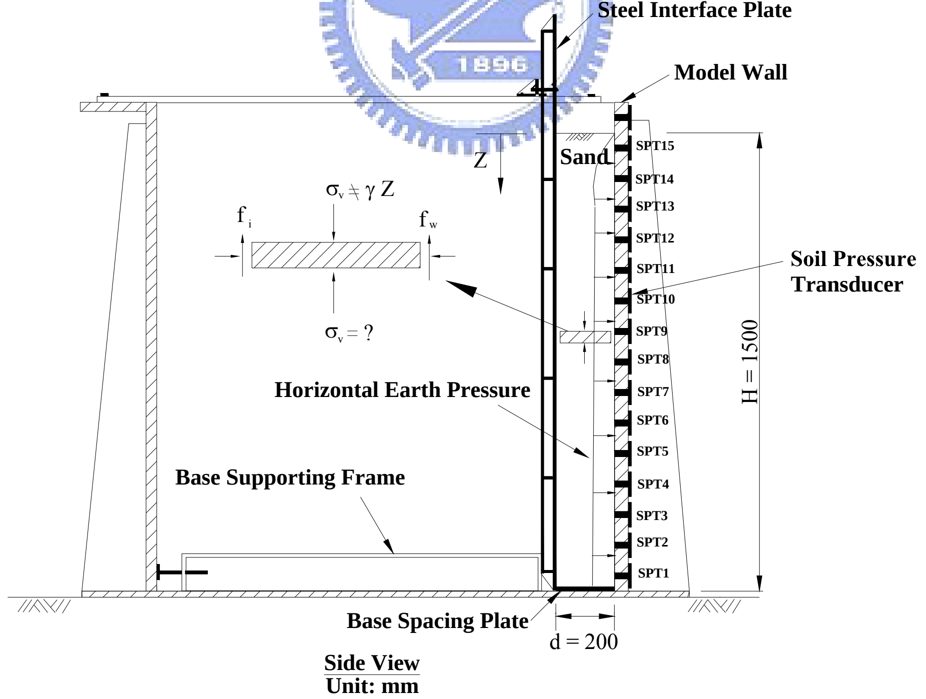

(c) Filled with sand

Fig. 6.11. Distribution of horizontal pressure for water and sand with d = 200 mm

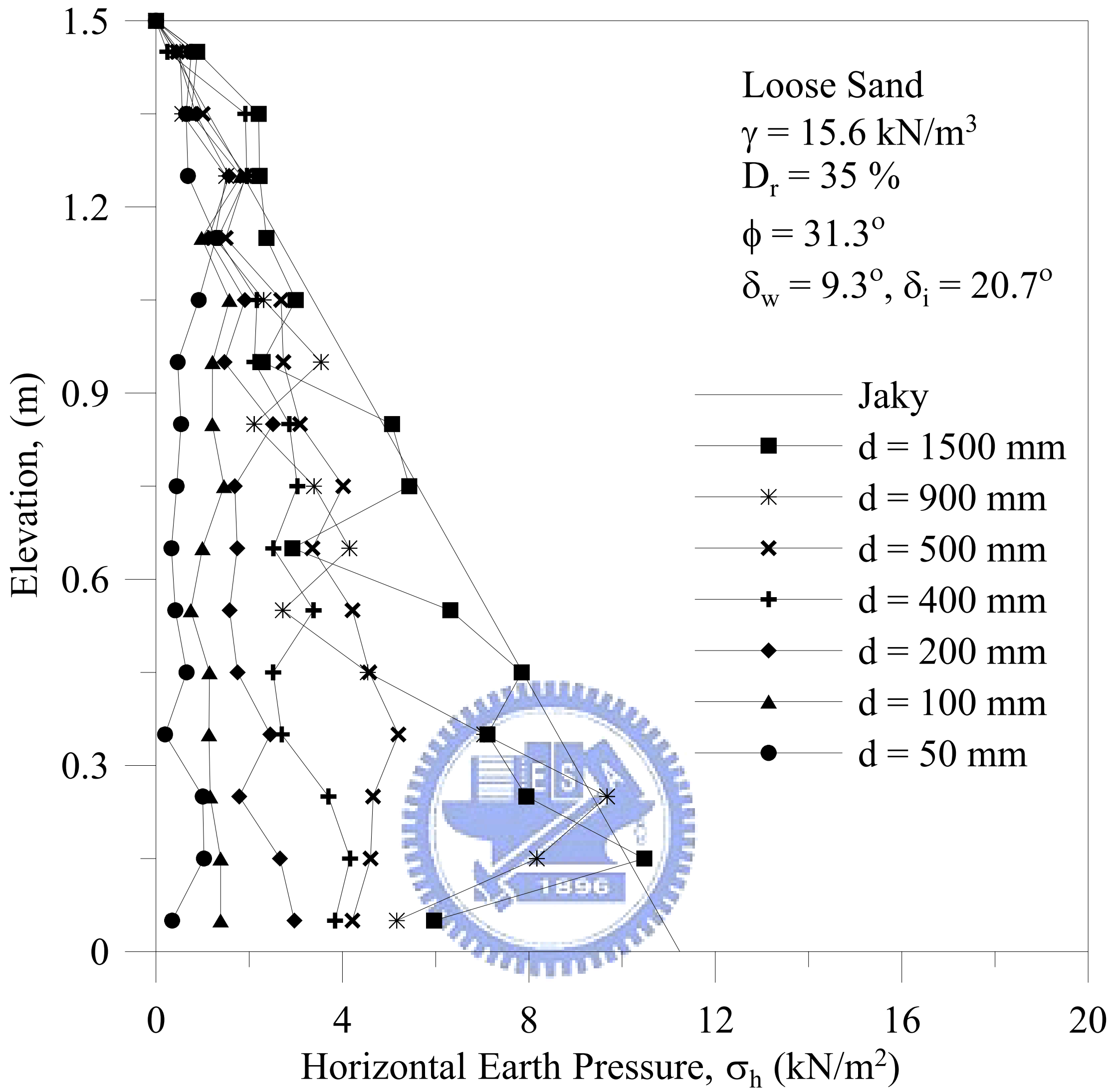

Fig. 6.12. Distribution of horizontal earth pressure for loose sand at different spacing d

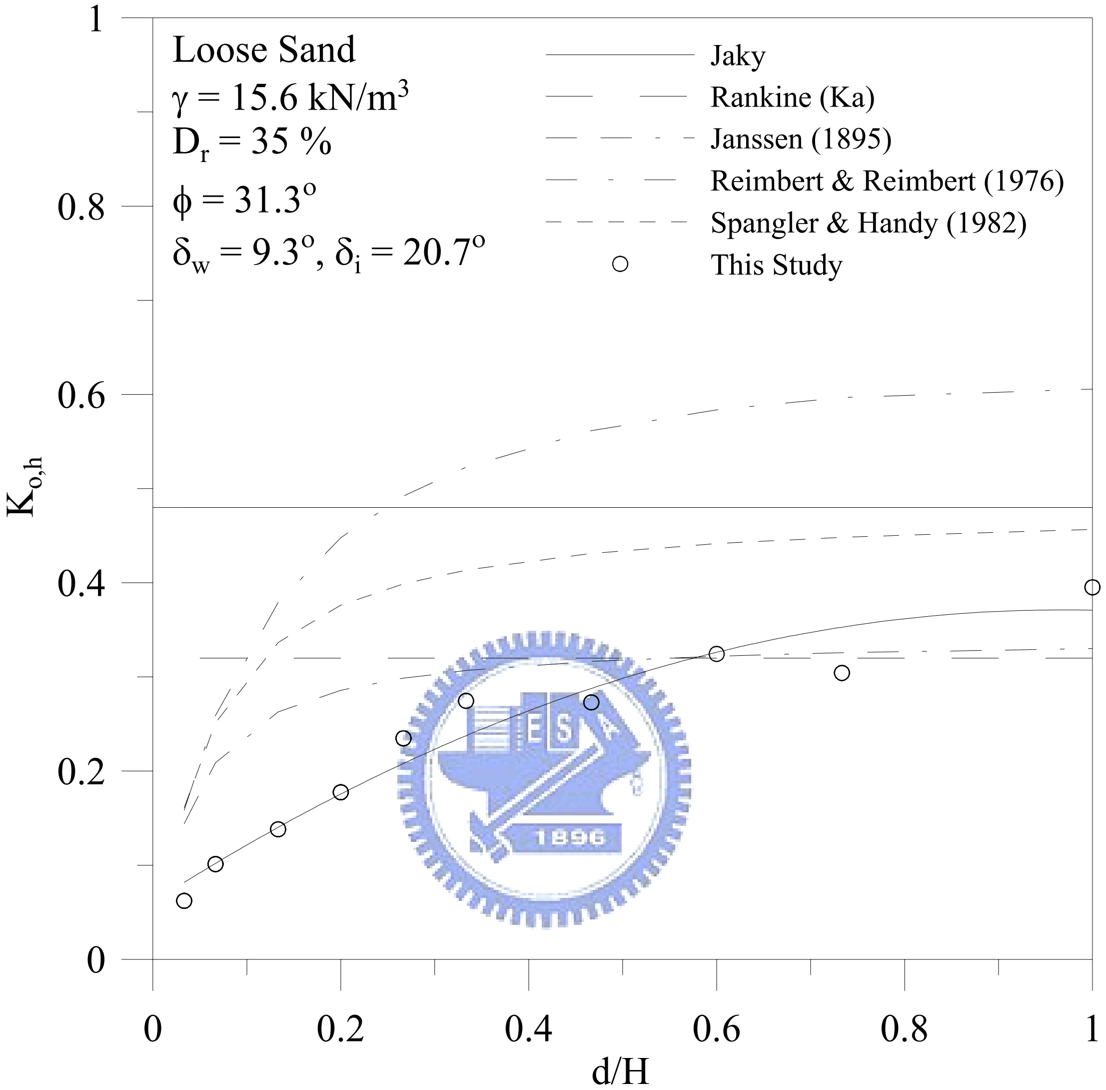

Fig. 6.13. Distribution of $K_{o,h}$ for loose sand at different spacing d

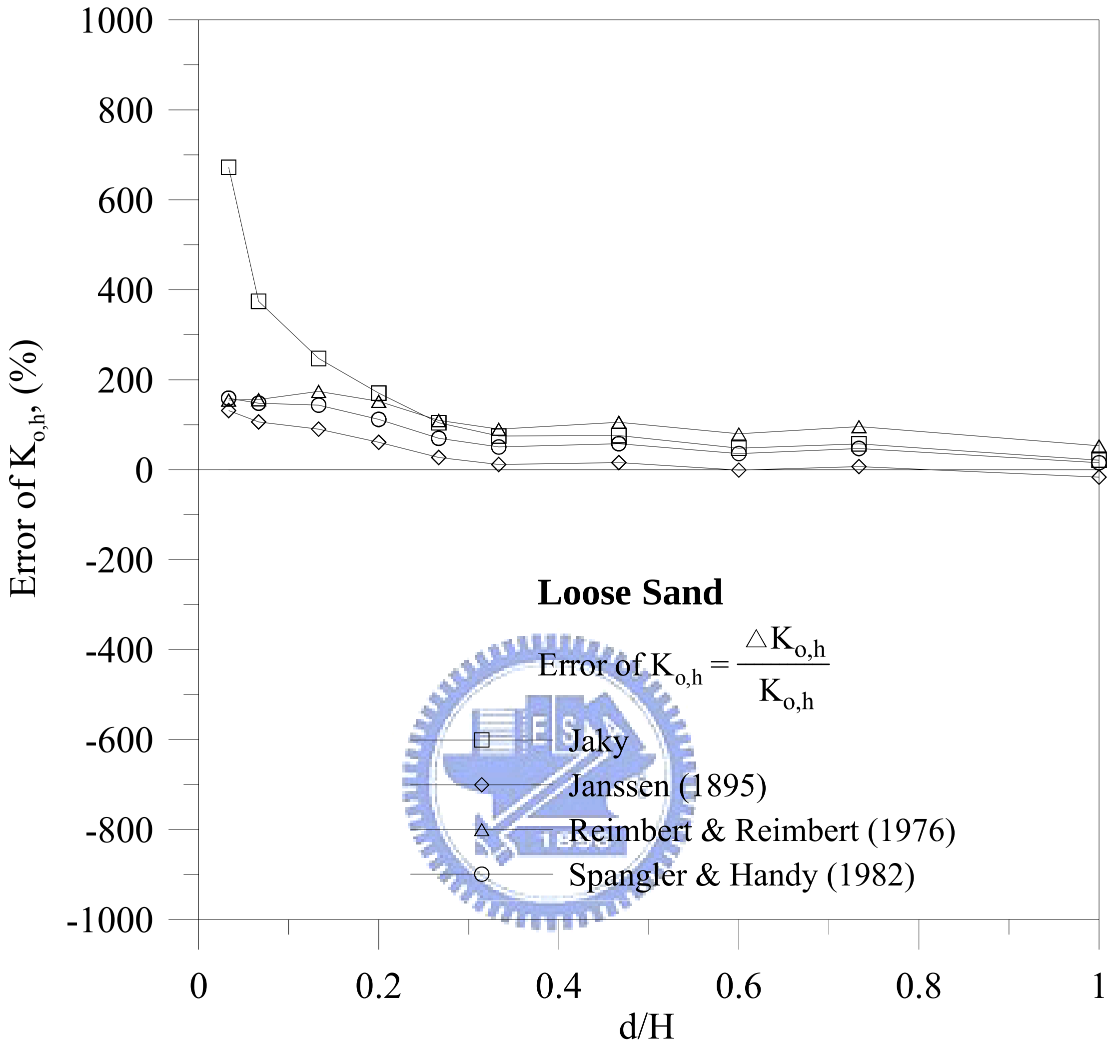

Fig. 6.14. Error of $K_{o,h}$ estimated with different methods

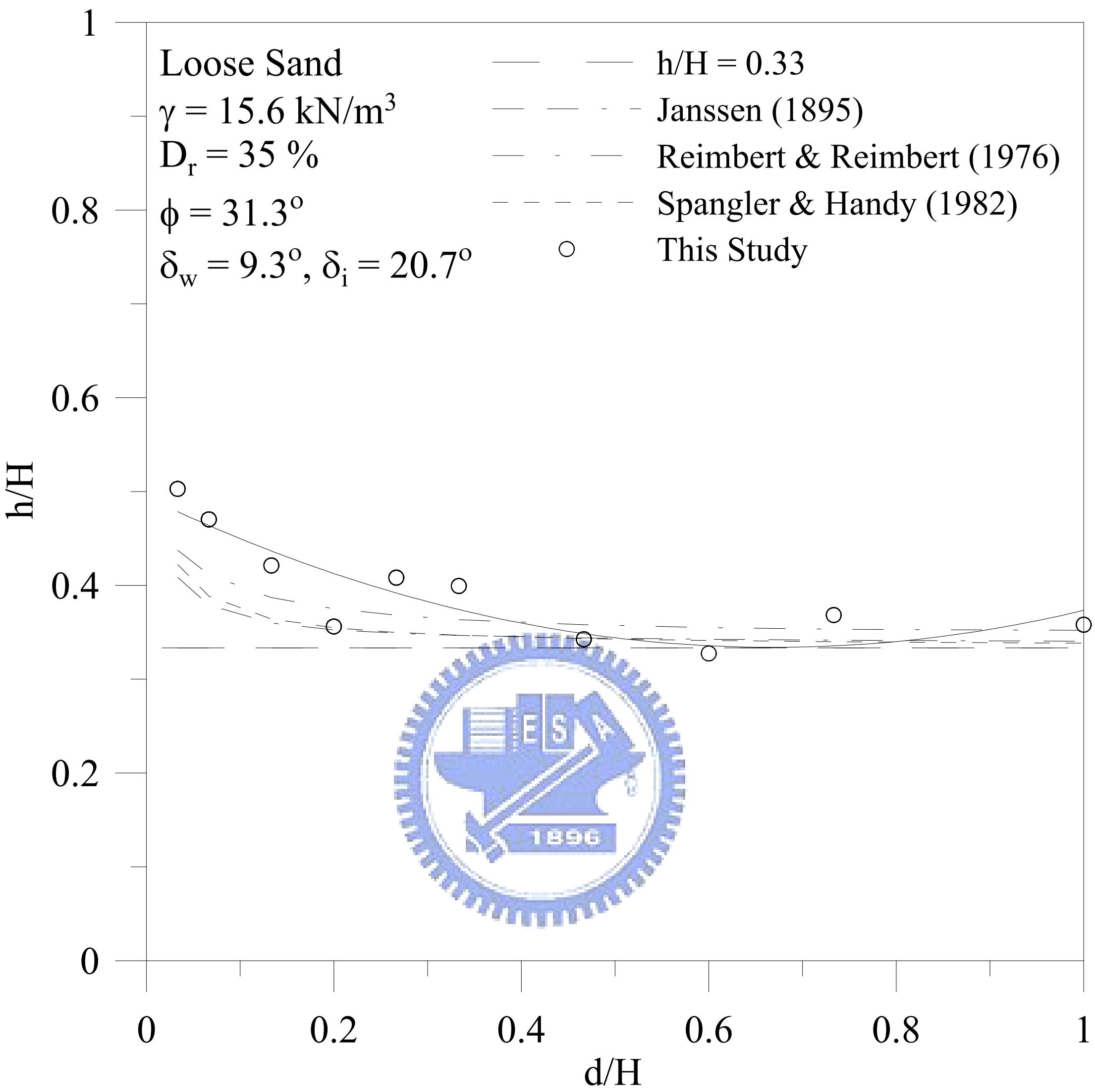

Fig. 6.15. Point of application for loose sand at different spacing d

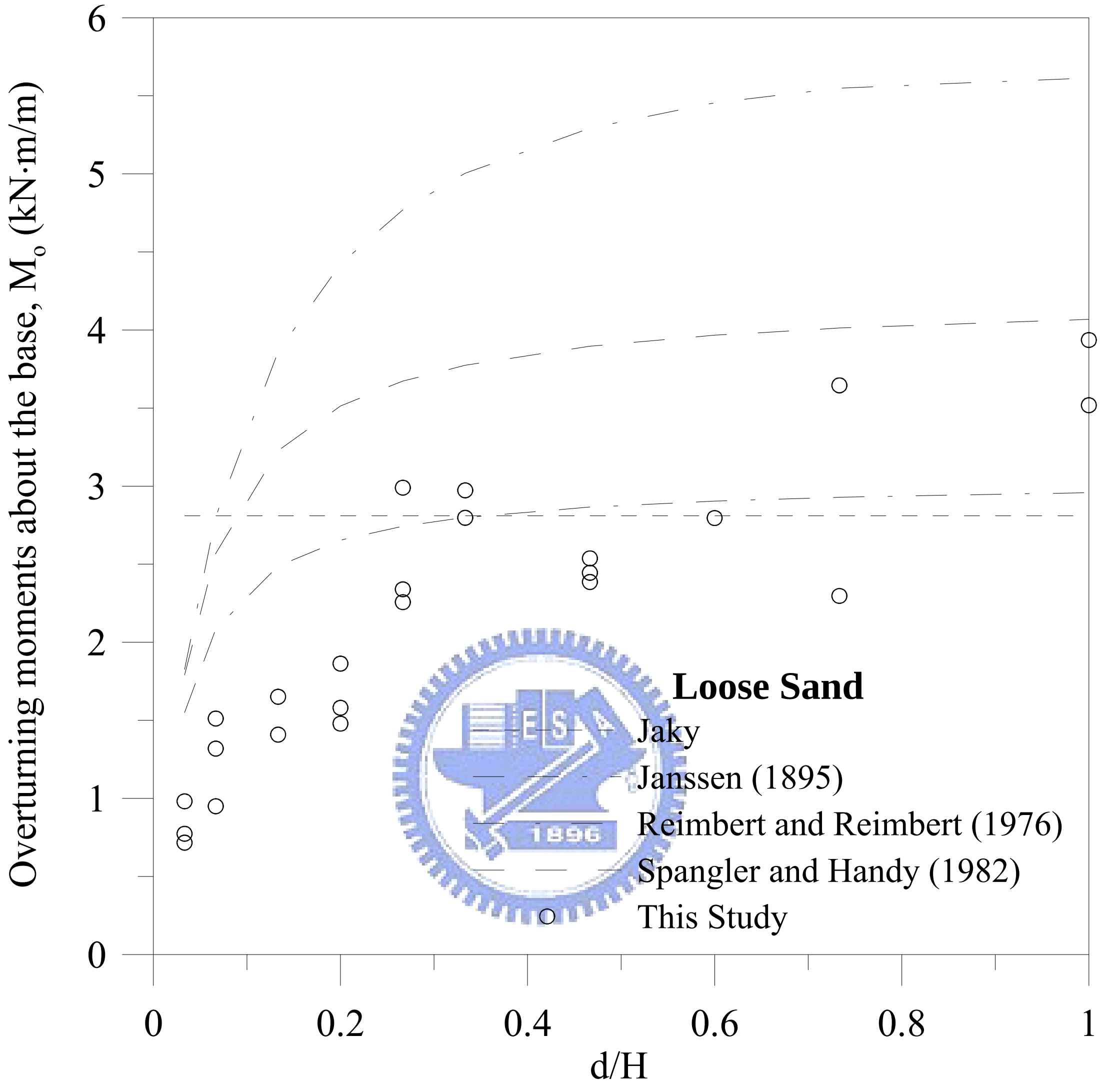

Fig. 6.16. Distribution of overturning moments about the base for loose sand with different spacing d

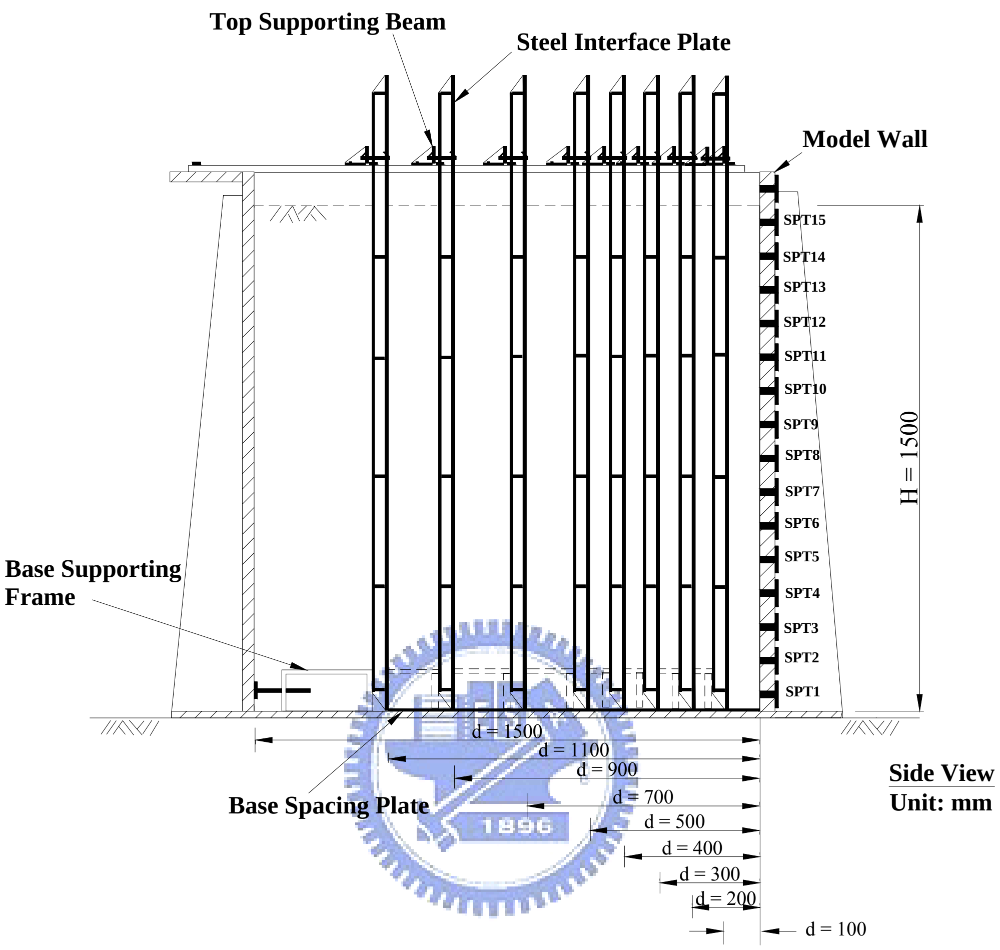

Fig. 7.1. Different spacing d between interface plate and model wall

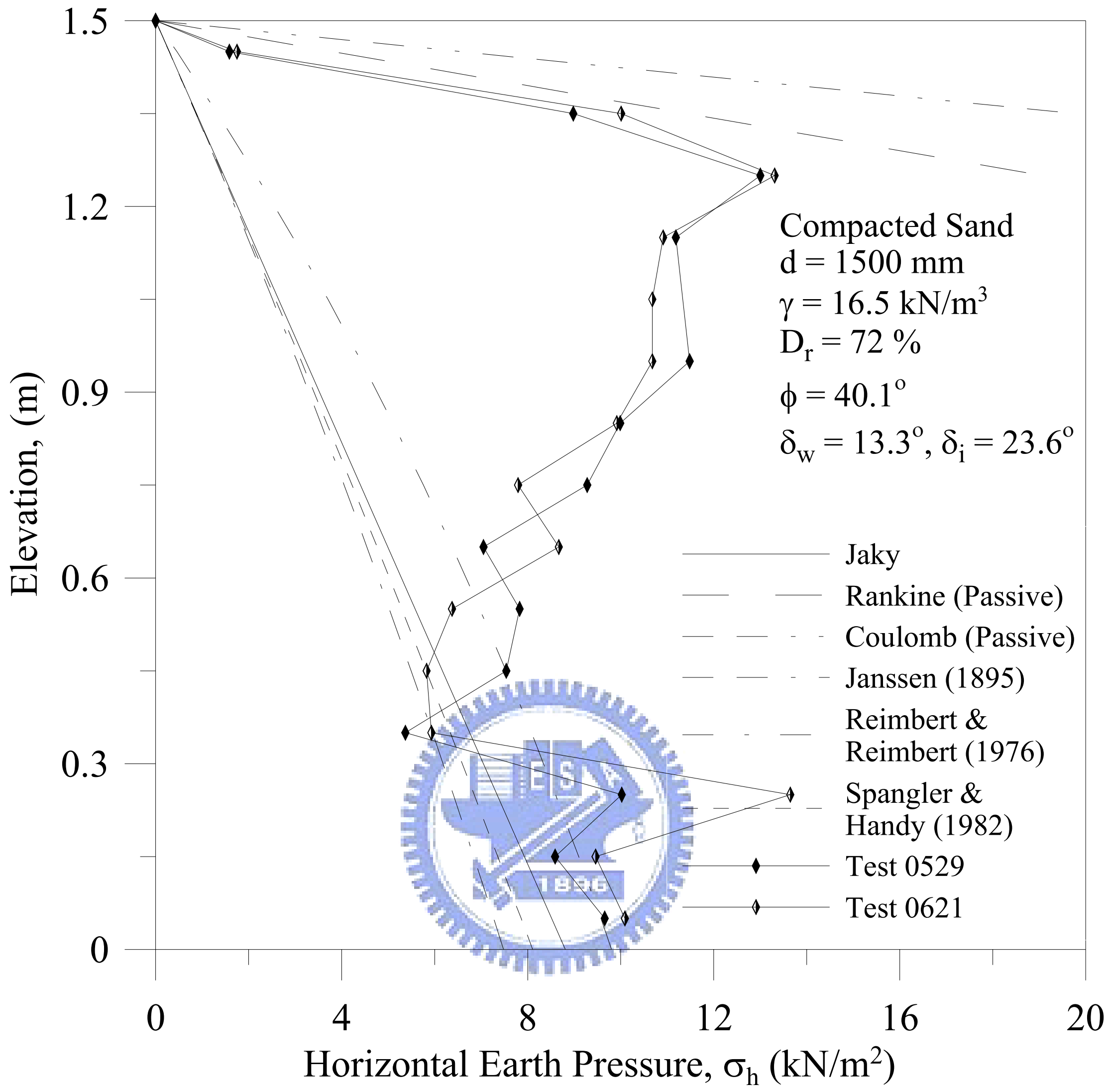

Fig. 7.2. Distribution of horizontal earth pressure for compacted sand with d = 1500 mm

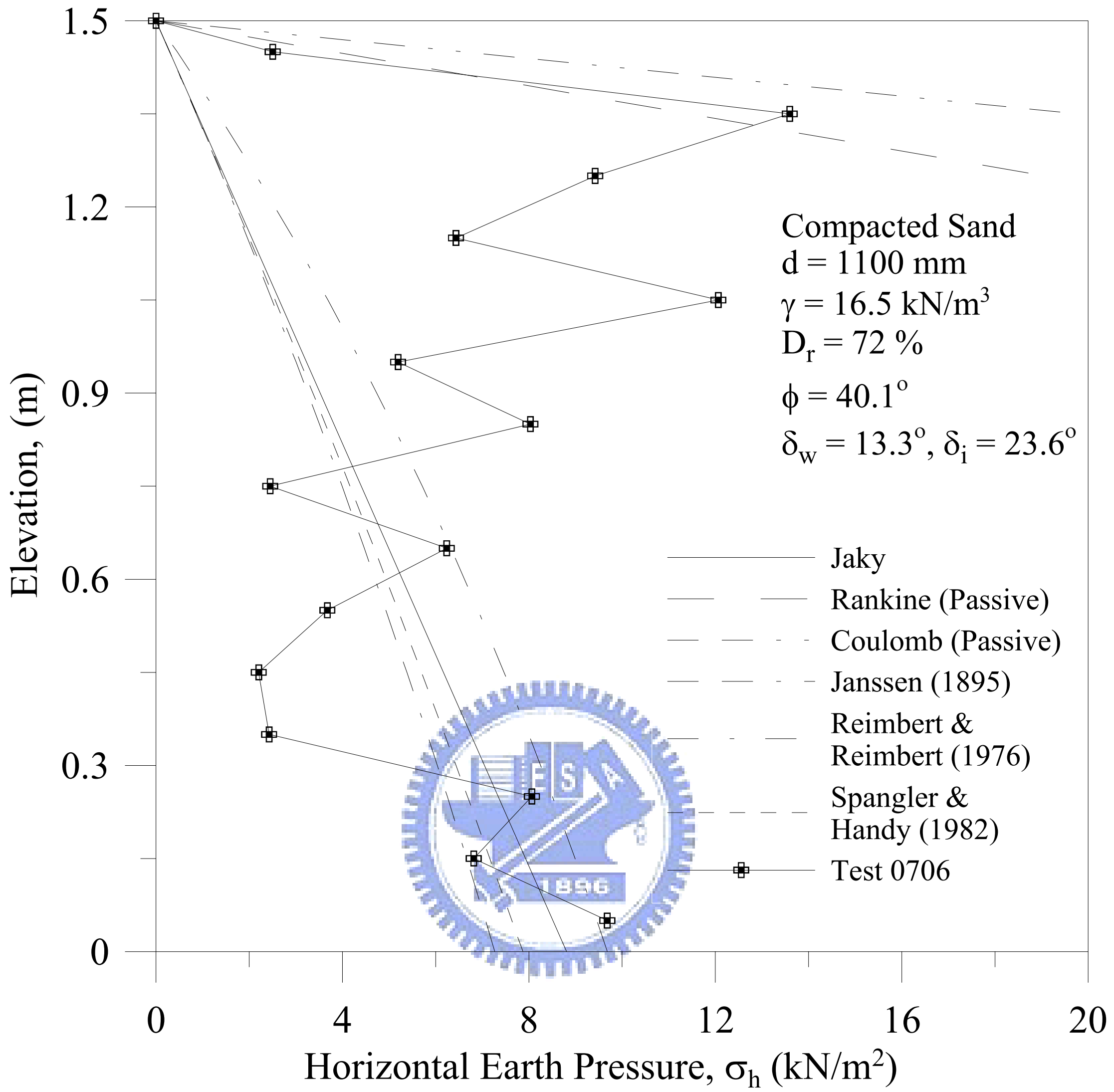

Fig. 7.3. Distribution of horizontal earth pressure for compacted sand with d = 1100 mm

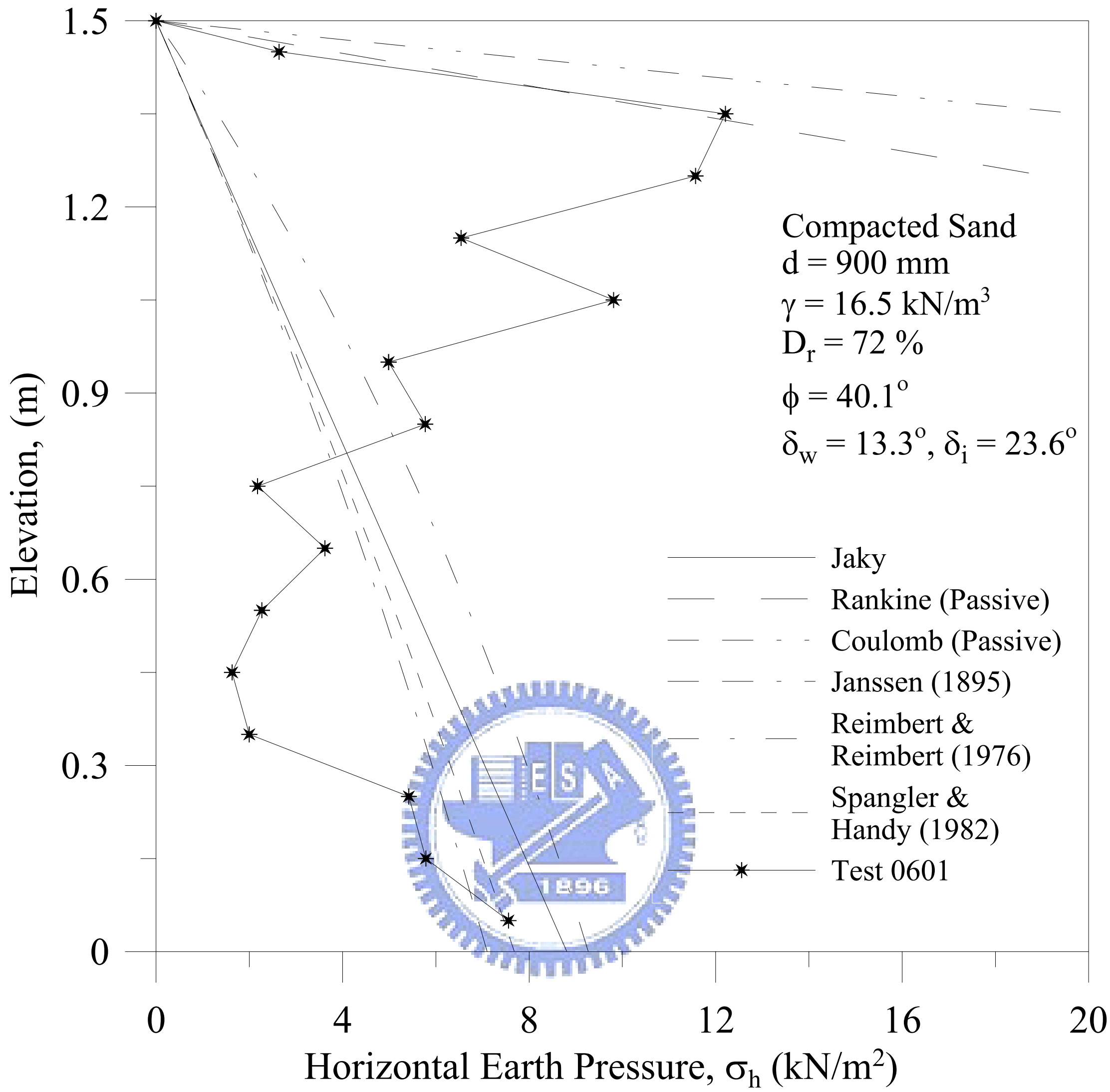

Fig. 7.4. Distribution of horizontal earth pressure for compacted sand with d = 900 mm

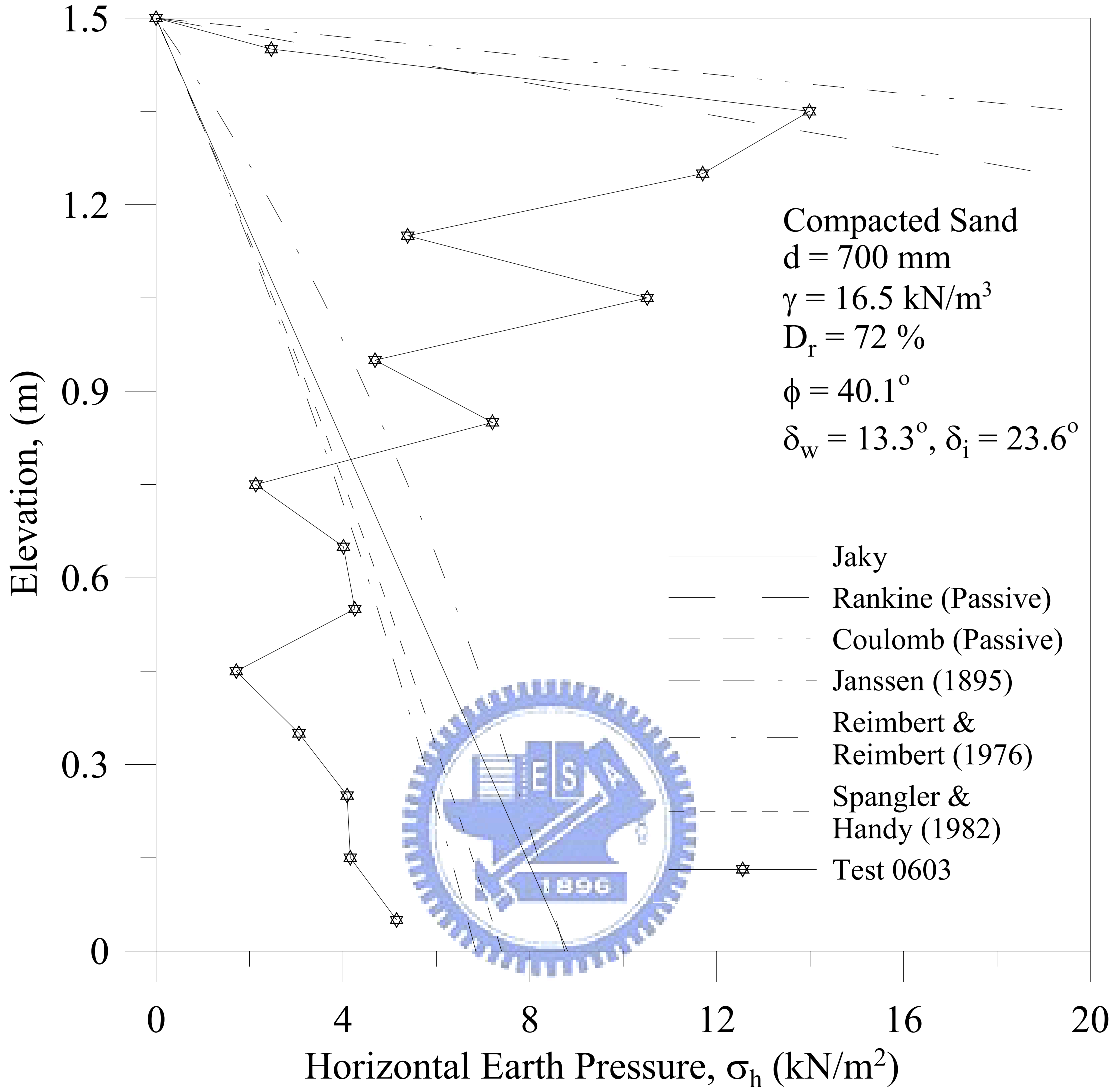

Fig. 7.5. Distribution of horizontal earth pressure for compacted sand with d = 700 mm

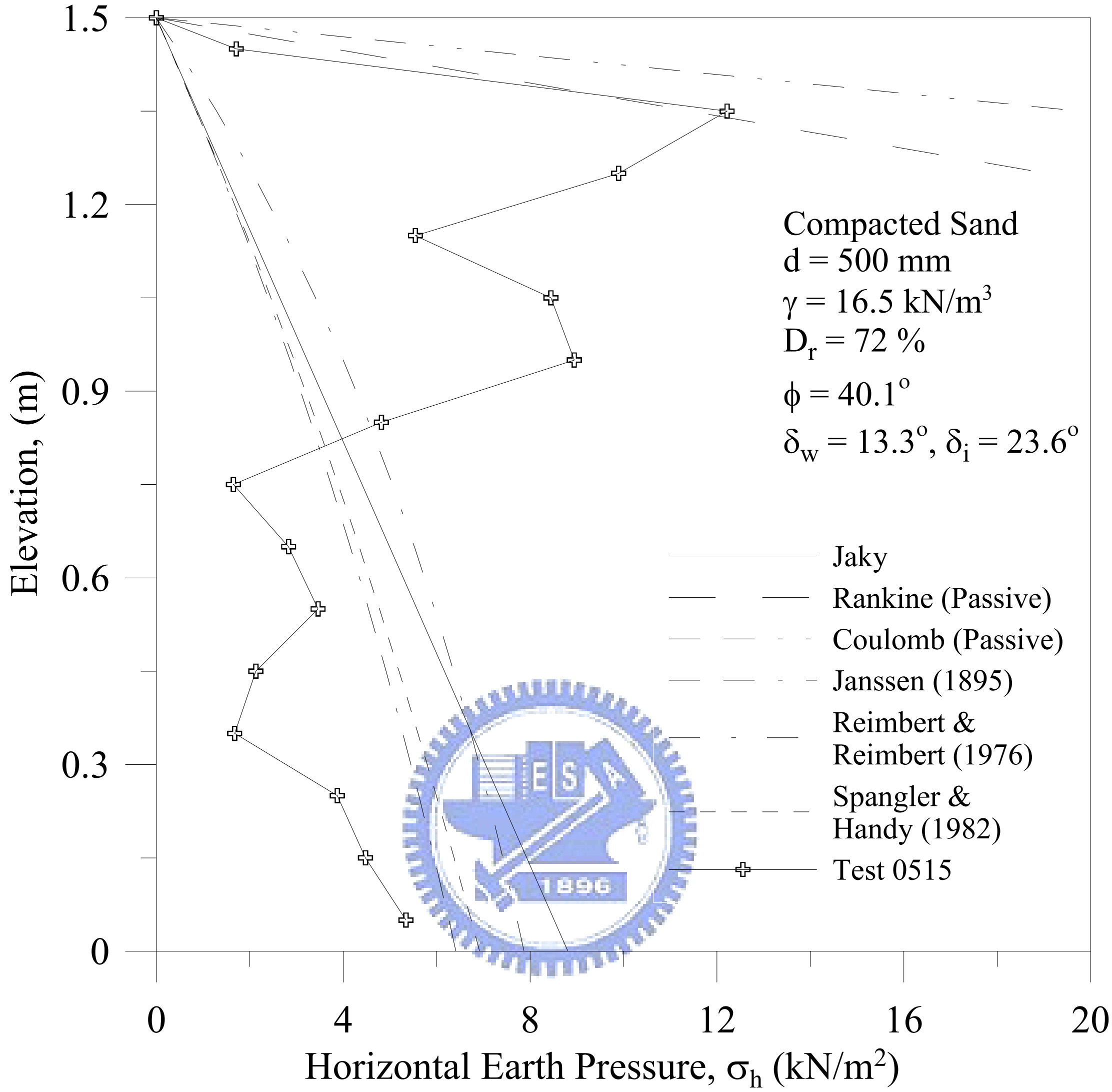

Fig. 7.6. Distribution of horizontal earth pressure for compacted sand with d = 500 mm

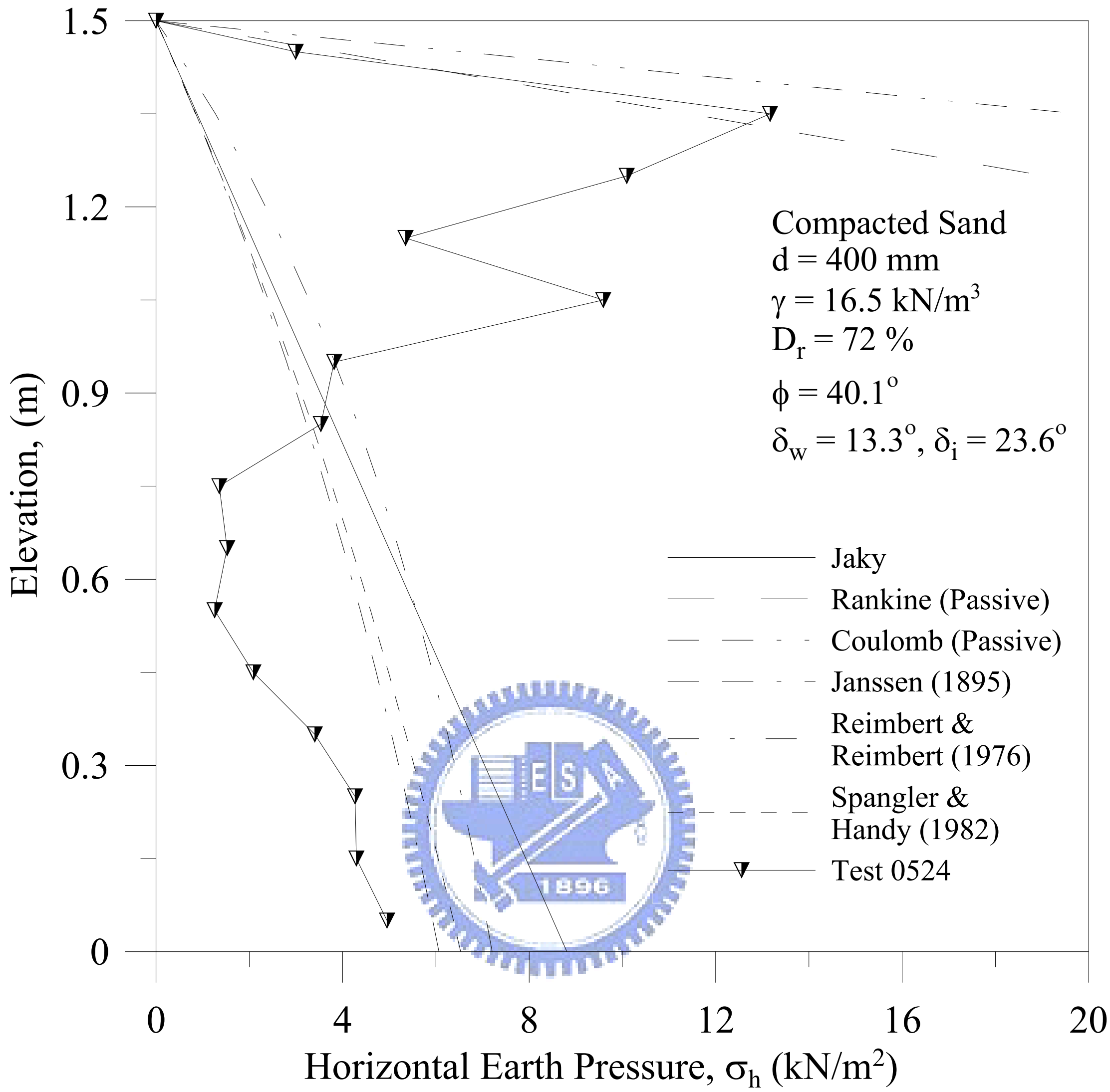

Fig. 7.7. Distribution of horizontal earth pressure for compacted sand with d = 400 mm

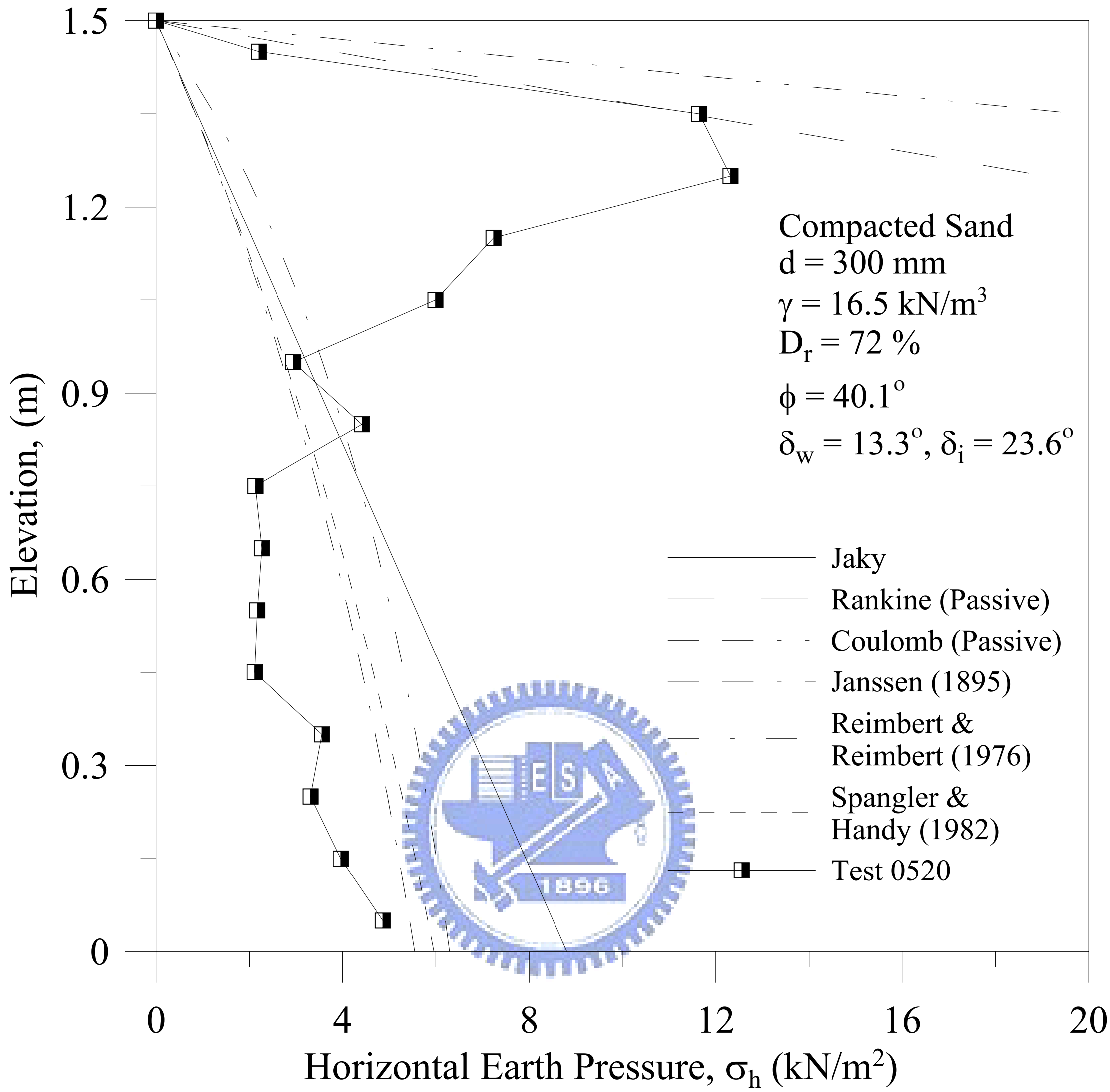

Fig. 7.8. Distribution of horizontal earth pressure for compacted sand with d = 300 mm

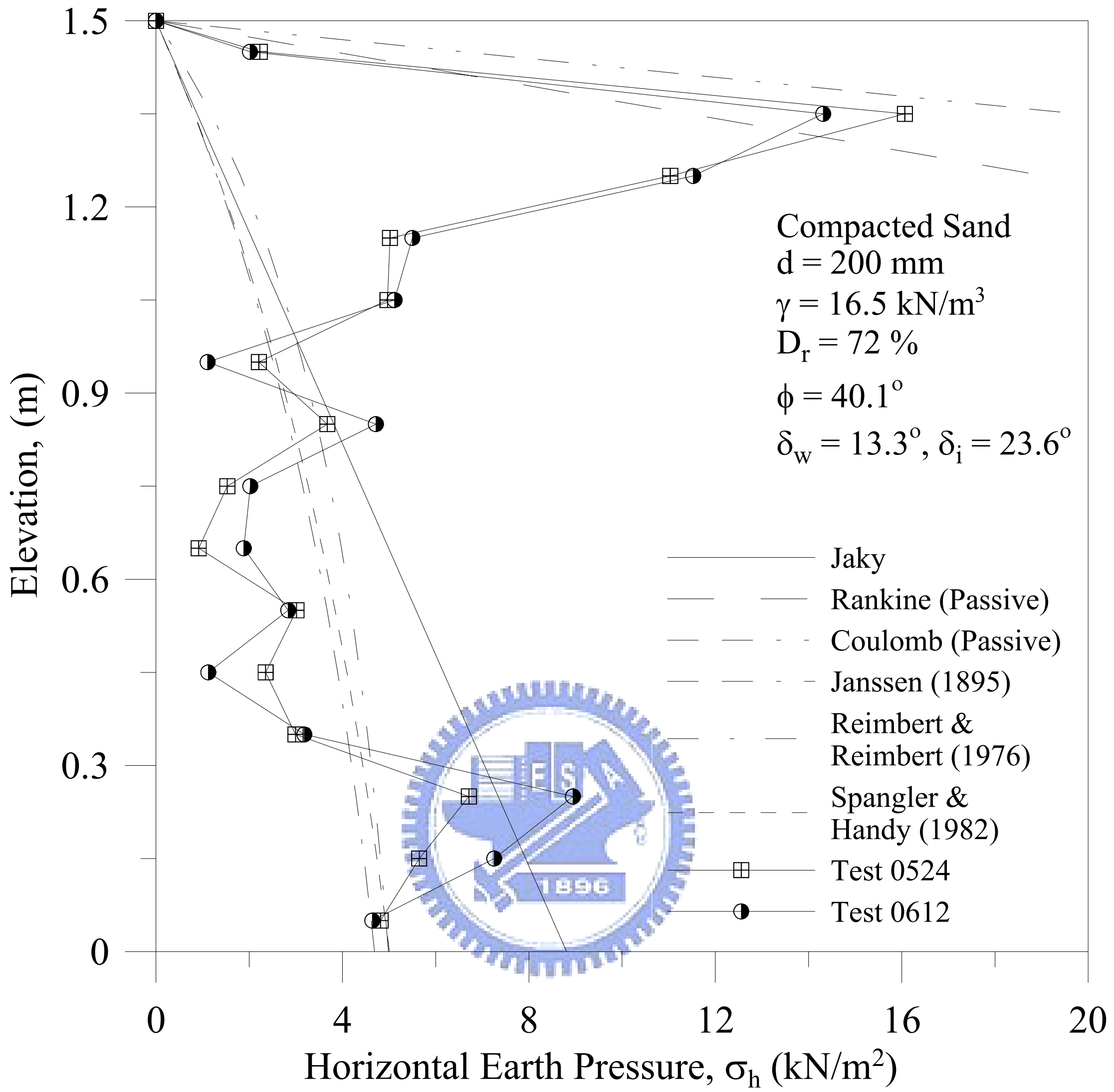

Fig. 7.9. Distribution of horizontal earth pressure for compacted sand with d = 200 mm

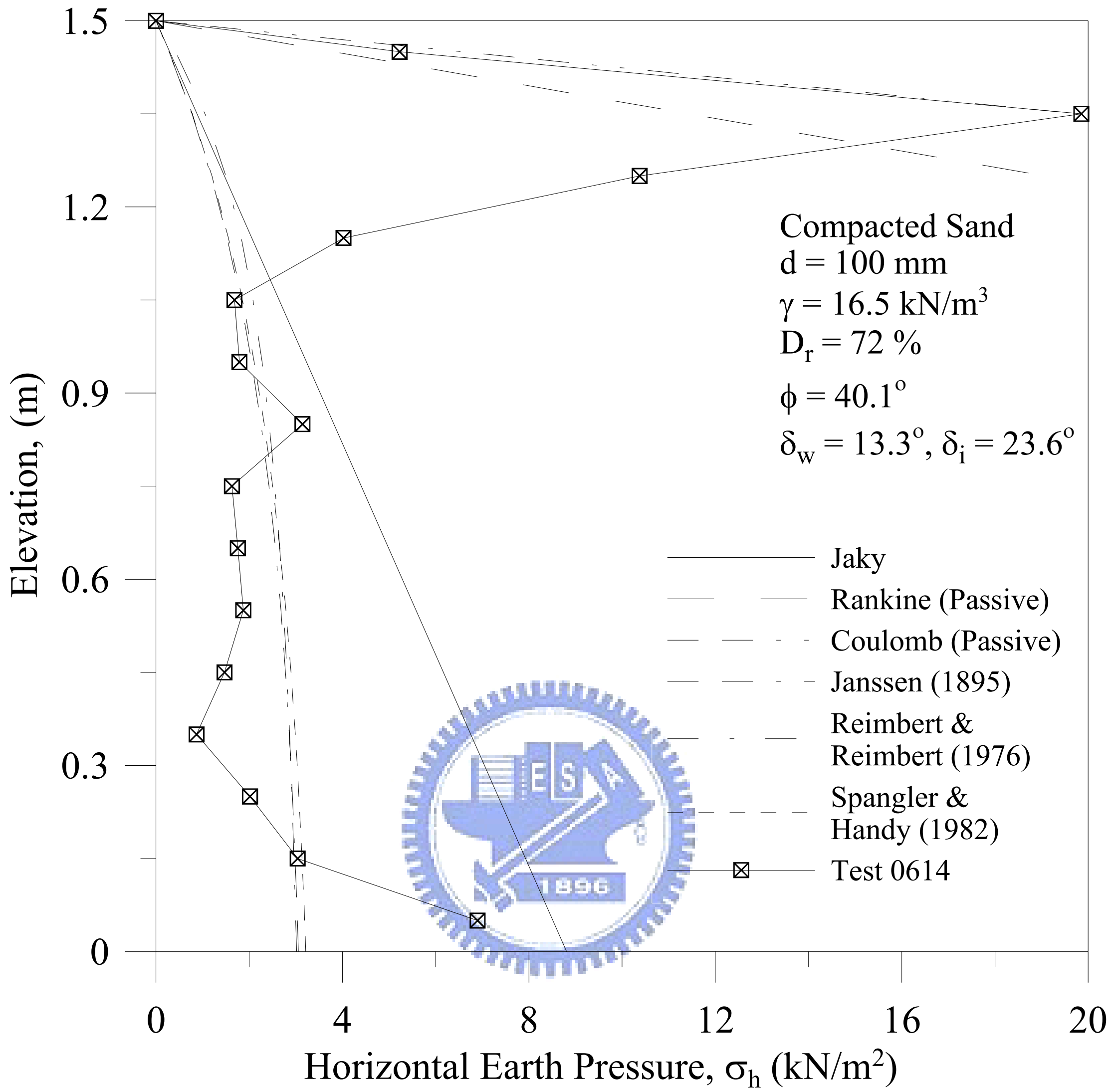

Fig. 7.10. Distribution of horizontal earth pressure for compacted sand with d = 100 mm

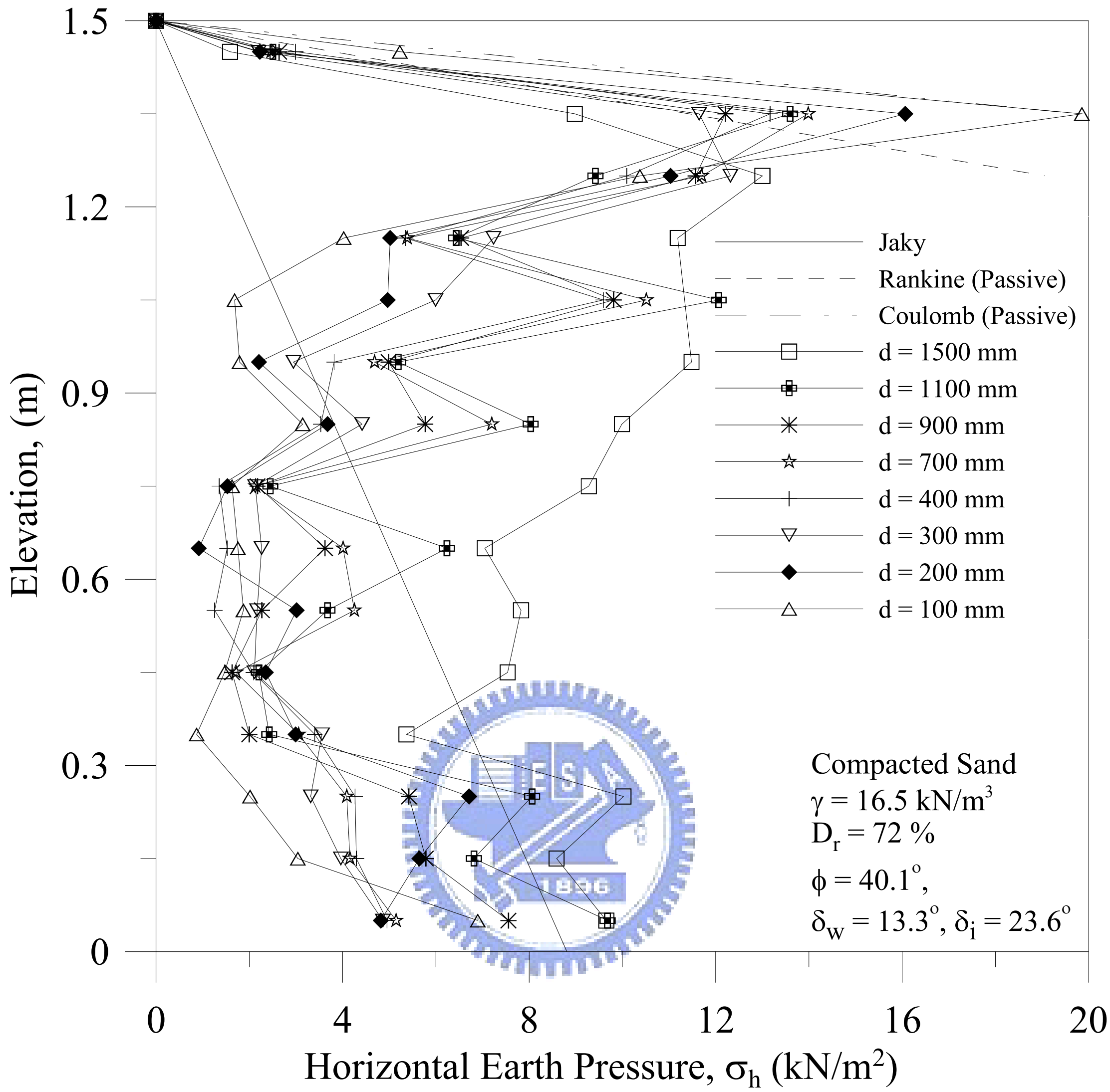

Fig. 7.11. Distribution of horizontal earth pressure for compacted sand at different spacing d

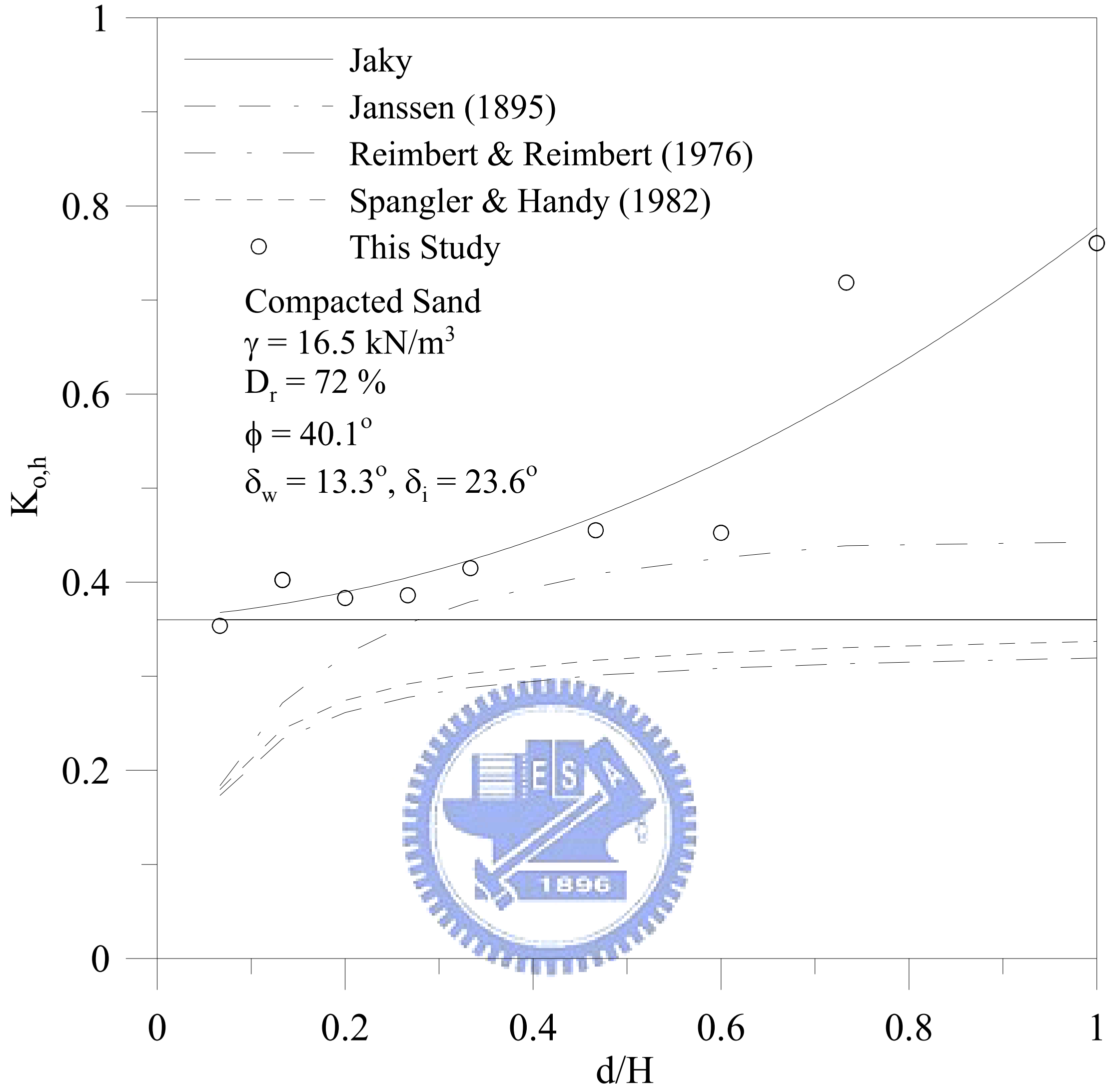

Fig. 7.12. Distribution of $K_{o,h}$ for compacted sand with different spacing d

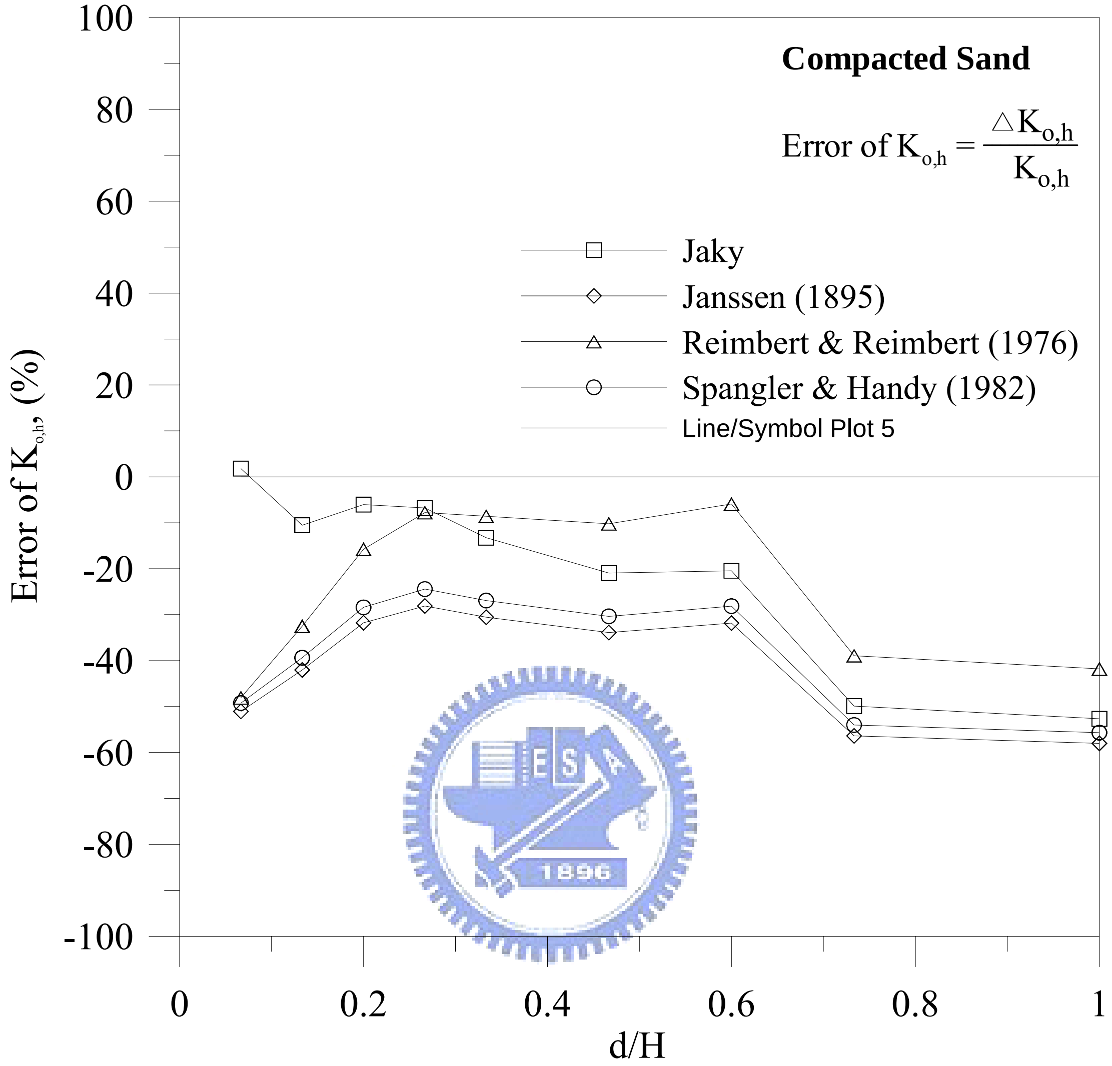

Fig. 7.13. Error of $K_{o,h}$ estimated with different methods

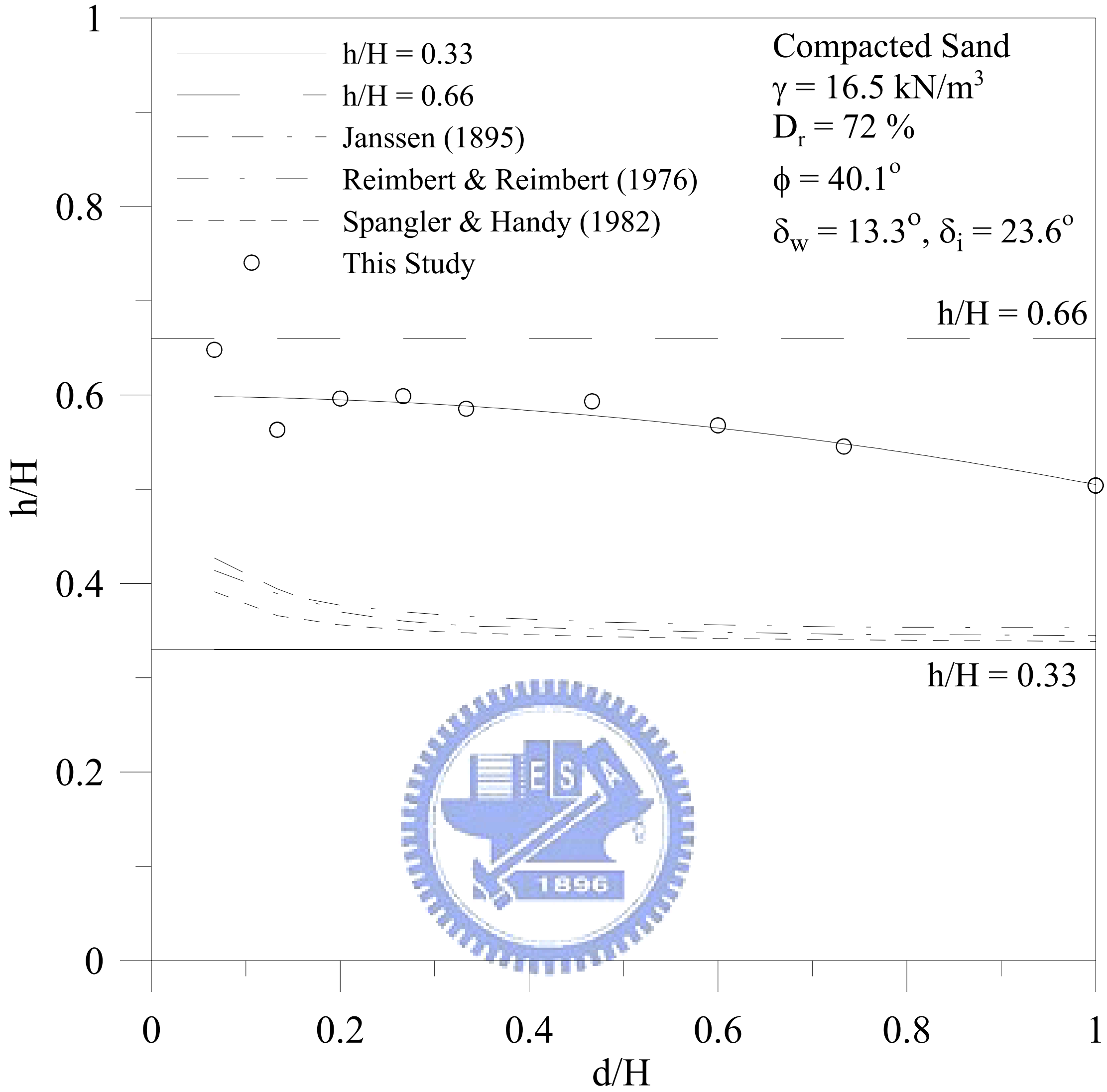

Fig. 7.14. Point of application for compacted sand with different spacing d

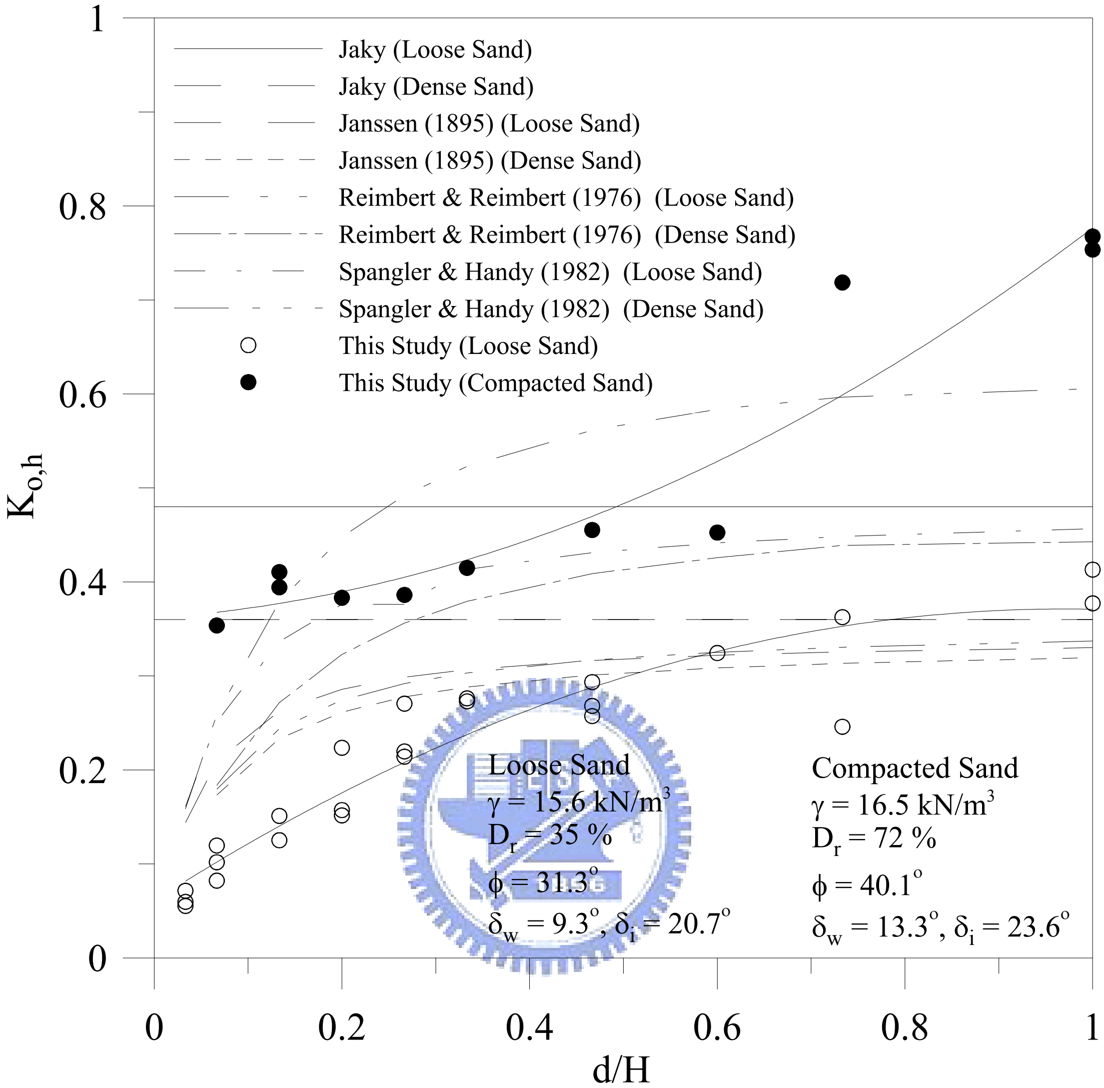

Fig. 7.15. Comparison of $K_{o,h}$ for loose and compacted sand with different spacing d

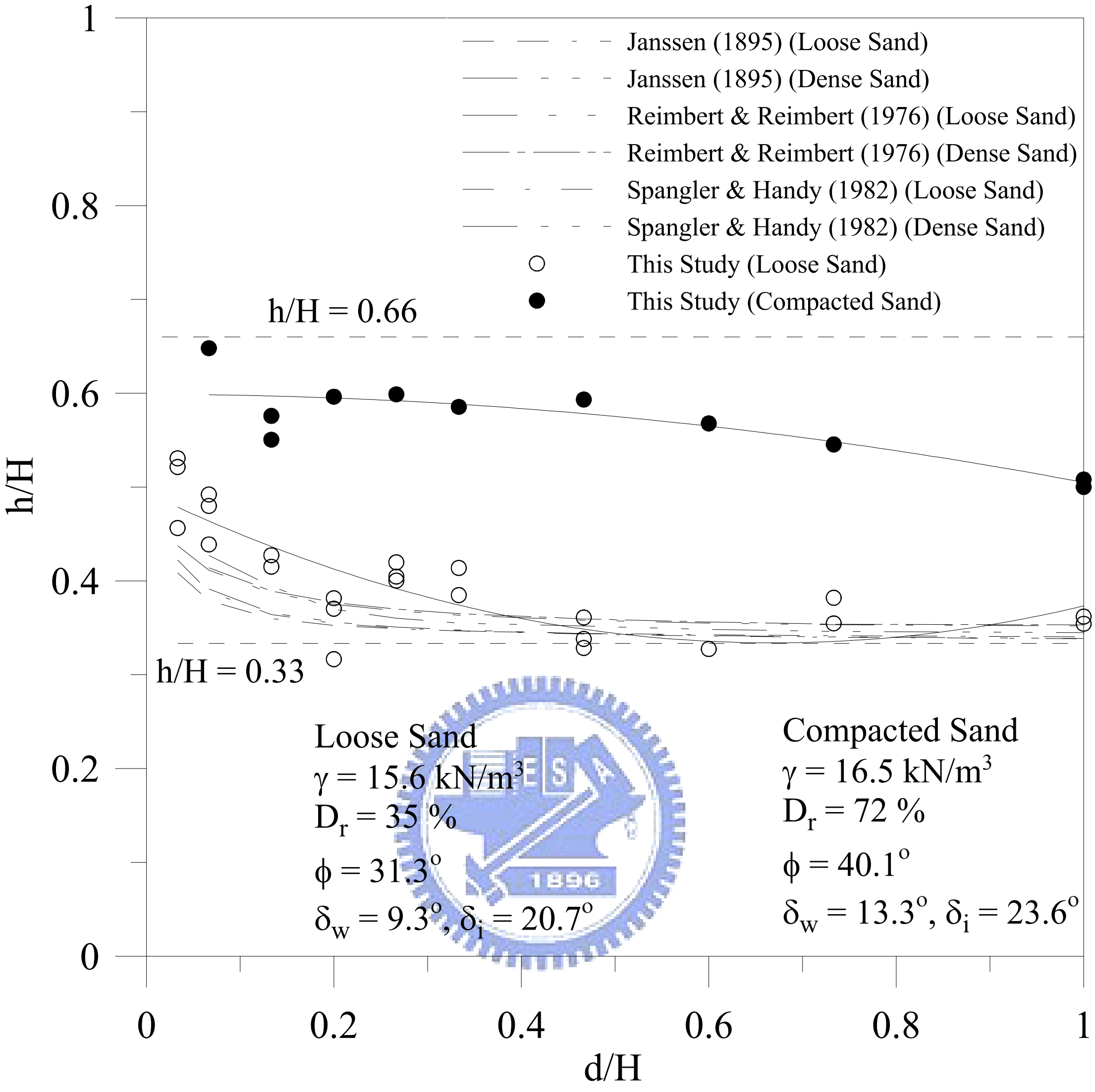

Fig. 7.16. Comparison of h/H for loose and compacted sand with different spacing d